

*Library Circulation*

UNLIMITED

REFERENCE COPY

# Communications Research Centre

## RADAR DETECTABILITY OF LIGHT AIRCRAFT

by

M.V. Patriarche, G.O. Venier and J.R. Lewis

DEPARTMENT OF COMMUNICATIONS  
MINISTÈRE DES COMMUNICATIONS

CRC REPORT NO. 1291

This work was sponsored by the Department of National Defence,  
Research and Development Branch under Project No. 38-03-67.

TK  
5102.5  
C673e  
#1291

IC

CANADA

OTTAWA, APRIL 1976

## TABLE OF CONTENTS

### ABSTRACT

## COMMUNICATIONS RESEARCH CENTRE

### DEPARTMENT OF COMMUNICATIONS

#### CANADA

- 2.1 Radar Target
  - 2.1.1 Time Domain
  - 2.1.2 Frequency Domain
- 2.2 Static Measurement of Light-Aircraft RCS
  - 2.2.1 Low-Wing Cherokee 140
  - 2.2.2 High-Wing Cessna 150
  - 2.2.3 Additional General Conclusions
- 2.3 Dynamic RCS Measurement

### RADAR DETECTABILITY OF LIGHT AIRCRAFT

by

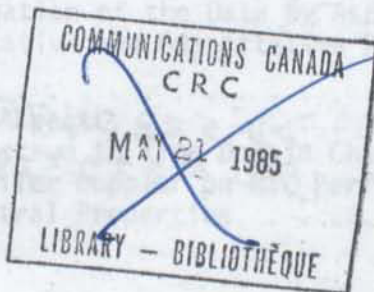
M.V. Patriarche, G.O. Venier and J.R. Lewis

(Radio and Radar Branch)

Industry Canada  
Library - Queen

SEP - 4 2012

Industrie Canada  
Bibliothèque - Queen



CRC REPORT NO. 1291

TELS REPORT NO. 34

Received April 1976

Published April 1976

OTTAWA

This work was sponsored by the Department of National Defence, Research and Development Branch under Project No. 38-03-67.

#### CAUTION

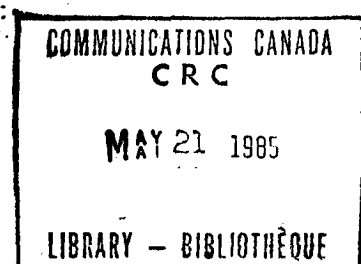
The use of this information is permitted subject to recognition of  
proprietary and patent rights.

TK  
5102.5  
C6730  
#1291  
c.b

DD 5332470  
DL 5332514

## TABLE OF CONTENTS

ABSTRACT. . . . .	1
1. INTRODUCTION. . . . .	2
2. BACKGROUND. . . . .	3
2.1 Radar Target Theory. . . . .	3
2.1.1 Time Domain . . . . .	3
2.1.2 Frequency Domain. . . . .	4
2.2 Static Measurement of Light-Aircraft RCS . . . . .	6
2.2.1 Low-Wing Cherokee 140 . . . . .	6
2.2.2 High-Wing Cessna 150. . . . .	11
2.2.3 Additional General Conclusions. . . . .	11
2.3 Dynamic RCS Measurement. . . . .	16
3. CRC RADAR DATA ACQUISITION SYSTEM . . . . .	18
3.1 Coherent Laboratory Radar. . . . .	18
3.2 Radar-Computer Interface . . . . .	20
3.3 Data Acquisition Software. . . . .	21
3.3.1 Calibration Module. . . . .	21
3.3.2 Recording Module. . . . .	21
4. LIGHT AIRCRAFT COHERENT RADAR DATA. . . . .	23
4.1 Time Domain RCS Fluctuation. . . . .	24
4.1.1 Short-Term Mean RCS . . . . .	24
4.1.2 Dynamic RCS Probability Density Estimates . . . . .	27
4.1.2.1 Segregation of the Data by Aspect. . . . .	27
4.1.2.2 Qualitative and Quantitative Results . . . . .	28
4.2 Aircraft RCS Spectrum. . . . .	31
4.2.1 Variation with Aspect . . . . .	36
4.2.2 Relation to Spectrum to Time Domain Characteristics . . . . .	38
4.2.3 Effect of Propeller Doppler on MTI Performance. . . . .	39
4.2.4 Summary of Spectral Properties. . . . .	41



## 1. INTRODUCTION

At the request of the Directorate of Electronics Engineering and Maintenance, Department of National Defence, the Communications Research Centre (CRC) undertook a study of the radar echoing characteristics of some common types of light aircraft. The information to be obtained included the mean value of the radar cross-section (RCS), the doppler spectrum of the return, and the incidence of "tangential fading" in MTI radars. The Ministry of Transport expressed interest in the project, and accepted an invitation to participate.

The concern expressed by both military and civil authorities arises from the hazard presented to airline and military traffic by light aircraft operating in the vicinity of an airport. Light aircraft are not usually equipped with transponders, and experience shows that they are not detected reliably by primary radar; in addition, they are frequently operated by inexperienced pilots. The possibility of mid-air collisions evidently exists, and several such events have occurred in recent years. The MOT Aircraft Accident Report included as Appendix A describes a collision between an Air Canada Viscount and a private Ercoupe at Vancouver. The report concludes: "The Ercoupe, because of its size, provides an unreliable radar return. This partially negated the value of the air traffic control radar." The conclusion that the poor detectability of light aircraft is due to their small size is widely accepted, usually without any examination of the fundamental capabilities of radar detection.

Concurrently with the planning of the work reported here, the US Federal Aviation Administration (FAA) carried out an extensive program of measurements of static RCS for three common types of light aircraft.<sup>6</sup> Static RCS is measured with the aircraft motionless on the ground and the engine off; the aircraft is mounted on a structure that enables the viewing angle (aspect) presented to the radar to be varied. For each aircraft type, the RCS was measured for a wide range of aspects, radar frequencies, and polarizations. The program was carried out at the Radar Target Scatter Division (RAT SCAT), Holloman Air Force Base, New Mexico. These results complement the dynamic (in-flight) results obtained in the present investigation, and extensive use is made of them in this report. Dynamic measurements are preferable to static measurements in several respects: the aircraft is in its normal environment; there are no spurious reflections from the ground or from the supporting structure; and the effects of propeller rotation, small aircraft motions due to control action or atmospheric turbulence, and structural deflections due to inertial and aerodynamic loading, are properly represented. The principal advantage of static measurements is the precise control of aspect that this method permits.

This report summarizes the results of the FAA program, and describes two series of experiments carried out to determine the characteristics of the radar echoes from three types of light aircraft in flight. In one series, a calibrated coherent radar was used to measure the RCS, its amplitude probability-density function, and the spectrum of the echo, as functions of aspect angle for each aircraft type. In the second series, the ability of an operational ASR-5 airport surveillance radar to detect light aircraft was assessed; this series included investigations of tangential fading (the attenuation of the output that occurs in MTI radars with targets of low radial

velocity), for both linear and circular polarizations of the radar pulse. The final section of the report summarizes the results obtained in this and previously published work, and some implications of these results are presented in the form of recommendations concerning the design, siting, and operation of future radar systems. If implemented, these recommendations would provide, at some future date, a partial solution to the problem of light aircraft detectability. The principal recommendation in this section is based on an alternative (and preferred) approach, which offers a virtually complete solution to the problem, and could be implemented immediately.

## 2. BACKGROUND

The purpose of this section is to review aspects of basic radar target theory in a form that will be needed in later sections, and to summarize literature of particular relevance to this report.

### 2.1 RADAR TARGET THEORY

#### 2.1.1 Time Domain

The radar equation gives the peak target power received by a radar as<sup>2</sup>:

$$P_r = \frac{P_t G^2 \lambda^2 F^2}{(4\pi)^3 R^4} \sigma, \quad (1)$$

where  $P_t$  is the peak transmitted power in watts,  $G$  is the antenna power gain,  $\lambda$  is the wavelength in metres,  $F$  is the propagation factor (describing lobing and beam shape effects),  $R$  is the range to the target in metres and  $\sigma$  is the target radar cross section (RCS) in square metres. Antenna gain and propagation factors are assumed to be equal for reception and transmission. The least well-defined term in the radar equation is usually the target RCS, which is a random variable. For a target having many individual scatterers, none of which is dominant, it can be shown that the amplitude of the received signal has the Rayleigh distribution; and, correspondingly, the power of this signal has the exponential distribution. It follows that the probability distribution of the RCS of such a target is exponential. This density function may be written as:

$$p(\sigma) = \frac{1}{\bar{\sigma}} e^{-\frac{\sigma}{\bar{\sigma}}}, \quad \sigma \geq 0, \quad (2)$$

where  $\bar{\sigma}$  is the mean cross section. When the correlation properties of the radar cross section are such that RCS is essentially constant from pulse-to-pulse, but varies from scan-to-scan, the target is said to follow Swerling's Case 1, probably the most commonly-assumed distribution for ATC radar system calculations.

Edrington<sup>3</sup> has measured amplitude data for two piston and two jet engined aircraft as they approached a radar, nose-on, at low altitude. The specific aircraft types were not identified. Briefly, Edrington concluded that "with good consistency, the aircraft echo power was exponentially distributed up to levels as high as 6 to 80".

An aircraft echo can be modelled mathematically using the amplitude and phase of the reflections from its principal scattering centres. Clearly, when considered as a set of fixed scatterers irradiated at a particular aspect angle, the aircraft has an RCS which is entirely deterministic. The *statistical* problem of computing radar probability of detection can then be stated in two ways, namely:

- (a) what is the probability of detecting one of a number of identical aircraft, each with mean cross section  $\bar{\sigma}$ , at some point in a manoeuvre; or
- (b) what is the probability of detecting an aircraft of mean cross-section  $\bar{\sigma}$ , on each scan of a number of scans, as the aircraft flies through a particular manoeuvre.

Averaging as in (a) and (b) above is analogous to the ensemble and time averaging of random-process theory; where, as is the case here, the two are not equivalent except under certain restrictive conditions. In the measurements described later in this report, the second approach to probability of detection estimation was generally adopted, since it is appropriate to the operation of "controlling" aircraft, and leads to relatively straightforward experiments.

### 2.1.2 Frequency Domain

The doppler frequency of a moving target is given by:

$$f_d = \frac{2v_r}{\lambda}, \quad (3)$$

where  $v_r$  is the radial velocity and  $\lambda$  is the wavelength in consistent units. The spectrum of a light aircraft radar return will consist of a fuselage line and sidebands, the latter deriving largely from reflections off the moving propeller itself, and the chopping of the fuselage return by the propeller. Aspect will determine which effect dominates. Gardner<sup>4</sup>, in an excellent paper devoted to spectra of aircraft targets, concluded that:

- (a) "Rotating propeller blades produce doppler-shifted echoes relative to the airframe due to radar energy reflected from the blades themselves. The major portion of the propeller doppler-spectrum is always lower in frequency than the airframe line in a system which folds the spectrum about zero.
- (b) The return from the rear of a propeller consists mainly of periodic pulses of a doppler frequency proportional to the radial velocity of a discrete reflecting element on a blade. The reflecting element's radius on the propeller blade, hence its radial

velocity, is a function of viewing aspect and is most clearly defined within limits determined by the blade angles.

- (c) The doppler return from the front of a propeller contains frequency modulation as well as amplitude modulation. At small aspect angles, the propeller doppler spectral lines are grouped in the vicinity of the airframe doppler frequency, while at larger aspects they become spread over a much greater portion of the spectrum below the airframe line. Again, the spectral lines are spaced by the propeller blade modulation frequency."

While the Swerling I model assumes that RCS is constant during any one scan, the video output of an air traffic control radar may show considerable pulse-to-pulse variation due to the response of its phase detector and MTI to the doppler frequency components of the aircraft echo and, at some aspects, propeller amplitude modulation. System-induced fluctuations are just as important to the accurate calculation of probability of detection as those of the target, but must be considered separately.

Conventional delay-line MTI receivers make use of doppler shift to discriminate between fixed and moving targets on the basis of their instantaneous *radial* velocities. An aircraft passing through a terminal control area will exhibit zero radial velocity as the path becomes tangential to a circle centred on the airport radar. Because of the width of the MTI zero-velocity rejection notch, these aircraft will disappear for a finite distance before and after the precise abeam position. The distance over which such targets can move while remaining undetected is a function of three factors for a given radar:

- (a) signal strength above MDS;
- (b) target ground speed; and
- (c) target distance from the radar.

The most severe tangential fading will occur for low-speed, small-cross-section targets far from a radar employing low frequency and high PRF. The type of canceller (number of delay lines) and the use of feedback for velocity response shaping will also affect the severity of the tangential fade problem. Any radar parameter change which decreases the basic target signal margin will increase the width of tangential fades (for example, severe sensitivity time control attenuation, or sharp-cutoff antenna patterns). Quantitative knowledge of tangential fading may be useful in determining the cause of spotty radar coverage during instrument procedures, and should be employed as one trade-off in any consideration of siting a terminal radar off-airport (e.g., where the radar is to provide terminal service for a number of airports). From the point of view of flight safety, it is not the gaps in coverage of a controlled aircraft that are of primary concern, but rather the failure to see uncontrolled traffic on conflicting tracks. (Appendix A provides a good example of a mid-air collision where tangential fading probably was a contributing factor).

## 2.2 STATIC MEASUREMENT OF LIGHT-AIRCRAFT RCS

In 1973, a detailed program to measure static RCS (i.e., engine off, aircraft firmly positioned) of Cessna 150, Cherokee 140 and Super Cub aircraft was carried out at the Radar Target Scatter Division (RAT SCAT), Holloman Air Force Base, under contract to the United States' Federal Aviation Administration<sup>6</sup>. Data were taken at L, S and C-bands (three frequencies within the S-band), with vertical, horizontal and right-circular polarization. This section summarizes relevant results of the RAT SCAT measurements.

### 2.2.1 Low-Wing Cherokee 140

Figures 1 through 4 (reproduced from the FAA report) show the 2800 MHz static cross section of a Cherokee 140 for various aspects, as measured at RAT SCAT. Because of the logarithmic vertical scale, median values cannot be accurately extracted from these figures by eye; however, contours of equal median RCS are presented in Ref. 6, and it is from these that quantitative data were taken for the following discussion.

Figure 1 shows that, for  $0^\circ$  roll and  $0^\circ$  pitch, vertically-polarized 2800 MHz radars encounter a median RCS of just over 5 dBsm at nose aspect, and just under 5 dBsm at tail aspect, rising fairly steadily to over 20 dBsm for the 10 degrees each side of the beam aspect. Figure 2 (same conditions as Figure 1, except circular polarization) shows a general 5-6 dB drop in median RCS, which should come as no surprise\*; but the attenuation of the beam-aspect peaks of the RCS by about 15 dB is of some operational significance, as will be shown later. Figure 3 shows RCS versus aspect for a  $30^\circ$  bank (slightly more than a standard-rate turn for this class of aircraft). When viewing the upper surface of the aircraft ( $090^\circ$ ), median RCS is about 5 dB below the value for level flight; but, when viewing the lower surface of the aircraft ( $270^\circ$ ), the  $30^\circ$  bank angle has decreased the median RCS by about 10 dB. The effect of using circular polarization against a banked aircraft is shown in Figure 4. The previously-observed general loss of about 5 dB in RCS is again apparent, but the peak in RCS when viewing the upper surface of the aircraft from abeam, which had been visible only with linear polarization, is now observed with CP. Little increase in beam-aspect RCS is observed when viewing the lower surface.

To summarize, the use of circular instead of linear polarization significantly reduces the beam-aspect return from an aircraft in level flight, probably because of strong flat-plate-type reflection. At other aspects and bank angles, multi-scatterer reflection predominates, and the loss incurred by using CP is small.

---

\* Circularly polarized (CP) waves reflected from a flat plate or a spherical scatterer will have the sense of their polarization reversed, and will be attenuated if received using the same antenna that transmitted them. On the other hand, any odd number of multiple reflections (such as occurs at a corner reflector) will cause the polarization sense of the reflected wave to be unchanged. As both mechanisms contribute to the aircraft echo, the apparent aircraft RCS will typically be reduced by use of CP.

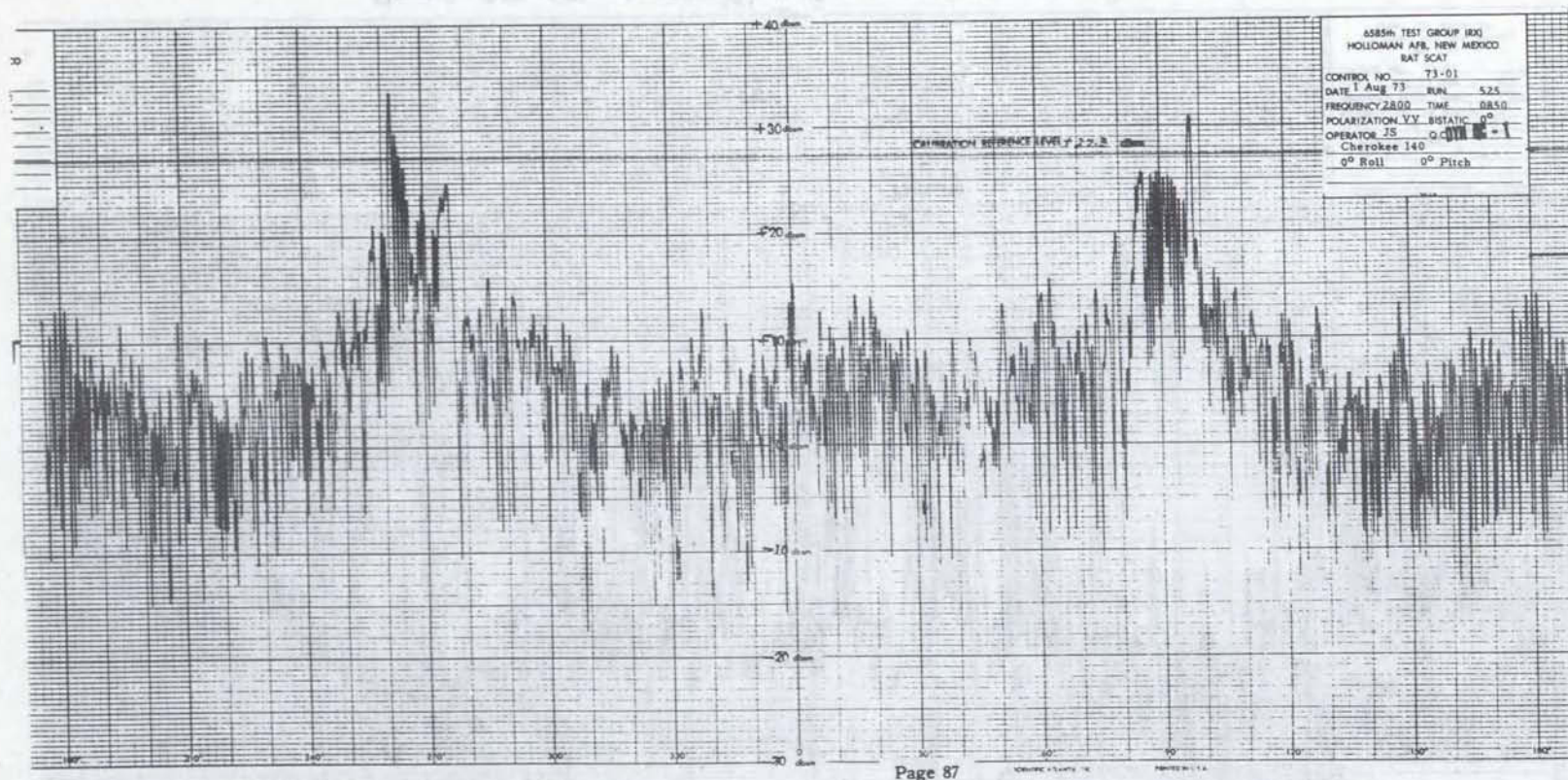


Figure 1. RCS of Cherokee 140; 0° roll, 0° pitch, 2800 MHz, Vertical Polarization

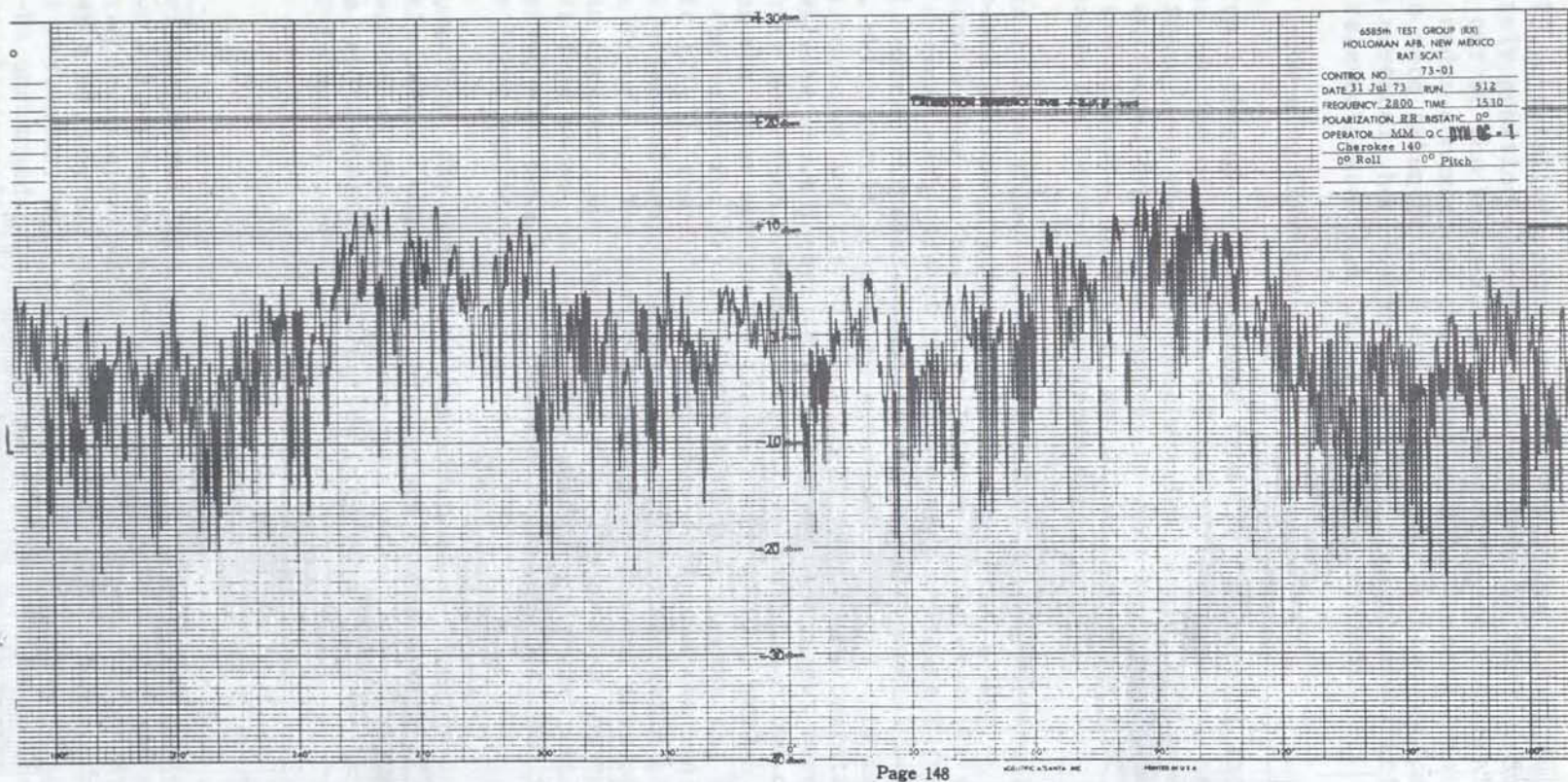


Figure 2. RCS of Cherokee 140; 0° roll, 0° pitch, 2800 MHz, Circular Polarization

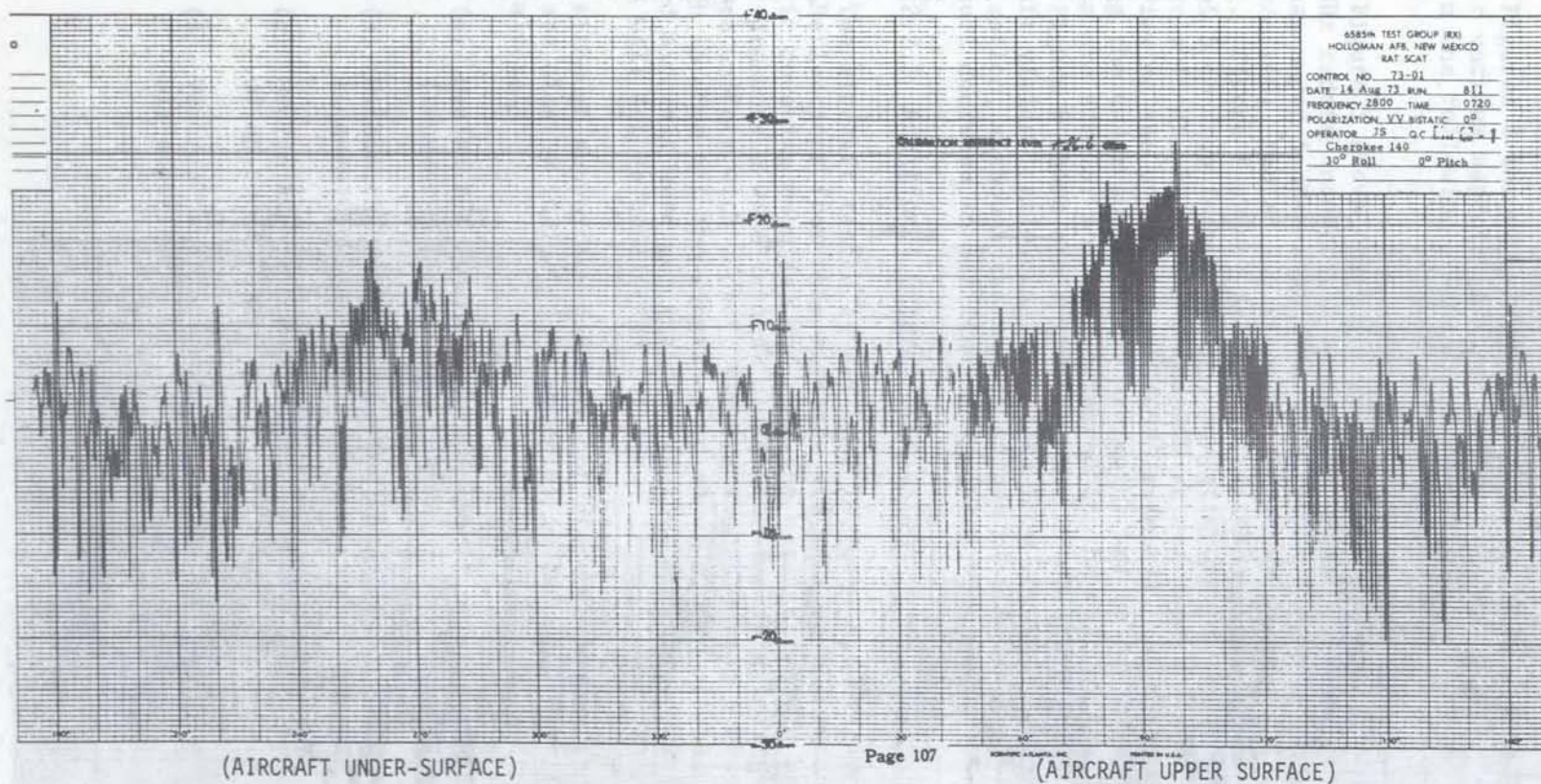


Figure 3. RCS of Cherokee 140; 30° roll, 0° pitch, 2800 MHz, Vertical Polarization

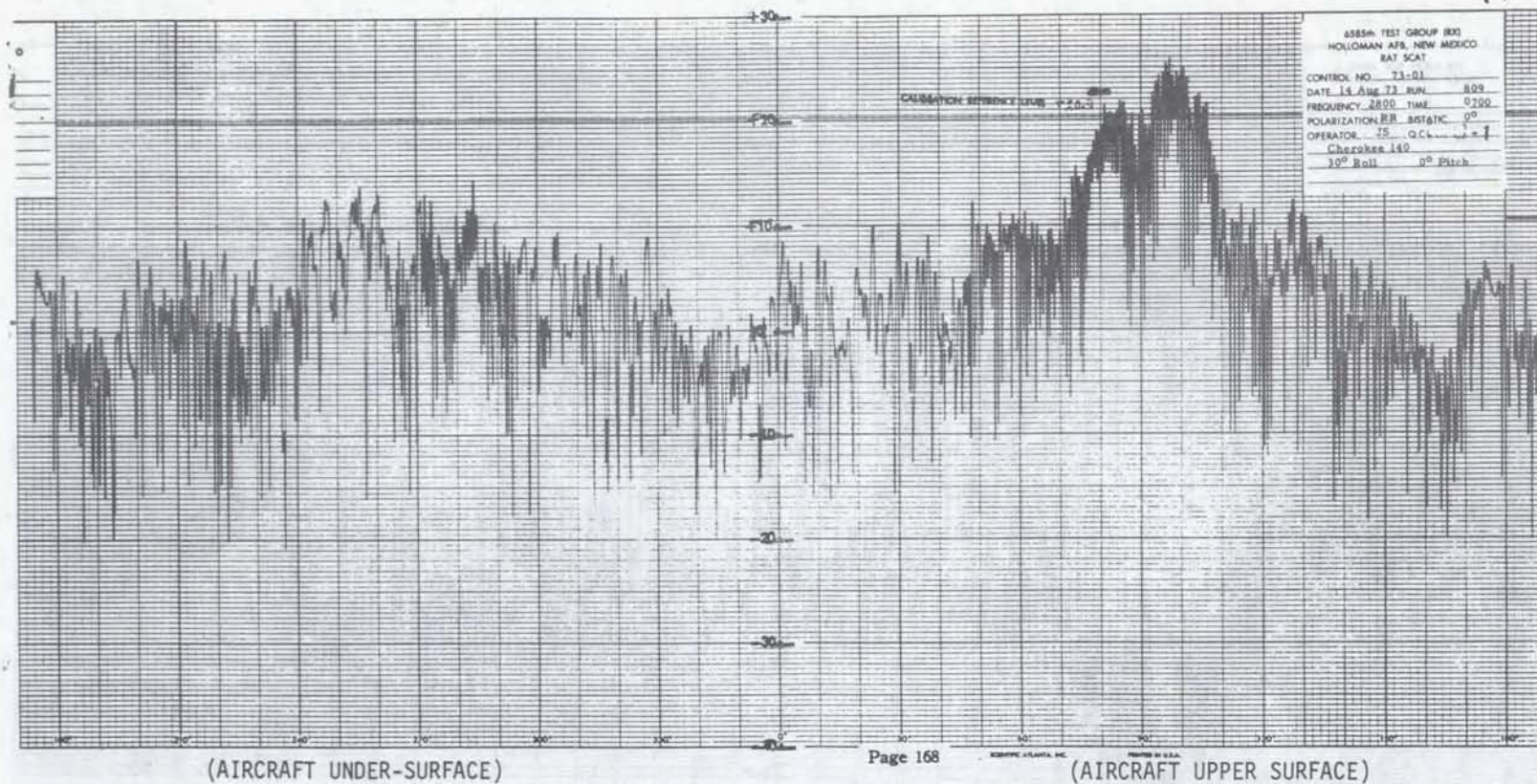


Figure 4. RCS of Cherokee 140; 30° roll, 0° pitch, 2800 MHz, Circular Polarization

### 2.2.2 High-Wing Cessna 150

Figures 5 through 8 show the 2800 MHz static cross section of a Cessna 150 for various aspects, as measured at RAT SCAT. As before, quantitative data in the following discussion are taken from median RCS contour plots in Ref. 6.

Figure 5 shows that, for  $0^\circ$  roll and  $0^\circ$  pitch, vertically polarized 2800 MHz radars encounter a median RCS of just over 5 dBsm at nose aspect, and just under 5 dBsm at tail aspect, similar in magnitude to that of the Cherokee 140. Median RCS rises fairly steadily to about 20 dBsm for the beam aspect. Figure 6 shows, again, that circular polarization results in a general 5 dB drop in median RCS, and attenuation of the beam-aspect RCS peaks by nearly 15 dB. Figure 7 shows RCS versus aspect for a  $30^\circ$  bank. Median RCS, viewing the upper surface ( $090^\circ$  azimuth), has risen slightly, while that viewing the under surface ( $270^\circ$  azimuth) has fallen by about 8 dB. These effects are similar to those observed in the case of the low-wing Cherokee 140. Figure 8 shows again that the use of CP against the banked high-wing aircraft yields little change in form from the results observed with linear polarization, although the median values of RCS observed for all aspects show the usual decrease in magnitude associated with CP.

### 2.2.3 Additional General Conclusions

The aircraft tested at RAT SCAT included a fabric-covered Piper Super Cub. Reflections from this aircraft are made up of components from the dielectric covering material and from the metal structure beneath. Since the latter presents a wide variety of lengths and orientations, the median RCS was more uniform with aspect, varying smoothly from 6 dBsm off the nose, through 15 dBsm off the wingtips, to about 4 dBsm off the tail. Since fabric covered aircraft were not employed in the CRC study, RAT SCAT results in this regard will not be considered further.

Although supporting data are not presented here, the following conclusions are clearly indicated by material in Ref. 6. With respect to the all-metal aircraft:

- (a) Median RCS for both CP and linear polarization is independent of frequency, from L to C bands;
- (b) Within the S band, only the fine detail of RCS versus aspect is frequency dependent;
- (c) Median RCS at S band was not appreciably affected by pitch changes of up to  $\pm 10^\circ$ ; and
- (d) Vertical and horizontal polarization yield near-identical RCS for all aspects.

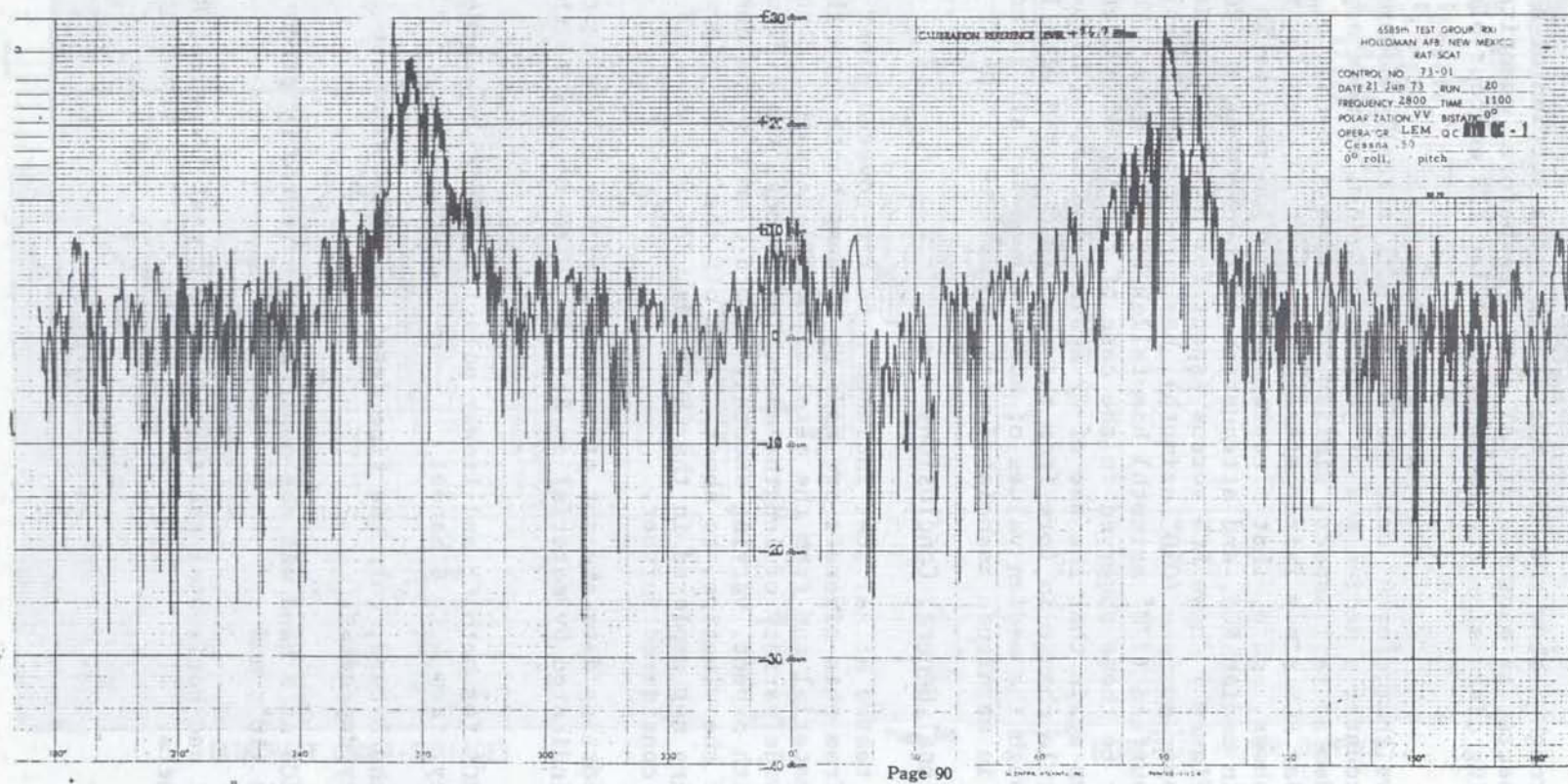


Figure 5. RCS of Cessna 150; 0° roll, 0° pitch, 2800 MHz, Vertical Polarization.



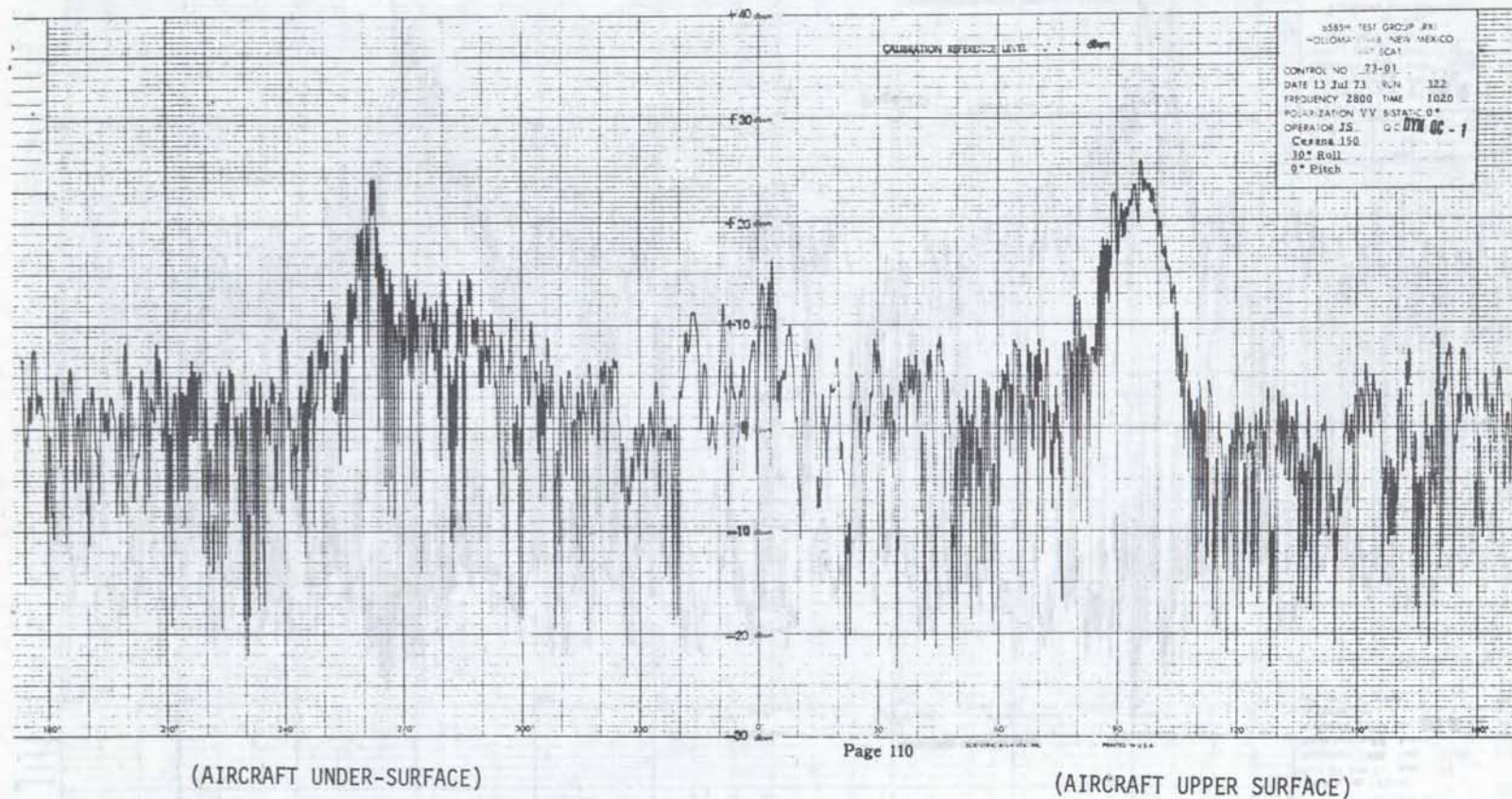
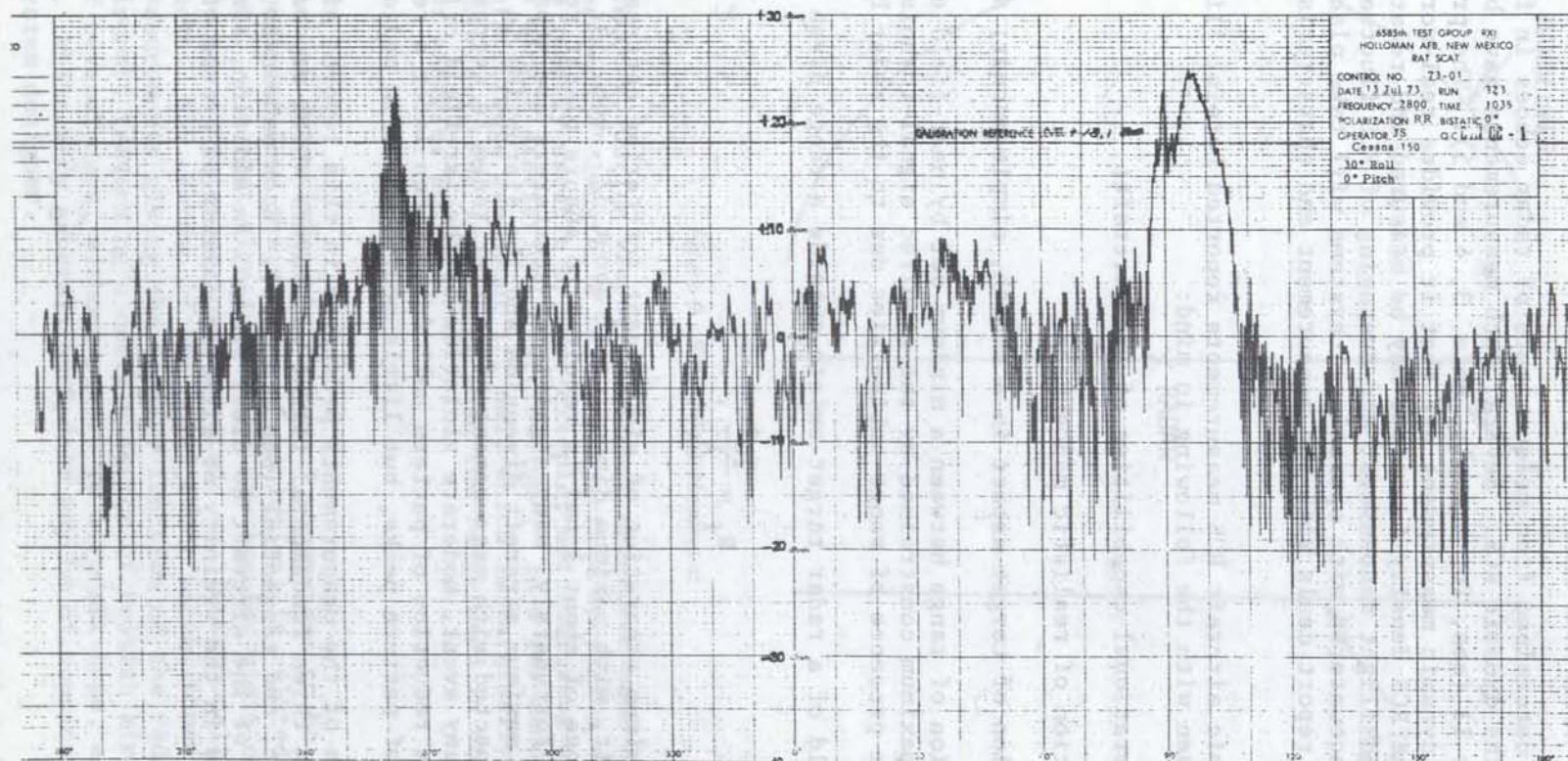


Figure 7. RCS of Cessna 150; 30° roll, 0° pitch, 2800 MHz, Vertical Polarization.



Page 142

Figure 8: RCS of Cessna 150; 30° roll, 0° pitch, 2800 MHz, Circular Polarization.

### 2.3 DYNAMIC RCS MEASUREMENT

When RCS is determined from measurements of radar echoes in flight, the result is called the dynamic RCS. Several such measurements have been reported since World War II (see, for example, Refs. 3, 4 and 5). The principal advantages of the dynamic measurement are that it provides real-world data; typical spectra and RCS density functions may be measured and related to frequently-executed flight manoeuvres; and averaging of RCS fluctuations similar to that encountered with operational systems will take place. The remainder of this report deals with the measurement and characteristics of the dynamic RCS.

In the dynamic aircraft RCS measurements reported herein, flight patterns were chosen with the following in mind:

- (a) the operational capabilities of the aircraft;
- (b) simulation of realistic manoeuvres;
- (c) variation of target aspect in a smooth, simple manner; and
- (d) variation of range between a minimum set by near-field effects, and a maximum constrained by the required signal-to-noise ratio and the presence of range ambiguities due to the radar PRF.

The far field of a radar target exists outside a range given by:

$$R_f = \frac{2D^2}{\lambda}, \quad (4)$$

where D is the maximum separation of significant scattering centres. For most light aircraft, with maximum dimension of about 32', eqn. (4) suggests that a minimum range of about 1 nmi is required to ensure planar reflections from the target. Fortunately, many significant scatterers are separated by far less than the maximum aircraft dimension and the disruption in data fidelity to be expected with measurement at shorter range is decreased accordingly. In any event, moderate violation of the far-field criterion results first in a reduction of pattern null depth, then later a reduction in the amplitude of pattern peaks, but little modification in median values<sup>5</sup>.

For purposes of the measurements presented in this report, aircraft were flown through three fundamental flight manoeuvres which may be described as overflight, arc, and tangential (See Figure 9). Each manoeuvre exposed a particular aspect of the aircraft to close study. In addition, almost all aircraft movements in the vicinity of airports consist of groups of these three manoeuvres.

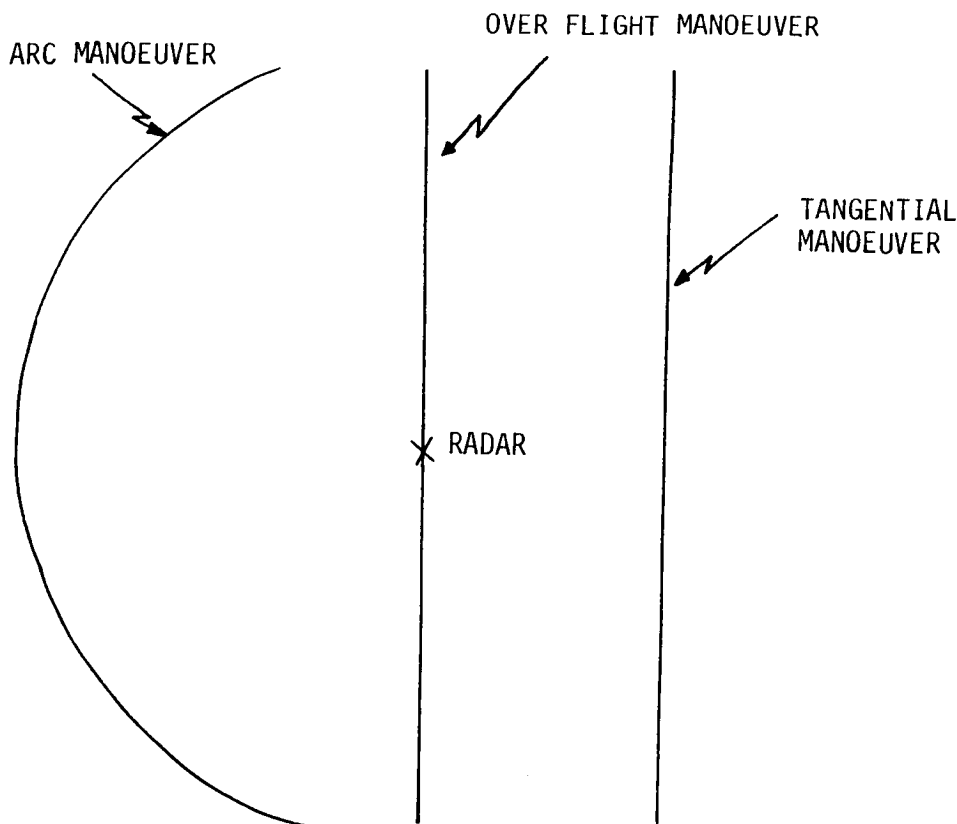


Figure 9. Basic Flight Manoeuvre

Data recorded during execution of each manoeuvre were broken into segments of "reasonable" length, a rather subjective operation designed to make results more readily useable by, for example, not including nose and beam aspects in a single statistical distribution\*. In a few manoeuvres, the minimum aircraft range was about 1/2 nmi, which is marginally less than the near-field boundary, but is greater than the range used in other measurement programs (for example, Ref. 6)

\* The problem of determining the number of parameters to be allowed to vary in an experiment (and their range of variation) is related to the end use of the data. A target signature study may require rigid control of aspect angle, whereas a system performance study may intentionally average over many aspects. M.P. Warden of the Royal Radar Establishment recently reported measurements giving the density function of the radar cross section of all aircraft traversing a certain sector of British airspace over a period of several days, without regard to aircraft type, altitude or position. While very general, such data may be of considerable interest to the system designer.

### 3. CRC RADAR DATA ACQUISITION SYSTEM

The CRC equipment used to study the detailed amplitude and spectral characteristics of light-aircraft radar reflections consists of a coherent S-band radar, and a Hewlett-Packard Model 2100 computer connected to the radar through a specially-designed interface.

A coherent radar maintains a consistent phase relationship over many transmitted pulses, so that the pulses reflected from a target are samples of a continuous microwave waveform. Coherency is necessary to obtain the complete target spectrum, including phase. Present interface hardware restricts the CRC system to coherency within a block of up to 2048 transmitted pulses. Pulsed-oscillator radars are incoherent, although a form of "pseudo coherency" is obtained by use of a COHO in MTI systems.

This section describes the radar, the radar-computer interface, and the data recording software. The method of analysis and discussion of results will be dealt with in Section 4.

#### 3.1 COHERENT LABORATORY RADAR

With the present CRC system, aircraft targets are acquired and tracked in azimuth and elevation by an operator using remote servo-controls to position the antenna. A TV camera is mounted parallel to the antenna boresight, and a monitor located near the servo-controls provides the visual reference needed.

Figure 10 is a functional block diagram of the radar transceiver. A 2970 MHz signal is pulse modulated with PIN switches, amplified in a travelling-wave tube amplifier, and transmitted. The received signal is amplified, shifted to a 60 MHz Intermediate Frequency, passed through a logarithmic amplifier and detected (using the 60 MHz reference) in a quadrature phase detector. The "limiter" shown in the receiver RF line protects the receiver front end during transmission, and does not affect normal-level received signals.

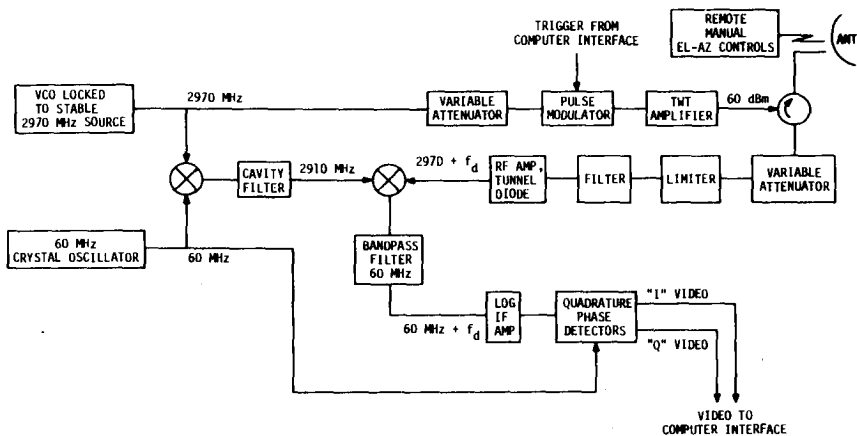


Figure 10. Functional Block Diagram, CRC Laboratory Coherent Radar

The radar parameters used during the light aircraft studies are listed in Table 3-1. The measured total amplitude transfer characteristic of the receiver is shown in Figure 11. Propagation delay through the IF chain is within  $\pm 1^\circ$  over the dynamic range of input illustrated. Consequently, error due to amplitude-to-phase conversion can be ignored.

TABLE 3-1

*Laboratory Radar Parameters*

Frequency	— 2970 MHz
Pulsewidth	— 1 $\mu$ sec
PRF	— 6828 Hz
Transmit Power	— 1 kW peak
IF	— 60 MHz logarithmic
Antenna	— parabolic reflector, $G = 35.5$ dB, manually steered by remote servo controls
Polarization	— vertical, transmit and receive
Losses (cable and guide)	— 5 dB one way
MDS	— -96 dBm (at receiver front end)

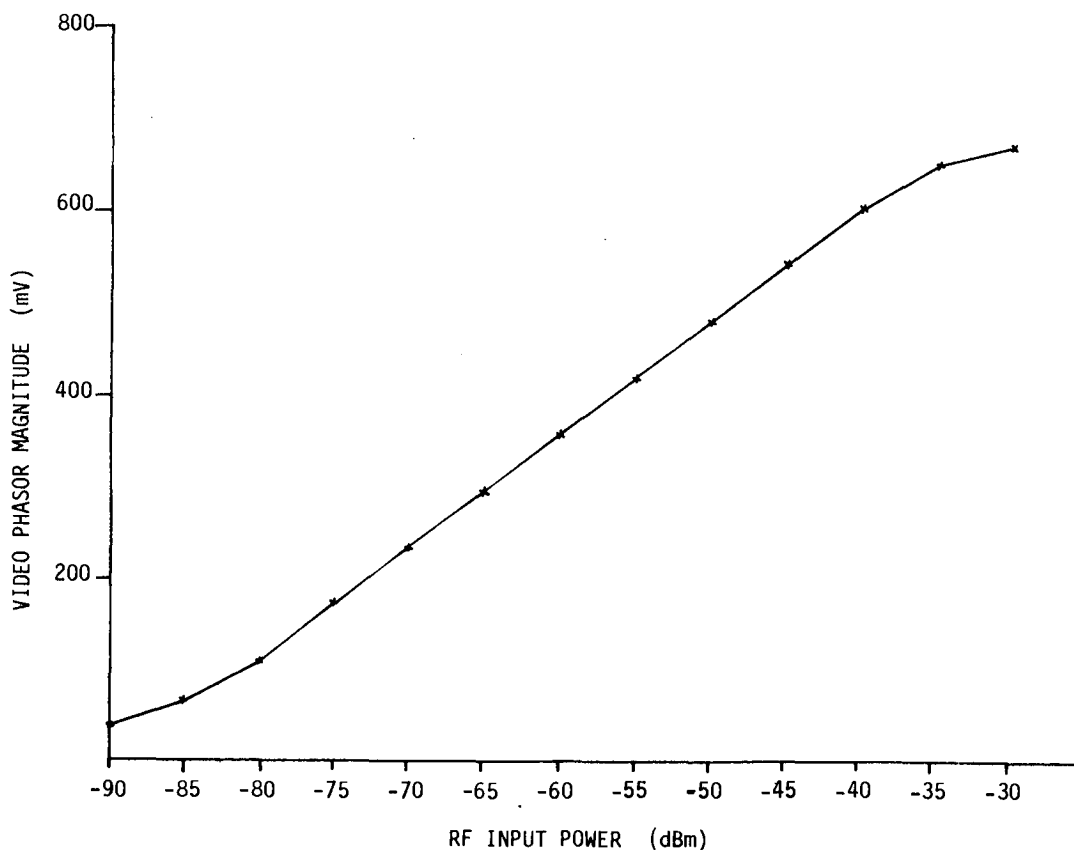


Figure 11. Radar Receiver Transfer Characteristic

### 3.2 RADAR-COMPUTER INTERFACE

Figure 12 is a functional block diagram of the interface between the laboratory radar and the HP2100 computer. The interface unit contains three registers: the PRI (pulse repetition interval) register, the range register, and the multiplexer address register. These registers are individually readable and writable under program control. By writing register contents, the computer controls respectively the radar trigger rate, the video sample range, and the identity of the video channel being sampled. Switches on the interface front panel allow manual operator intervention.

The Analog-to-Digital Converter used is a 10-bit bipolar ( $\pm 1$  volt) unit requiring a conversion time of 20  $\mu$ s. When two video channels ( $I$  and  $Q$ ) are being sampled at a high PRF and a constant or slowly varying range, most of the computer time is spent alternating the multiplexer addresses and reading data from the converter. With the interface shown in Figure 12, the maximum PRF which can be handled is about 13 kHz.

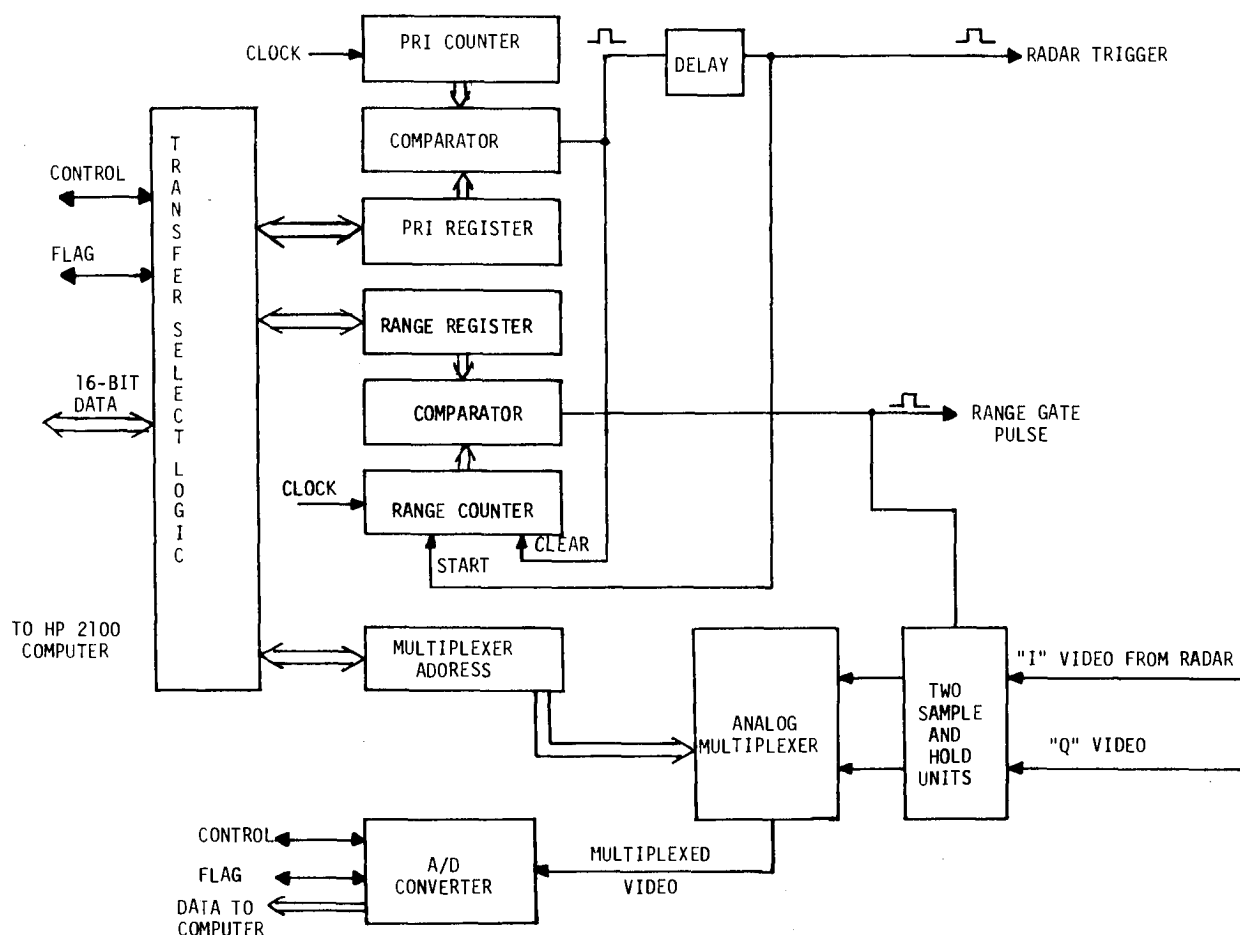


Figure 12. Functional Logic Diagram, Radar-Computer Interface

### 3.3 DATA ACQUISITION SOFTWARE

Software modules are used to calibrate the radar receiver, and to control the radar during the pulse-by-pulse recording of aircraft echo data. This section describes each briefly.

#### 3.3.1 Calibration Module

Each data recording run is preceded by receiver calibration, both to verify proper operation, and to account for varying gains within the receiver chain. With the receiver input derived from a 2970 MHz pulsed signal generator, the calibration module takes 100 samples of video for each input RF power level, incremented in 5 dB steps from -90 dBm to -30 dBm. At each input level, the mean modulus of the 100 in-phase and quadrature (I and Q) pairs is calculated and punched on paper tape with the corresponding input power level in dBm. The paper tape produced by this module, a permanent record of receiver gain and transfer characteristic, is retained with the recorded video data obtained in the subsequent experiment for use during data analysis.

#### 3.3.2 Recording Module

The recording module produces digital magnetic tape recordings of the I and Q video samples corresponding to successive aircraft hits. Up to 2048 consecutive hits are stored as a single physical tape record, with records separated in time by 0.3 to 1.5 seconds depending upon the mode of target range tracking employed. In addition to the video data, each physical record contains housekeeping words identifying the record number, target range, transmitted power, PRF, and RF attenuation applicable to the particular record. These parameters allow the calculation of cross section from the digitized video, using the radar receiver calibration tape.

Figure 13 is an abbreviated flow chart of the recording module. Once the range gate position is made to correspond with the target position initially, automatic tracking in range can be selected, and program control is held in the "wait and track" loop. The tracking algorithm is simple. Three range delays centred on the past target position and separated by 0.57  $\mu$ sec are tested. At each range, hardware spectral analysis of a short record is performed to allow fixed-clutter rejection. The range yielding the strongest non-zero-doppler return is chosen as the updated target position. A threshold test prevents the change of range gate position for very low amplitude returns, to allow the holding of constant range during tangential fades.

Data recording is started and stopped by setting or clearing a computer switch which controls entry into the "record loop" of Figure 13. While control is in the record loop, single passes through the track algorithm may be alternated with acquiring and writing physical records of video data.

Automatic range tracking of the target is optional, and the recording program module is fully compatible with manual tracking from the interface front panel. The automatic mode described was designed to adequately track the slow-moving light aircraft being studied; it would not be adequate for tracking aircraft at velocities much greater than 200 knots, due to the restricted iteration rate (required by magnetic tape recording), and the restricted range correction on a single iteration.

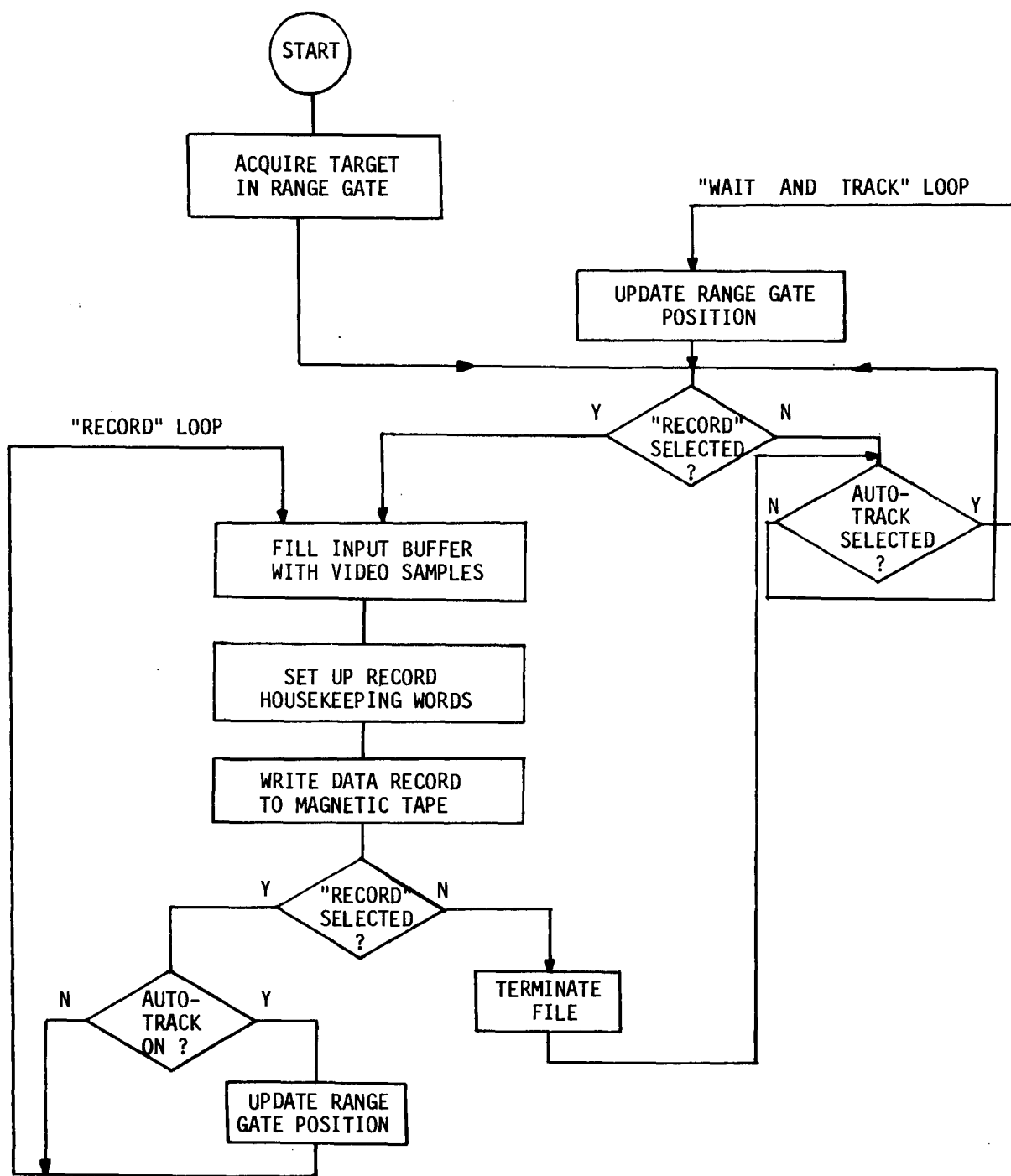


Figure 13. Functional Block Diagram of the Data Recording Module

#### 4. LIGHT AIRCRAFT COHERENT RADAR DATA

The CRC laboratory radar described in Section 3.1 was used to obtain recordings of radar video from a Cessna 177 Cardinal, a Cessna 172 Skyhawk, and a Piper Cherokee 140. Figure 14 shows the ground tracks flown by all aircraft. Each track was flown at an altitude of 500 ft. above the antenna, and was covered at least twice in a given recording session as a check on reproducibility of the data. An aircraft flying track 1 presents successively a broad range of aspect\* angles to the radar; on tracks 2 and 3, wing, nose, and tail aspects are presented.

\* The term "aspect" is used here to indicate the angle between the aircraft's longitudinal axis and the line between the radar and aircraft, both projected in the horizontal plane.

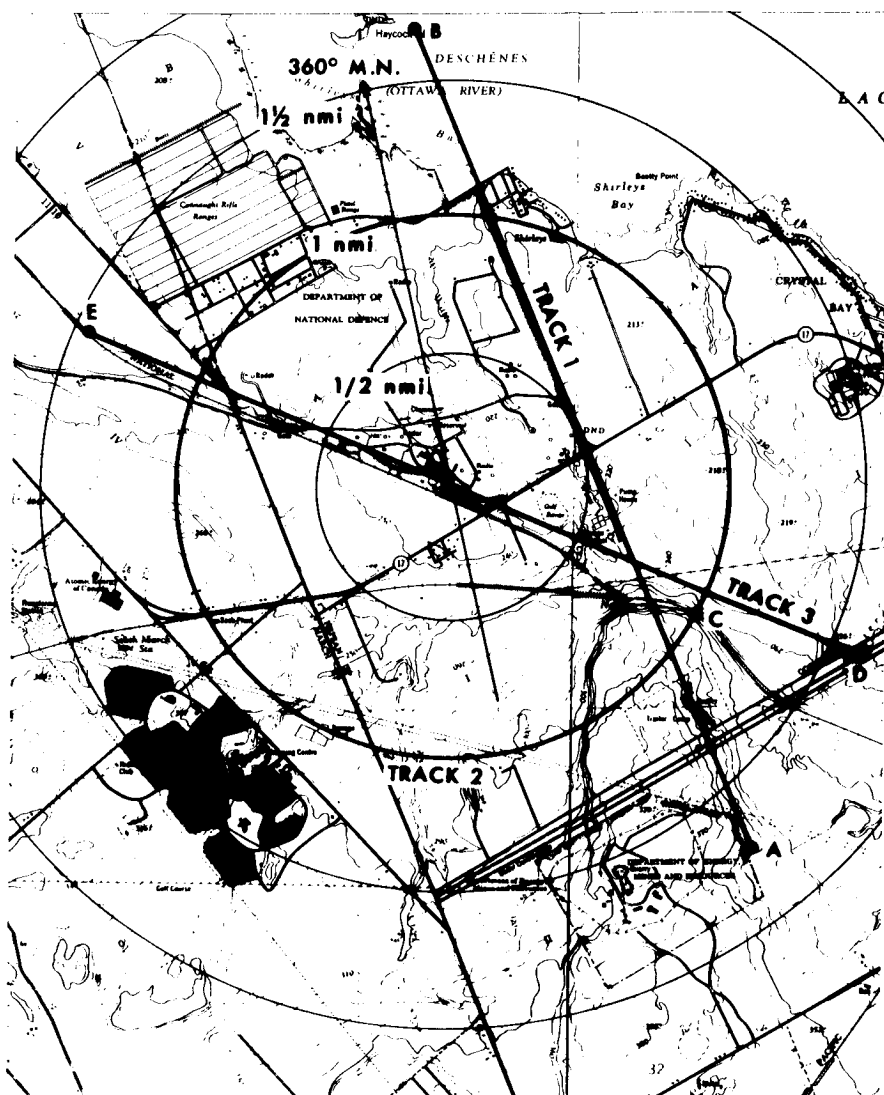


Figure 14. CRC Test-Flight Routes (The CRC radar is at the centre of the 1/2-nmi range rings)

Since the radar receiver has a nonlinear amplitude transfer function, all data analysis begins by using the calibration curve (relating the video phasor amplitude to received power) to "invert" the radar nonlinearity. The modulus of each complex video sample (I and Q pair) is uniquely related to the input RF power by this curve; moreover, the amplitude-to-phase conversion in the receiver has been shown to be negligible. Under these conditions, the effect of the nonlinearity may be removed from the data by replacing the amplitude of each recorded sample (pulse-by-pulse) with the square root of the actual input power in milliwatts. The phase of each sample is left unchanged. The resulting modified sample moduli have the units of volts across a  $1\Omega$  resistance; Radar Cross Section (RCS) is then calculated using the radar parameters of Table 3-1, the Radar Equation (eqn. (1)), and the target range which has been recorded with each data block. Doppler spectra computed from the modified data will have the intermodulation associated with the nonlinear receiver channel strongly suppressed, and the remaining spectral characteristics will be related to the aircraft scattering characteristics.

The subsections which follow discuss, in turn, the time-domain fluctuation of observed RCS, and the doppler spectral dependence on viewing aspect, for each of the three aircraft studied.

#### 4.1 TIME DOMAIN RCS FLUCTUATION

The fluctuation of radar return from an aircraft is commonly described in terms of the fluctuation of RCS; this eliminates the range dependence from the description, as well as eliminating the dependence on transmitter power and antenna gain. Two types of fluctuation will be discussed briefly by means of examples:

- a) fluctuation of the short-term mean RCS; and
- b) fluctuation of the RCS pulse-to-pulse, shown as probability density estimates.

##### 4.1.1 Short-Term Mean RCS

Figures 15 to 17 are representative time histories of the short-term mean RCS as the test aircraft flew along the tracks shown in Figure 14. In each case, the mean RCS is computed for a 150 msec record containing 1024 samples (long enough to include 5 complete propeller revolutions); and records are separated in time by about 1.5 seconds (limited by the computer processing speed).

Figure 15 is the observed mean RCS of the Cherokee J40 as it flew along track 1. The aspect of observation of the aircraft varies continuously along this track. Several aspect angles are indicated along the time axis; these are determined from the radial velocity (measured as doppler shift) and the estimated aircraft ground speed and crab angle. The most significant aspect dependence visible is the 12-15 dB increase in mean RCS in the narrow angular sector centred on the wing tip, in agreement with data presented in Section 2.2.1.

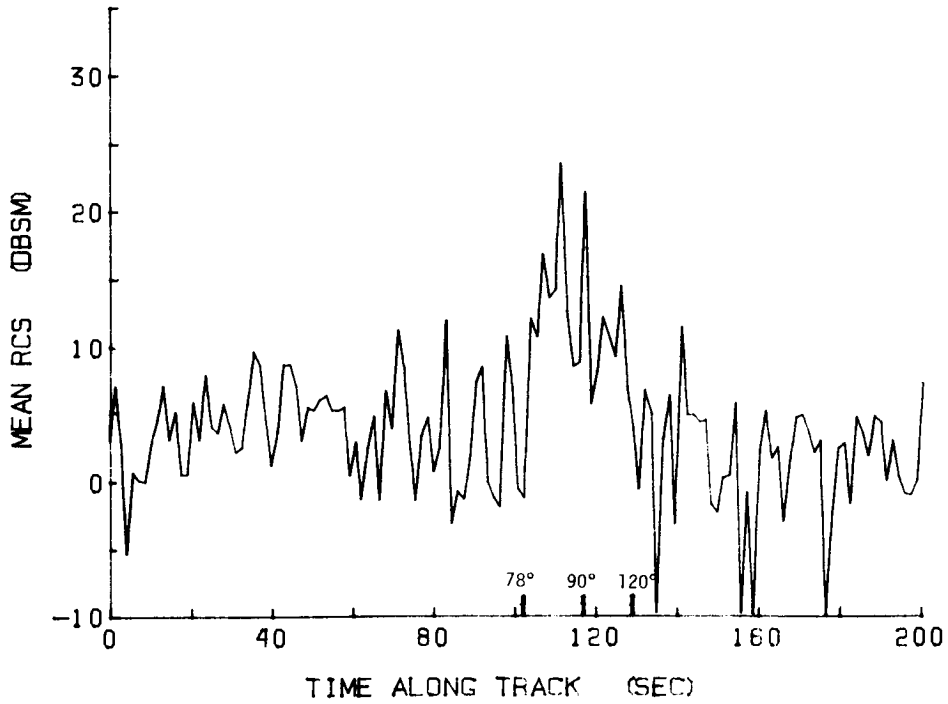


Figure 15. Short-Term Mean RCS of Cherokee 140, on Track 1

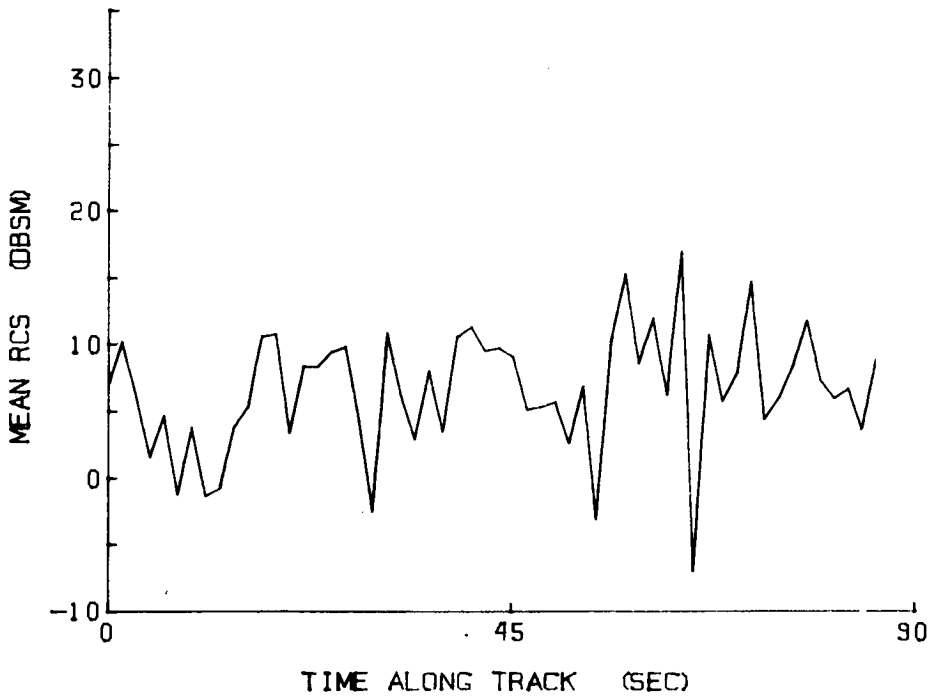


Figure 16. Short-Term Mean RCS of Cherokee 140, on Inbound Track 3

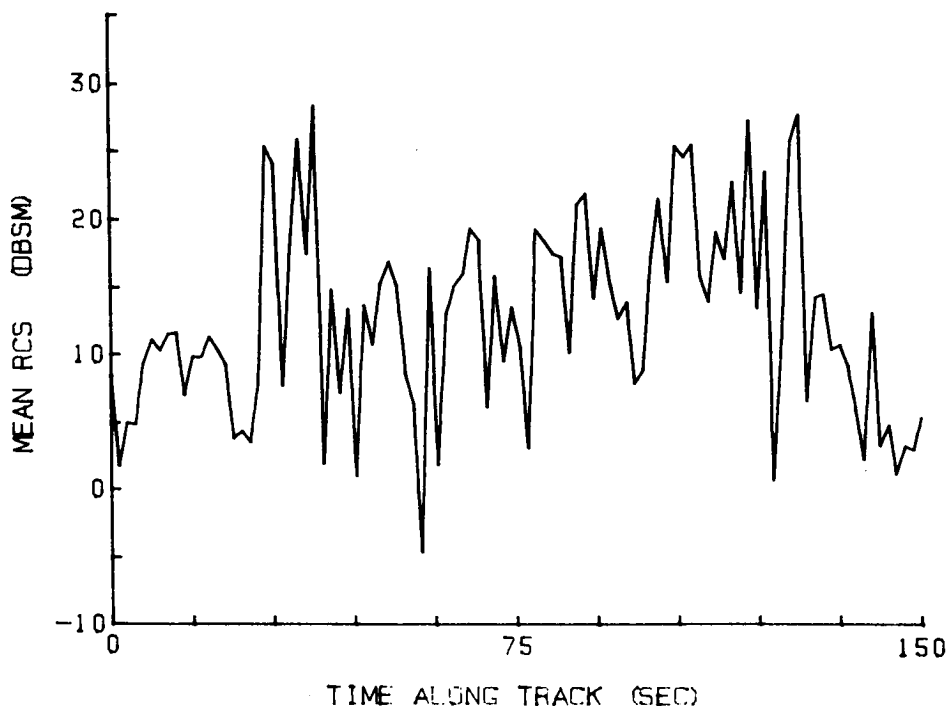


Figure 17. Short-Term Mean RCS of Cessna 177 on Tangential Track 2

Figure 16 shows the fluctuating mean RCS of the Cherokee 140, observed on the inbound section of track 3. On this track, the aspect angle is zero (nose-on). Short term mean RCS variations of up to 20 dB seen in this example are typical of those observed in both nose and tail aspects for all three aircraft.

Finally, Figure 17 shows the mean RCS observed using the Cessna 177 Cardinal, on a portion of the tangential track 2. On this track, the aircraft maintains a near 90° aspect with respect to the radar; the high RCS observed at 90° aspect (> 15 dBsm for a significant part of the observation) is a consistent feature of all three aircraft studied.

From examination of short-term mean RCS data (presented in the form of Figures 15 to 17) for several flights of each track by each of the three test aircraft, the following generalizations may be drawn:

- a) the dynamic RCS has a significant increase in mean in a narrow region about wing aspect. This is in agreement with the static RAT SCAT RCS measurements reported in Ref. 6 for three light aircraft;
- b) the short-term mean RCS fluctuates by as much as 10-20 dB over intervals as short as 1.5 seconds, for light aircraft performing simple manoeuvres. Normal handling on any of the test routes can produce changes of aspect of one degree or more per second; and the static RCS data shows that such changes could account for the observed fluctuations.

## 4.1.2 Dynamic RCS Probability Density Estimates

### 4.1.2.1 Segregation of the Data by Aspect

The extent of the fluctuation of dynamically-measured RCS is conveniently demonstrated by forming estimates of the probability density function of cross section. A need for some segregation of the data according to aspect angle exists: the cross section samples observed near  $90^\circ$  aspect clearly come from a population having a mean value higher than the mean of the remaining samples; also, the static RAT SCAT data suggests that somewhat higher median cross sections are likely to be observed at  $0^\circ$  and  $180^\circ$  aspects than in the intermediate regions between  $90^\circ$  and either of these extremes. For these reasons, the data for each aircraft were segregated according to projected aspect angle as shown in Figure 18.

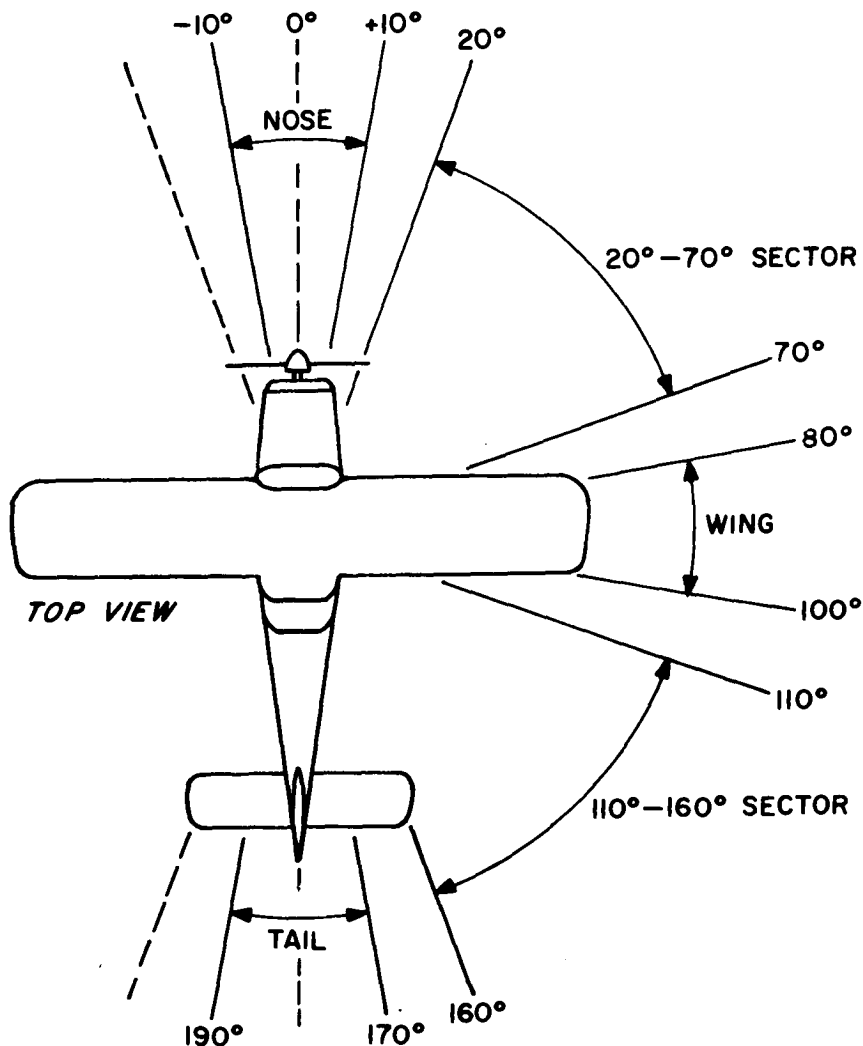


Figure 18. Angular regions selected for RCS probability density estimate. Both the line to the aircraft from the radar, and the longitudinal axis of the fuselage are projected in the horizontal plane.

For each aircraft, nose and tail-aspect data were taken from track 3 exclusively. The width of the aspect sector thus achieved is determined by the accuracy of flight and the crab angle needed to compensate for crosswind. Allowing for these factors, the angular width of the sectors involved is likely to be bounded by  $\pm 10^\circ$ .

Beam-aspect data is taken exclusively from selected recordings on tangential track 2. Selection was made to exclude records for which doppler shift showed that obvious gross track corrections were being made. Since the instantaneous relative wind vector is unknown, the allowed data is taken from the range  $90^\circ \pm 10^\circ \pm$  crab angle, with the crab angle less than  $10^\circ$ . The uncertainty in this angle and the sensitivity of median RCS to aspect near  $90^\circ$  will be evident in the beam-aspect density function estimates.

The "20°-70° Sector" and "110°-160° Sector" data included were selected from track 1 measurements. The angular regions included were determined by calculating the angle relative to track from the ground speed and mean doppler shift, and correcting, when necessary, for crab angle.

#### 4.1.2.2 Qualitative and Quantitative Results

Figures 19 and 20 are examples of RCS probability density function estimates derived from the segregated data. Each corresponds to a single aircraft type, a single aspect sector, and one recording flight. A density function estimate is produced by dividing the cross section range into bins of width  $0.2 \text{ m}^2$ , counting the number of cross section samples observed to fall in each bin, and plotting the suitably normalized count as a function of the bin position. The aircraft type and aspect are not shown, as these figures are intended only to illustrate features of the data which were generally observed.

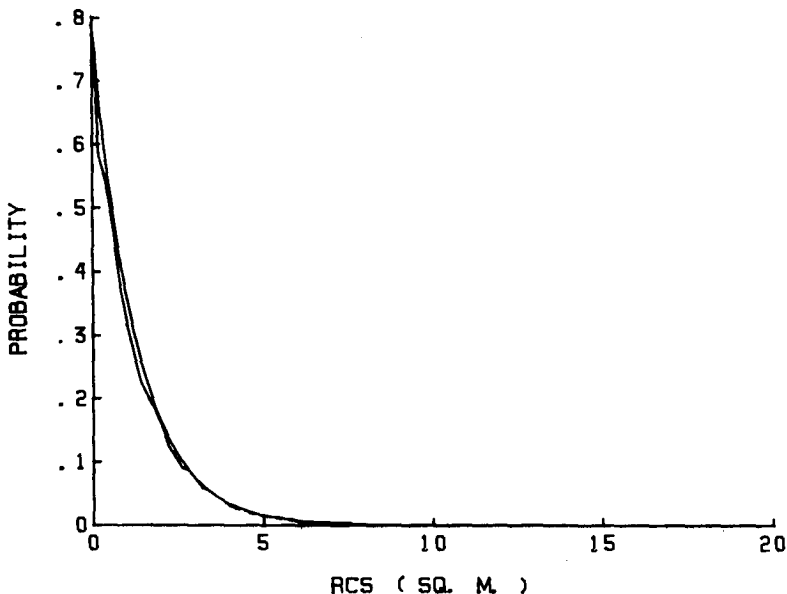


Figure 19. Experimental RCS probability density estimate. The overlaid curve is an exponential function with mean =  $1.3 \text{ m}^2$ .

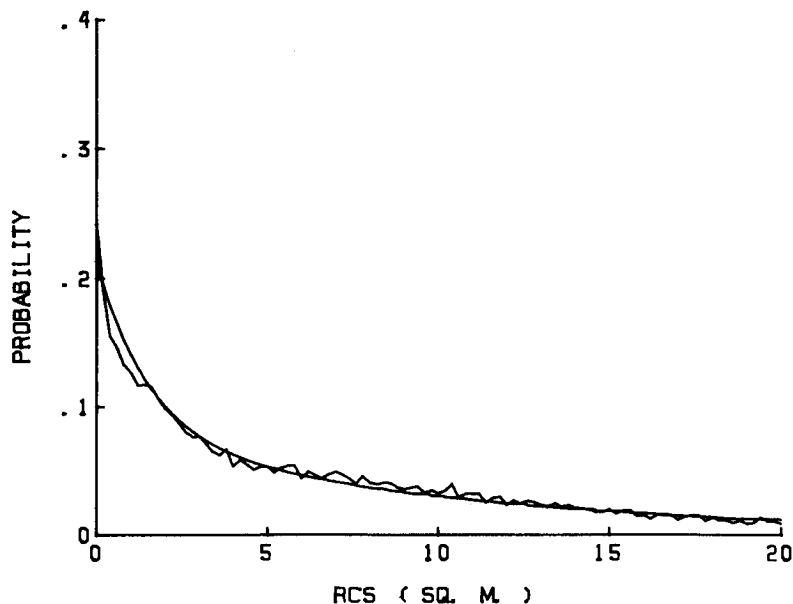


Figure 20. Experimental RCS probability density estimate. The overlaid curve is the weighted sum of two exponential functions of mean  $7 \text{ m}^2$  (0.9 weight) and mean  $0.5 \text{ m}^2$  (0.1 weight).

The physical justification for expecting an exponential distribution of RCS is discussed in Section 2.1.1. The experimental curve in Figure 19 is overlaid with an exponential curve having a mean value equal to the experimental mean. Excellent agreement between the two can be seen. The curve of Figure 20, however, cannot be adequately represented by a simple exponential function.

Certain experimenters have reported log-normal distributions for the RCS of some highly structured rigid scatterers when sampled in azimuth; however, as yet no satisfactory physical mechanism for the occurrence of log-normally distributed scattering has been found<sup>8</sup>. The log-normal distribution is suggested by the existence of very wide dynamic range in observed cross section samples, such as is shown in Figure 20. Wilson<sup>9</sup> has reported successful fitting of dynamic RCS density estimates for an unspecified propeller-driven aircraft at L, S and X-band, using the chi-squared distribution. His data were segregated into aspect (azimuth) sectors of  $10^\circ$  width, and were presented for aspects of  $20^\circ$  to  $160^\circ$ . Except at beam aspect, the chi-squared distribution with 2 degrees of freedom closely approximated his results. The chi-squared distribution with 2 degrees of freedom is identical to the exponential distribution of eqn. (2). In fact, the experimental curve of Figure 20, which employed data from a relatively broad range of aspects, can be very nearly approximated by the weighted sum of two exponential functions having different mean values. The mean values used, and the resulting analytic approximation to the experimental curve, are shown in Figure 20.

For all three aircraft studied, and for each of the gross aspect sectors (excluding only wing aspect), a single generalization can be made: the RCS probability density function estimated from the data for any flight is closely approximated by either

- a) an exponential function; or
- b) the weighted sum of two exponential functions having different mean values.

Appendix B contains a typical set of experimental RCS density plots for each of the three aircraft studied, in each of the 5 gross aspect sectors. The parameters of appropriate analytic approximations (as the weighted sum of exponentials), are presented with each curve. Curve fitting was done by a sequence of trials, using the eye to judge goodness of fit. No attempt was made to fit the curves for beam aspect, as these appear to be multimodal.

Repetition of single flights with any aircraft tends to show

- a) consistency in the mean values of the two exponential curves needed to fit the resulting RCS density estimate; and
- b) some variation in the weights required in summing the exponentials.

These results are reasonable, given the assumption that, for most aspect angles (with the possible exception of beam aspect), the effective RCS results from the vector summation of the returns from a number of scattering centres, none being dominant. This gives rise to exponentially distributed samples as small changes in aircraft orientation occur. Certain changes in orientation add or remove significant scattering centres by virtue of altered shadowing of the fuselage and propeller. Thus, the mean return changes while the mechanism needed for exponential scattering is still maintained. Consequently, a set of cross section samples obtained during a single flight segment may contain members of several distinct exponential populations. Since each aircraft pass is slightly different from others due to local wind and turbulence, the fraction of time spent in sampling each population varies from flight to flight. This gives rise to the variation in the weights applied to the two exponential curves which together fit the data.

The multimodal distributions of wing-aspect cross section have not been examined in detail. They probably arise through some combination of exponential scattering and the interaction of several large dominant scatterers. In level flight at wing aspect, an aircraft presents the large, relatively flat side of its fuselage as a radar reflector. Intuitively, this suggests that the criteria for exponential scattering may not be met.

The numerical results of the RCS probability density function study are summarized in Table 4-1. For each of the three aircraft, and each aspect sector (with the exception of wing aspect), four numbers are presented:

- a) Mean of "most likely" exponential distribution. The "most likely" exponential distribution is that exponential distribution comprising the largest fraction of all of the cross section samples taken in the study. The number given is the average of "most likely" mean values in several trials, and hence may differ slightly from the example in Appendix B;
- b) Fraction of the total observation in which the "most likely" exponential distribution occurred;

- c) Smallest mean occurring for a significant time. This is taken to be the smallest mean of an exponential distribution which was observed for 10% or more of a single flight; and
- d) The overall mean of all data available for that aircraft and aspect.

Table 4-1 provides a relatively simple description of the return from the three aircraft at most aspect angles. For example, the first line of the Cherokee 140 entry is interpreted: at nose aspect, about 80% of the observed RCS samples come from an exponential distribution with mean  $6.1 \text{ m}^2$ . However, within a few degrees of nose aspect a given observation may yield samples from an exponential distribution with mean  $0.5 \text{ m}^2$ , for a significant part of the observation. Such data are useful in analysis and testing of radar systems, and will be employed in Section 6.

The medians of the "most likely" exponential distributions reported in Table 4-1 for the Cherokee 140 are in agreement with the RAT SCAT medians reported for the same aircraft type in Ref. 6.

TABLE 4-1

*Summary of RCS Probability Density Data*

	MEAN OF "MOST LIKELY" EXPONENTIAL DIST' ( $\text{m}^2$ )	FRACTION OF TOTAL OBSERVATION	SMALLEST MEAN OBSERVED ( $\text{m}^2$ )	OVERALL MEAN RCS ( $\text{m}^2$ )
Cherokee 140				
Nose	6.1	0.8	0.5	5.1
20°--70°	2.6	0.8	1.0	2.5
110°--160°	1.3	0.8	1.0	2.2
Tail	2.3	0.7	0.8	3.0
Cessna 177 Cardinal				
Nose	7.5	0.6	2.0	5.4
20°--70°	1.6	0.8	1.0	2.4
110°--160°	1.5	0.9	1.3	1.5
Tail	1.6	0.8	0.25	1.3
Cessna 172 Skyhawk				
Nose	10.0	0.9	1.5	8.9
20°--70°	8.0	0.9	0.7	7.3
110°--160°	8.2	0.7	1.0	6.5
Tail	5.4	0.8	0.8	4.8

## 4.2 AIRCRAFT RCS SPECTRUM

The spectra shown in Figures 21 to 29 are selected examples of many computed from recorded data for the three aircraft. These examples were chosen to illustrate the behavior of target spectra, resulting from both amplitude and doppler modulation, as aspect angle changes. Each spectrum was

computed from a digital record consisting of a sequence of 1024 complex samples of the radar video waveform. The sample rate was 6828 Hz and the time duration of the record was therefore 150 milliseconds. Hanning weighting was applied in the frequency domain to reduce sidelobes, and this resulted in a degradation of the resolution to slightly worse than 7 Hz.

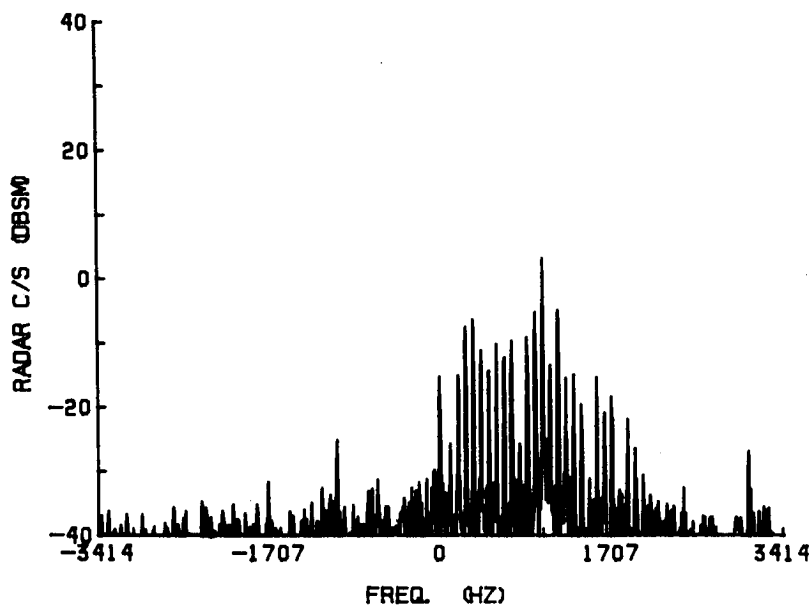


Figure 21. Doppler Spectrum, Cessna 172, 15° Aspect.

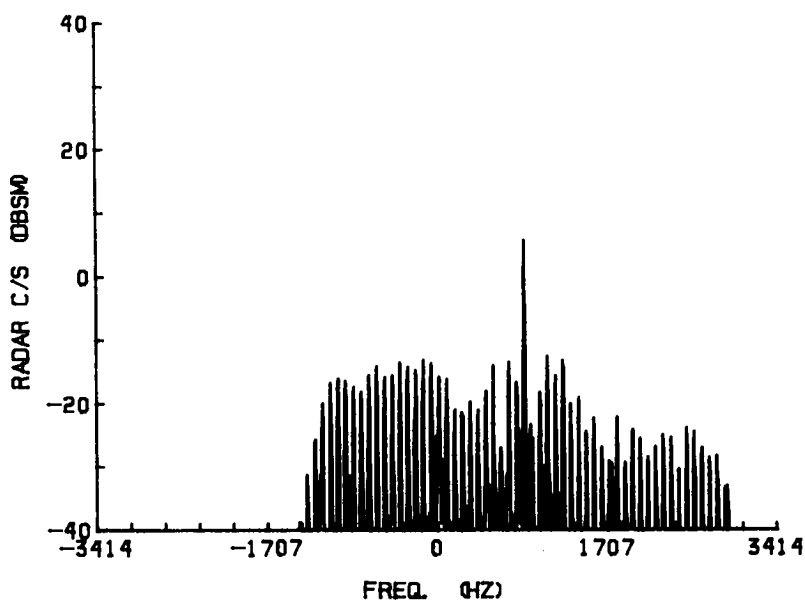


Figure 22. Doppler Spectrum, Cessna 172, 30° Aspect.

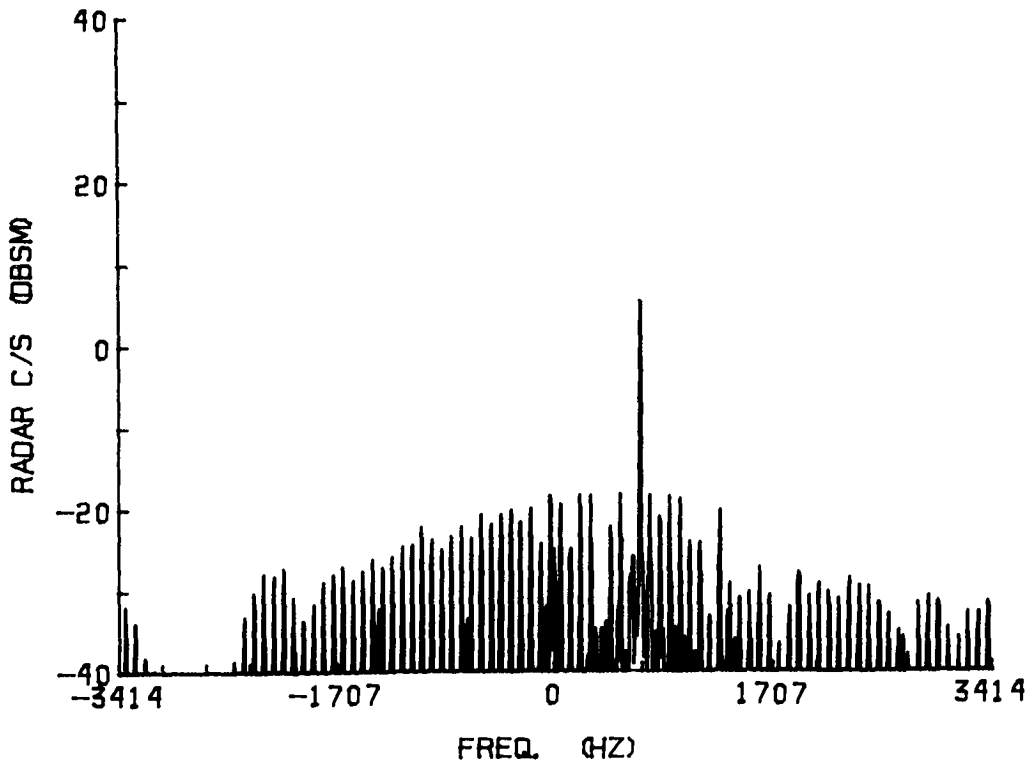


Figure 23. Doppler Spectrum, Cessna 172, 45° Aspect.

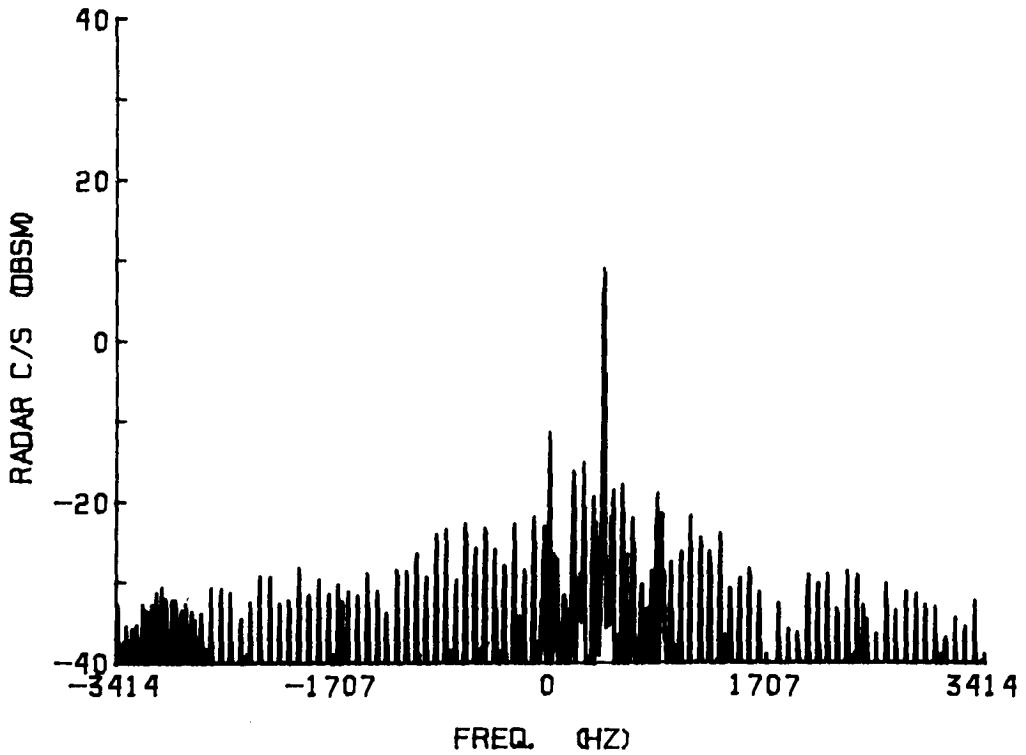


Figure 24. Doppler Spectrum, Cessna 172, 60° Aspect.

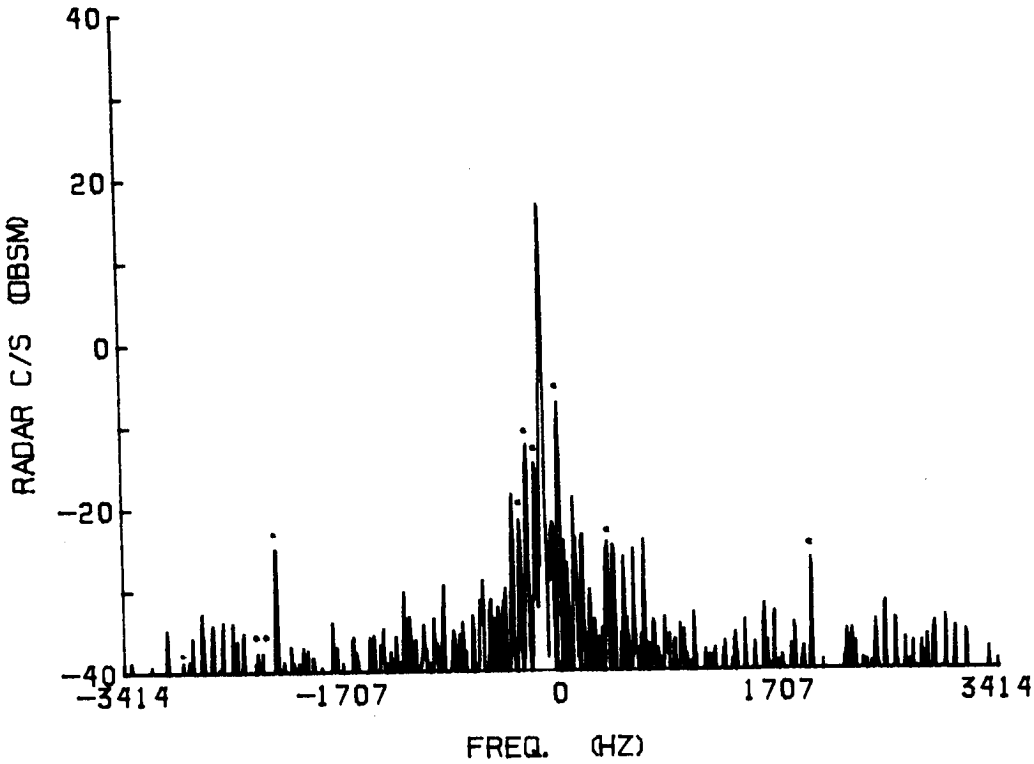


Figure 25. Doppler Spectrum, Cessna 172, 90° Aspect. The "dotted" lines are due to measuring system nonlinearities.

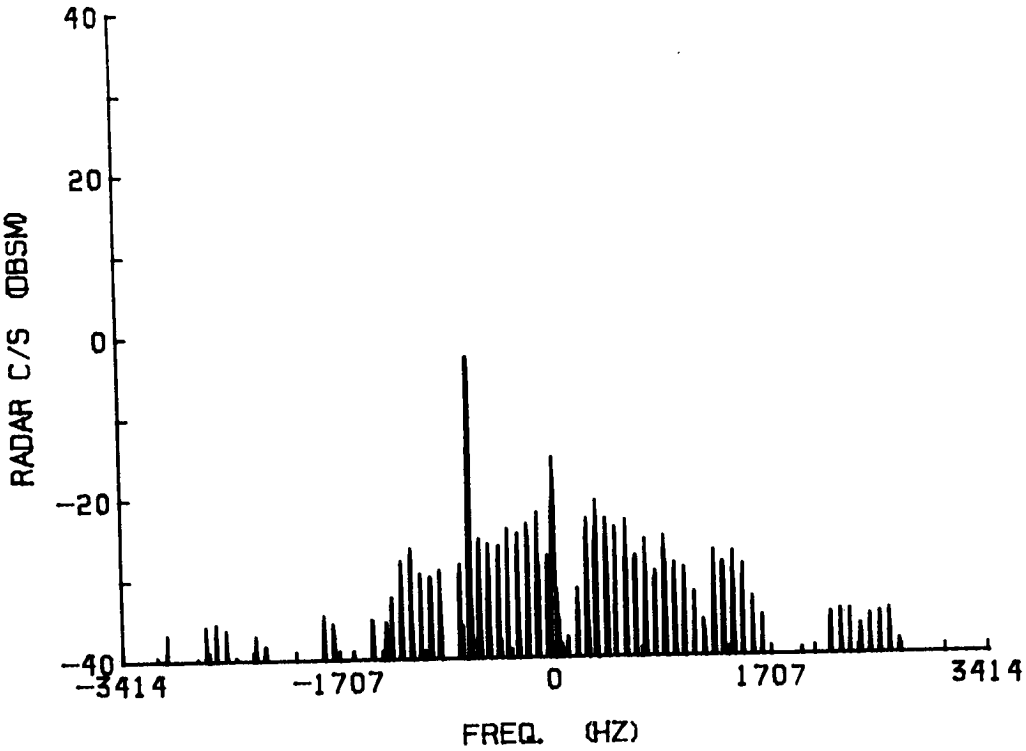


Figure 26. Doppler Spectrum, Cessna 172, 120° Aspect.

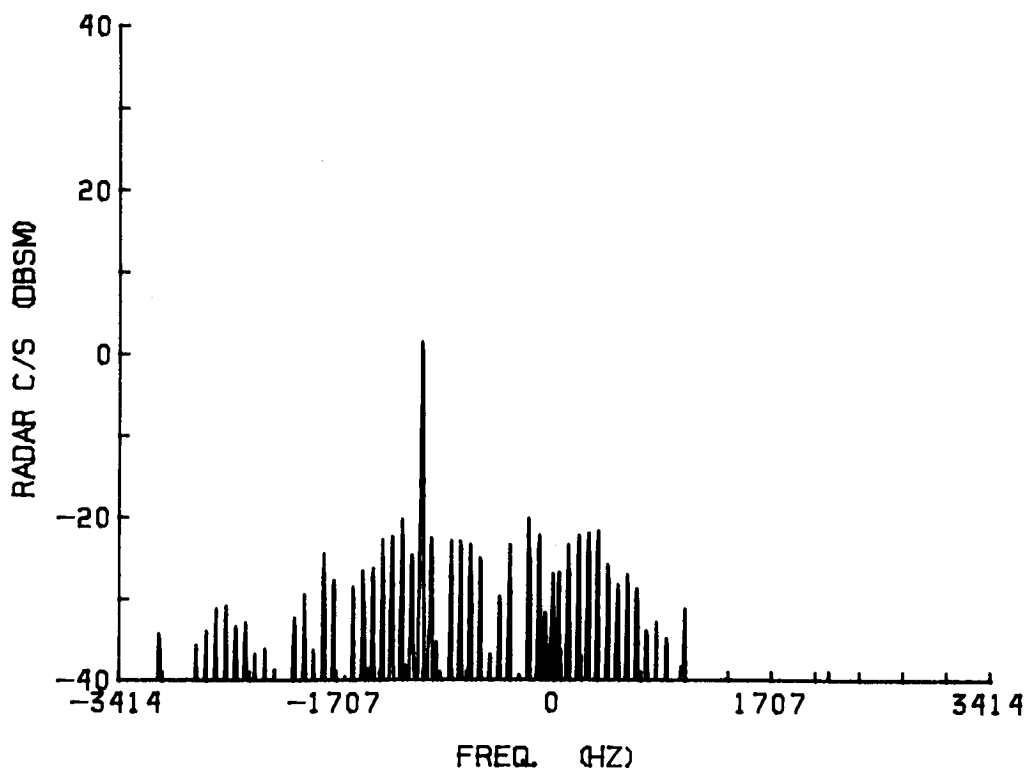


Figure 27. Doppler Spectrum, Cessna 172, 150° Aspect.

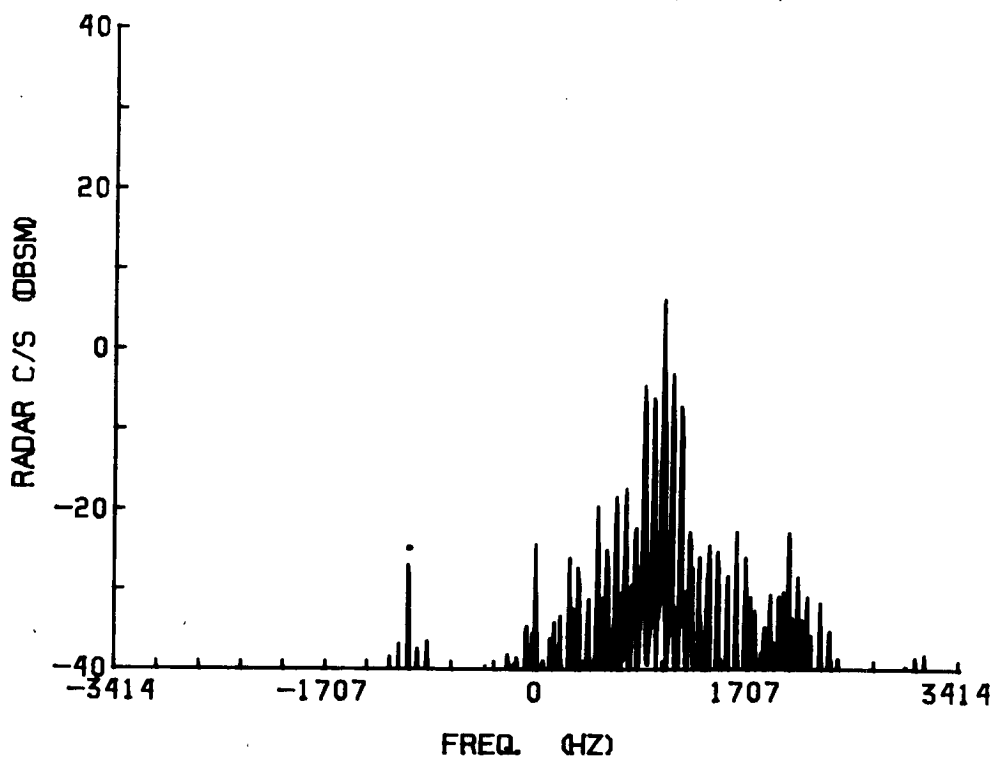


Figure 28. Doppler Spectrum, Cessna 177, Nose Aspect. The dotted term is due to measuring system nonlinearity.

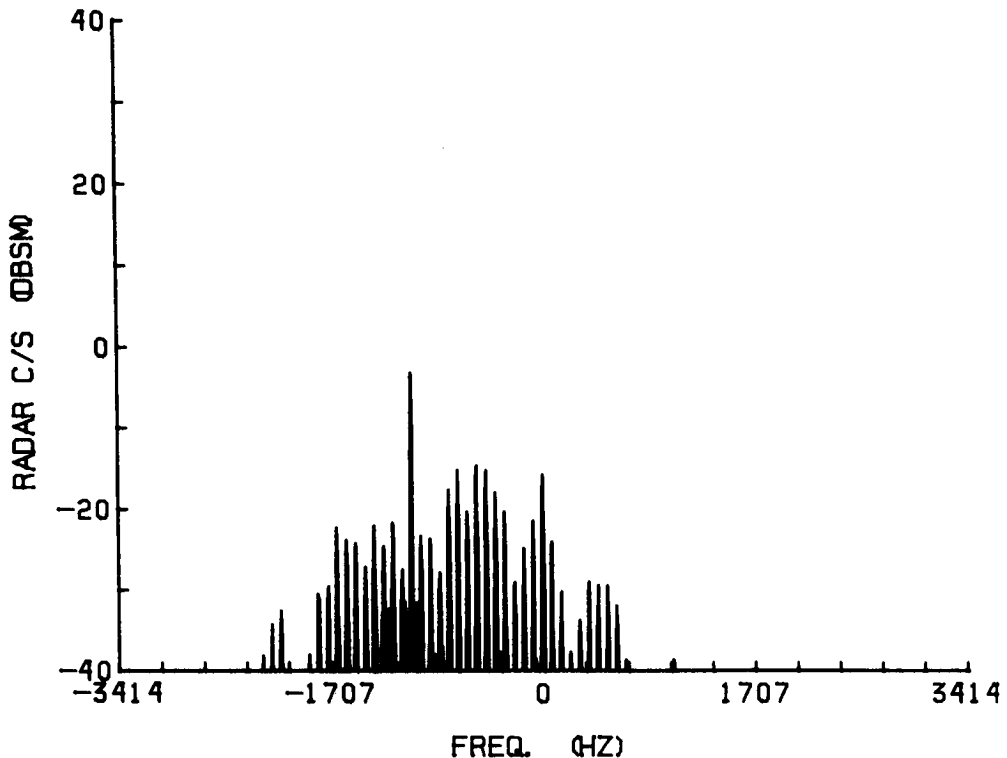


Figure 29. Doppler Spectrum, Cessna 177, Tail Aspect.

The vertical scale on these graphs is a radar cross section scale in dB relative to one square metre. It is not a density scale; that is, the integral over frequency does not give the total cross section. Rather, the total cross section is given by the sum of the values in each discrete frequency resolution cell. Such a presentation simplifies the interpretation of the line spectra, since the contribution of each line to the overall cross section is given by its y coordinate, provided the line is not significantly wider than the resolution cell. On this scale a target moving with constant velocity, and giving a perfect sine wave doppler, would generate a single spectral line, with the line amplitude giving the radar cross section of the target.

#### 4.2.1 Variation with Aspect

Figures 21 to 27 were computed from data recorded for aircraft at various points along Track 1 (Figure 14). The aircraft in this case was the Cessna 172, but similar spectra were obtained from the other two aircraft. Since the aircraft altitude was about 500 feet greater than that of the radar antenna, the radar beam was looking up at the aircraft at an angle to the horizontal varying from about  $3^\circ$  at the ends of the track, to about  $11^\circ$  at the point of closest approach. There were also changes in the effective angles of roll and pitch of the aircraft (relative to the line to the radar) caused by the altitude difference, but these were relatively small. The observation angles involved are considered not untypical for an aircraft passing an operational radar, since both the distance and altitude are normally greater.

Each graph was computed from data taken at a different point along the path and hence at a different aspect angle. (The term "aspect angle" is used here for the "projected aspect" discussed in 4.1.2.1.) Figure 21 shows the target spectrum for an aspect angle of about  $15^\circ$ . The strongest line, at about 1027 Hz, results from airframe reflection, and corresponds to a radial velocity of 100 knots. Other weaker lines are present, separated from the airframe line by multiples of 76.7 Hz. This frequency is equal to twice the 2300 r/min propeller rotation frequency. (The periodicity of any two-bladed propeller modulation corresponds to twice the rotation rate, since one half-revolution of the propeller is indistinguishable from the next.) Thus it is apparent that these lines result from the rotating propeller. The line at zero frequency is caused by fixed clutter, and RF leakage in the receiver.

Images of the airframe line are present at minus the true airframe doppler ( $-1027$  Hz) and also at plus three times the airframe doppler. These have been shown to be caused by residual effects of nonlinearity in the radar system, and are nearly 30 dB below the airframe line from which they arise.

Figure 22 is the spectrum for an aspect angle of about  $30^\circ$ . It can be seen that the propeller lines cover a greater frequency extent than before and are not spread symmetrically with respect to the airframe line. The airframe line has moved to a lower frequency, since the radial component of the aircraft's velocity is lower at this angle.

Figure 23, measured at an aspect angle of about  $45^\circ$ , shows even greater spread in frequency and lower individual line amplitudes. No immediate importance should be attached to the relative amplitudes of the airframe line and propeller lines, since the airframe line can change a great deal in amplitude in a short time as a result of its sensitivity to aspect angle. The propeller-line amplitudes do not display this sensitivity.

At an aspect angle of  $60^\circ$  (Figure 24) the lines are spread even further in frequency, and some aliasing occurs at the negative end of the frequency range (a consequence of the low sampling rate and the cyclic nature of the FFT). The amplitude of the lines has again decreased. The lines at zero frequency and at twice and three times the airframe doppler are, of course, not part of the true spectrum.

At an aspect angle of  $90^\circ$  (Figure 25), the very strong return from the airframe confuses the picture, since the undesired lines caused by the nonlinearity in the system, although well below the airframe line, are larger than the propeller doppler lines. Lines which have definitely been identified as undesired system-generated ones have been marked with a dot over them. The remaining lines are generally of low amplitude, but are spread over the entire frequency range.

At an aspect angle of  $120^\circ$  (Figure 26), the propeller lines have increased again in amplitude but their extent in frequency has decreased. Also, they are seen to extend more on the positive frequency side of the airframe line than on the negative frequency side. This is a reversal of the situation which occurred for aspects less than  $90^\circ$ . The spectrum for a  $150^\circ$  aspect angle in Figure 27 does not differ greatly from that of Figure 26, but the propeller lines have slightly greater amplitude and are less extensive in frequency.

To complete the picture, Figures 28 and 29 show the spectrum for aspects of  $0^\circ$  and  $180^\circ$ . These were computed from data on a different aircraft, a Cessna 177, which had similar spectra to those of Figures 21 to 27 at corresponding aspects. These nose and tail aspect spectra show relatively strong propeller lines and relatively small extent in frequency. The spectrum for tail aspect shows a wider doppler frequency extent than does the one for nose aspect. There is some possibility that this effect is not real, but is caused by an actual aspect angle differing from  $180^\circ$ . This angle was difficult to control because of cross winds and track errors, but the results seem to be consistent over a number of runs. A possible explanation for the wider spectrum at tail aspect is modulation of the propeller return due to blocking of the radar wave at some angles by the other parts of the aircraft.

#### 4.2.2 Relation to Spectrum to Time Domain Characteristics

A look at a time history of the cross section from pulse to pulse should aid in understanding the spectra just presented. An example is given in Figure 30, which shows the radar cross section pulse-by-pulse within one record (1024 complex points). The data were obtained using a Cessna 172 at an aspect angle of  $30^\circ$ .

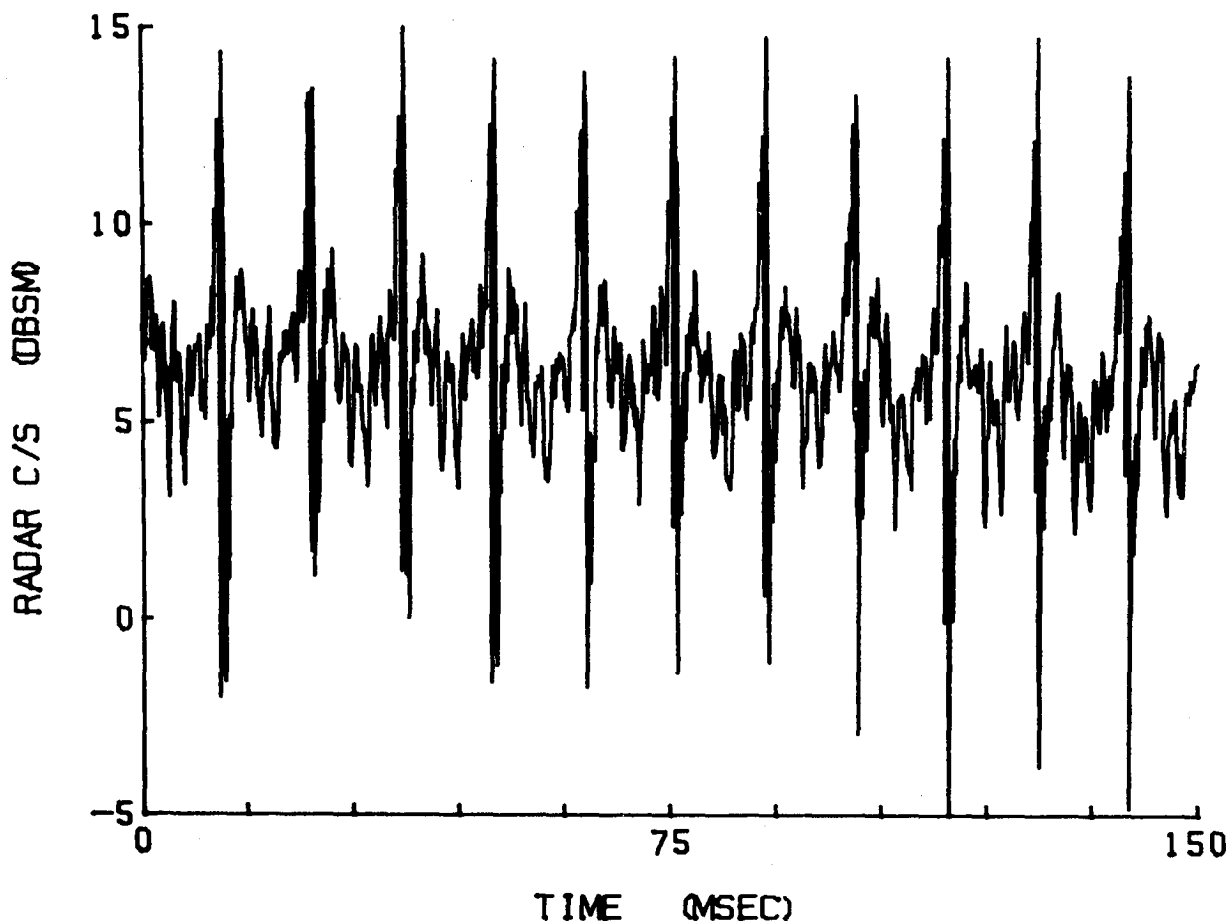


Figure 30. Example Time Record of RCS of Cessna 172 at  $30^\circ$  Aspect.

A short duration excursion is seen to occur about every 13 milliseconds, a period which corresponds to one-half rotation of the propeller. Gardner<sup>4</sup> attributes the short-duration propeller return to specular reflection at some angular position of the propeller. In fact, this mechanism would lead to the variation of spectral bandwidth reported by Gardner for aspects from  $0^\circ$  to  $60^\circ$ , and is in qualitative agreement with corresponding data in Section 4.2.1. However, the "specular patch" mechanism is not likely to apply at aspect angles of  $60^\circ$ - $120^\circ$  for example, since the edge of the propeller is then illuminated, and the width and radius of curvature of the reflecting patch must then be significantly less than the radar wavelength. An additional mechanism suggested in the following paragraphs is in qualitative agreement with the experimental results.

As a propeller rotates, a position will exist such that the radial axis of each of the blades is in turn perpendicular to the line of incidence of the radar energy. At these angles, reflections (not necessarily specular) from points along the length of the blade will add in phase, giving a maximum overall return from the blade. For two-bladed propellers, this condition will be satisfied twice per revolution. At an aspect angle of  $0^\circ$  the propeller blades are perpendicular to the line to the radar throughout the entire rotation (assuming zero aircraft pitch angle). As the aspect angle increases, the propeller spends less and less time within any given angle about the perpendicular until at  $90^\circ$  this time is a minimum. Since the shorter the duration of the signal peak the wider will be the resulting spectrum, we would expect the width of the spectrum to be minimum for nose and tail aspects and maximum at  $90^\circ$ . This is in fact the situation seen in Figures 22 to 27.

Figures 28 and 29 for nose and tail aspect still show a spectrum of significant width. This is due in part to the apparent pitch angle (the aircraft was higher than the radar), but variations in propeller cross section due to rotation through the direction of polarization of the incident field may also play a part, as may the shadowing of the airframe by the propeller (nose aspect) and of the propeller by the airframe (tail aspect).

Within the impulses shown in Figure 30, a high frequency oscillation can be seen. This, no doubt, is a result of the phase changes (doppler) of the propeller return relative to the airframe return. Phase variations appear as RCS fluctuations, since the returns from airframe and propeller add when in phase and subtract when out of phase. If the propeller were perfectly symmetrical, we would not expect such phase variations, since as one blade was moving away from the radar the other would be approaching, and the net effect would be no phase change. However, an examination of a typical two-blade propeller shows that for aircraft aspect angles between  $0^\circ$  and  $90^\circ$  (but not right at these angles) the blade which is moving relatively away from the radar presents a greater projected area to the radar than does the blade moving relatively toward the radar, while for angles between  $90^\circ$  and  $180^\circ$  the reverse is true. Thus the resulting doppler should be mainly negative with respect to the airframe doppler in the first case, and positive in the second. This effect is clearly seen in Figures 22 to 27.

#### 4.2.3 Effect of Propeller Doppler on MTI Performance

The portion of the spectrum due solely to the propeller was extracted by a program which computed the spectrum for each record, removed the strongest

(airframe) line, and computed the cross section corresponding to the total remaining power. The data for each aircraft as it flew Track 1 (Figure 14) was processed in this way and the results plotted as a function of aspect angle (computed from radial velocity). An example is shown in Figure 31. Each plotted point was computed from one 1024 complex-word record. Unfortunately, near  $90^\circ$  aspect, the very strong airframe line generates false lines which dominate the spectrum, making it difficult to extract the cross section of the true propeller doppler lines. Therefore it was necessary to remove some of these from the plots, leaving a scarcity of points near  $90^\circ$ . The trend visible in Figure 31 was common to all 3 aircraft: the overall propeller cross section has maxima near nose and trail aspects, and a minimum near  $90^\circ$  aspect. This might be expected from a simple look at the projected area of the propeller as seen by the radar. Unfortunately, it is just at an aspect of  $90^\circ$ , where the airframe doppler is near zero, that the propeller cross section is least. It is in this area that we might have hoped for some improvement in MTI response as a result of the rotating propeller.

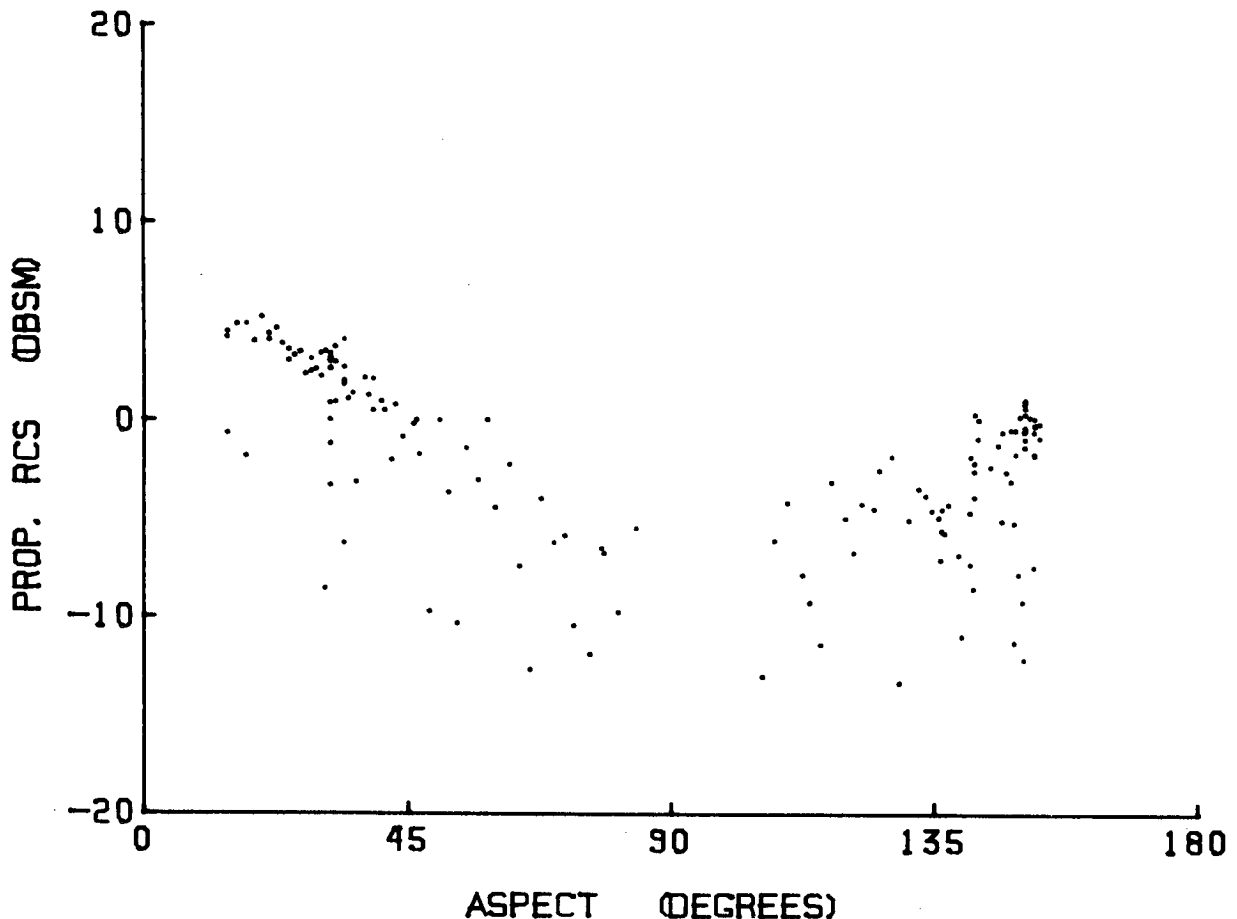


Figure 31. Variation of propeller RCS (computed from power in propeller modulation spectrum) with aspect. The data shown are for the Cessna 177.

#### 4.2.4 Summary of Spectral Properties

A number of general conclusions may be drawn from the spectra presented in this section.

- a) The rotating propeller causes the generation of a number of lines separated from the airframe line by multiples of twice the rotation rate.
- b) The magnitude of the propeller lines is greatest near nose aspect, decreases to a minimum at  $90^\circ$  aspect, and increases again to a maximum (apparently a lower one than the one for nose aspect) near tail aspect. The largest of these lines is smaller than the airframe line.
- c) The extent in frequency over which these lines exist is minimum at nose aspect and increases to a maximum at around  $90^\circ$  aspect. It decreases again to a minimum at tail aspect, although it appears that this is not as low a minimum as for nose aspect.
- d) The propeller doppler lines are not generally spread symmetrically with respect to the airframe line, but have a "centre of gravity" which is below the airframe line for aspect angles less than  $90^\circ$ , and above the airframe line for angles between  $90^\circ$  and  $180^\circ$ . For all aspects, therefore, significant scattering areas in the propeller move in opposition to the direction of motion of the airframe, to or from the observer.
- e) The total power in the propeller lines has a maximum near nose and tail aspect, and a minimum near wing aspect. The maximum at tail aspect appears smaller than that at nose aspect.

Generally, the spectral width of the target echo can be expected to alleviate MTI blind speed losses associated with constant-PRF radar systems, and velocity-response losses in the case of staggered-PRF radar systems. However, as a consequence of (b) and (d) above, and as shown in Figure 31, little relief from tangential fading can be expected.

The assumption inherent in the Swerling I target model, that amplitude does not fluctuate greatly within a given look (or scan), requires that signal bandwidth be less than the reciprocal of the dwell time on target (e.g., 17 ms for the ASR-5 radar). The spectra suggest that the Swerling I correlation requirement is violated for most aircraft aspects, and Figure 30 tends to confirm this view.

### 5. OPERATIONAL-RADAR DATA ACQUISITION AND ANALYSIS SYSTEM

This section describes hardware and software developed at CRC to facilitate recording of radar-target data in the field, and its later analysis in the laboratory using a dedicated HP 2100 minicomputer. While the digital recording equipment had been developed some years before, and has been used previously in a number of applications, the software was written specifically for the research reported herein.

## 5.1 CRC DIGITAL TARGET RECORDER

The digital tape recording system used to transform radar signals to a recorded digital data format compatible with the computer is described in this section.

The recorder uses a modified B-scan display for target acquisition and tracking (see Figure 32 below). This display scans in rectangular coordinates, giving Azimuth versus Range on the y and x axes respectively. Only signals within a range interval  $\Delta R$  and azimuth interval  $\Delta A$ , as shown in Figure 32(b), are recorded. The position of the recording window is set by a track ball that is integral to the recorder. Manual displacement of the track ball moves the displayed window for tracking purposes. In practice, because of spotty radar performance and the need to be sure of accurately tracking "misses" as well as "detections", raw SSR video, displaced in range from the skin paint by a constant distance, was added to the B-scan display to permit precise tracking, even during target primary-radar dropouts.

An 8-bit number giving the peak video voltage within the recording-window range interval  $\Delta R$  is acquired for every transmitted pulse. At the end of each scan, 16 8-bit words of housekeeping data and the accumulated video data (up to 496 words, depending on the PRF and the window width  $\Delta A$ ) are transferred as a discrete record to 9-track computer tape.

In the present trials,  $\Delta R$  was usually set to 1.2 nmi, or about 30 times the correlation time of the receiver video noise (ASR-5 video bandwidth is specified at 2 MHz). If the video input is gated to the recorder's peak detector for 30 times the correlation time of the input, the peak detector will, on average, choose the largest of 30 uncorrelated samples. Lewis, in an unpublished Technical Memorandum, has shown that this "collapsing loss", in the present instance, has a value of 6 dB.

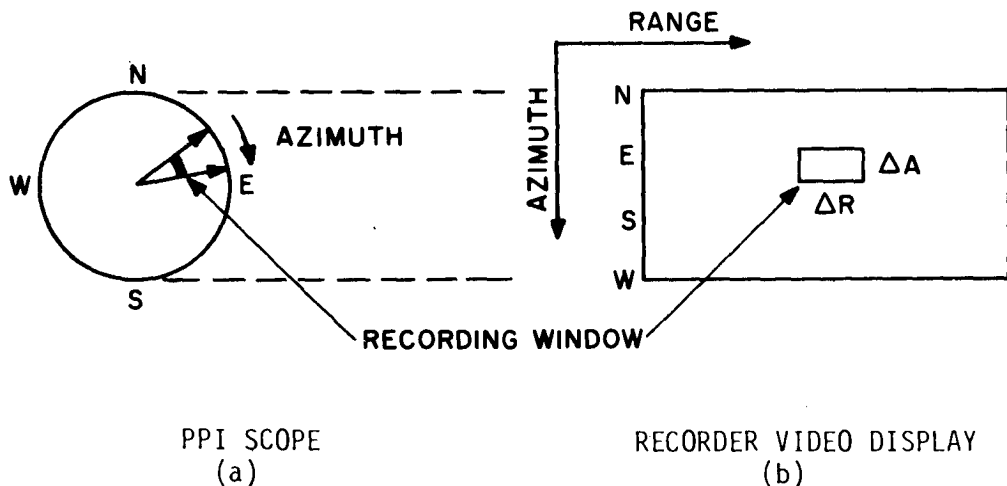


Figure 32. B Scope (b) – Versus – PPI Scope (a)

## 5.2 ANALYSIS SOFTWARE

Computer tapes resulting from the ASR-5 radar experiments were analyzed on a specially-configured HP 2100 computer system employing 32K memory, disc-operating system, magnetic tape unit, CRT X-Y display, and an on-line hard-copy plotter. The following paragraphs describe the software modules written for this task.

### 5.2.1 Track Plotter

This program plots the actual aircraft track flown, to any requested scale. It may be used to produce properly-scaled overlays for maps or PPI pictures of ground clutter (clutter profiles). By setting a sense switch on the computer, discrete locations along each track may be flagged. A table is output on the system teletype, giving the time, bearing and range of the points so flagged, and the track, distance and ground speed since the preceding flag.

### 5.2.2 Interactive Visual "Quick-Look" Routine

This computer program presents, for each scan, amplitude-versus-azimuth signal data, together with selected housekeeping parameters, on a CRT X-Y display. It is used for screening recorded blocks of data, and as a type of data editor, which can, under the operator's control, transfer segments of data to a disc file for later detailed analysis; or, it can produce permanent paper plots of signal histories during designated scans.

Figure 33 shows two examples of recorded range-gated video, as seen using the "Quick-Look" routine. Figure 33(a) is the video voltage produced as the ASR-5 antenna beam scans by a strong isolated, point target. The slight asymmetry of the target response (resulting from the radar's integrator) may be seen. Figure 33(b) is the same point target adjacent to an area of distributed clutter. In both cases, a first threshold has been set as shown, and a simple sliding-window detector (as described in Section 5.2.3) would have no difficulty determining the true azimuth of the point target. MTI video recorded using radar systems without integrators typically shows rapid fluctuations within a scan, but these have been largely eliminated here by the ASR-5 integrator.

### 5.2.3 Automatic Detection Routine

A software implementation of a plot extractor was employed to give a repetitive, unbiased and relatively accurate measure of the observed detectability of the aircraft return on each scan. The algorithm employed was the familiar double-threshold, sliding-window detector. For purposes of the analysis presented in later sections, the first threshold was set at three times the mean video voltage within each recording window (including noise, clutter residue, and signal), averaged over azimuth to contain a high proportion of noise and clutter residue. The second threshold was set to one-half the number of pulses per sliding window, which was, in turn, set to the number of hits per 10-dB beamwidth.

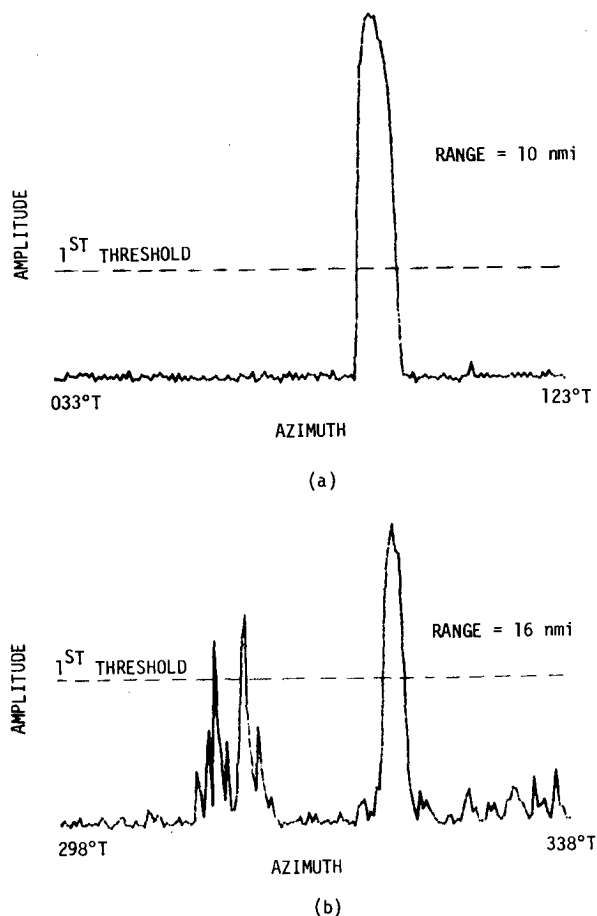


Figure 33. Range-Gated ASR-5 Video

#### 5.2.4 Probability of Detection Calculation Routine

In the context of a measurement problem, "instantaneous probability of detection" has no meaning. For the present work, the scan history of the target, consisting of "detections" and "misses" as determined by the previously-described automatic detection routine, was analyzed in overlapping blocks of 50 scans during a given manoeuvre. In this way, each "miss" within a block would lower blip/scan ratio by 0.02. To provide smoothing of results, the 50-scan block was advanced only 10 scans between computations, resulting in correlation between adjacent values of blip-scan ratio. Blake<sup>2</sup> defines the blip-scan ratio as the fraction of scans on which a blip is observed, averaged over a small range interval (consistent with its useage here). He further notes that this quantity "corresponds to the probability of detection when the observer's integration time is less than the scan period of the radar" (again, the case here).

With the Ottawa ASR-5 radar, averaging over 50 scans corresponds to averaging over 3 minutes and 20 seconds of real time, or 5-1/2 nmi of movement for a 100 knot aircraft (see parameters in Table 5.1). The 50 scan data

interval is a compromise, large enough to provide the required averaging (leading to repeatable, easily interpreted results), but small enough so that, normally, two or more unrelated detection factors do not occupy the interval at the same time (i.e., it may not be desirable for a tangential fade and strong target suppression by clutter to be averaged in the same data interval). In each of the sequences reported here, data were screened manually to ensure that false alarms and undesired aircraft in the recording window had not significantly corrupted probability of detection results.

TABLE 5.1

*Approximate ASR-5 Radar System Parameters (Ottawa)*

Peak Transmitted Power	400 kW
Pulse Length	0.833 $\mu$ s
Wavelength	0.107 m
PRF (average)	1158 Hz
PRI stagger	9:11
Antenna Gain (peak)	34.0 dB
Antenna Azimuthal Beamwidth	1.5°
Antenna Elevation Beamwidth	5.0°
Antenna Height	60 feet
Antenna Beam-Peak Elevation	1.8°
Antenna Polarization	vertical
Antenna Scan Rate	15 r/min
Receiver Bandwidth (IF)	4 MHz
Receiver Bandwidth (video)	2 MHz
Receiver Noise Figure	4.0 dB

### 5.3 OTTAWA ASR-5 TERMINAL RADAR

All operational-radar experiments discussed in this report employed the Ottawa ASR-5 terminal radar, although preliminary work had been done with other systems. This section describes only those parameters and subsystems of the Ottawa ASR-5 necessary to an understanding of the experimental results.

The ASR-5 MTI, as selected during the trials, employs a standard, double-delay, no feed-back canceller. The average PRF of 1158 Hz and PRI stagger ratio of 9:11 give rise to the velocity response shown in Figure 34, with a vestigial blind speed at 121 knots. Aircraft radial velocity components for the flights discussed here varied between zero and 125 knots. Typical radial flights were carried out with ground speeds of about 100 knots and for these, a signal-to-noise ratio loss of 5 dB would be expected.

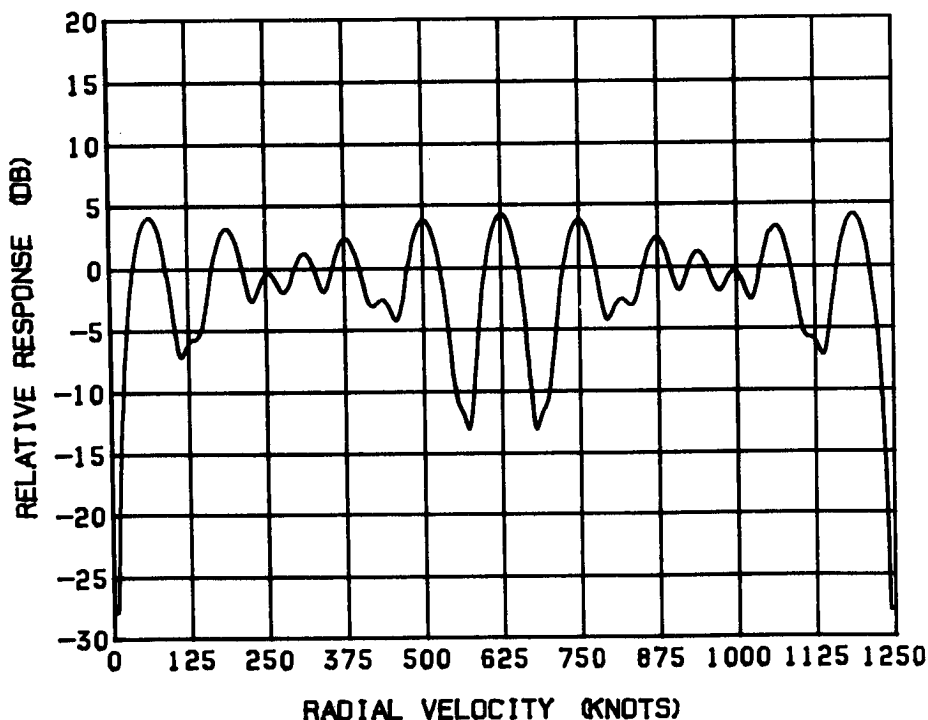


Figure 34. ASR-5 MTI Velocity Response

Figure 35 shows the probability of detecting 2, 5 and 10 m<sup>2</sup> Swerling I targets with the CRC recording equipment and ASR-5 radar employed in the Ottawa tests. In plotting Figure 35, the methods of Blake<sup>2</sup> and Fehlner<sup>10</sup> were utilized\*, with a target altitude of 2600 feet, probability of false alarm of 10<sup>-8</sup>, an assumed antenna temperature of 120°K, and an antenna beam-shape as discussed in Ref. 7 (cosecant-squared above the beam peak, and parabolic below). Total system losses of 27.7 dB have been assumed, made up as follows:

- a) MTI velocity response loss - 5 dB;
- b) recorder collapsing loss  
(Section 5.1.1) - 6 dB;
- c) antenna beamshape loss<sup>2</sup> - 1.6 dB;
- d) Bandwidth correction factor<sup>2</sup> - 1.1 dB;
- e) receiver microwave hardware  
loss - 3.9 dB;
- f) Transmitter microwave hardware  
loss - 2.5 dB; and

\* The computer program used to plot Figure 35 was written by A.U. Tenne-Sens of the Communications Research Centre, and is described by him in an unpublished Technical Memorandum.

- g) Miscellaneous (includes provision for "system degradation" in the field<sup>2</sup>, atmospheric absorption, etc). - 7.6 dB.

The above loss totals are consistent (within 2 dB) with those used in the manufacturer's published range calculations for similar equipment, if account is taken of the longer-than-standard waveguide run used in the Canadian Ministry of Transport installations. It should be noted that losses (a) and (b) introduce a potential 11 dB difference between Figure 35 and standard coverage diagrams for the ASR-5; therefore, Figure 35 relates to the present measurement program only, and should not be used as an indication of ASR-5 range performance in general.

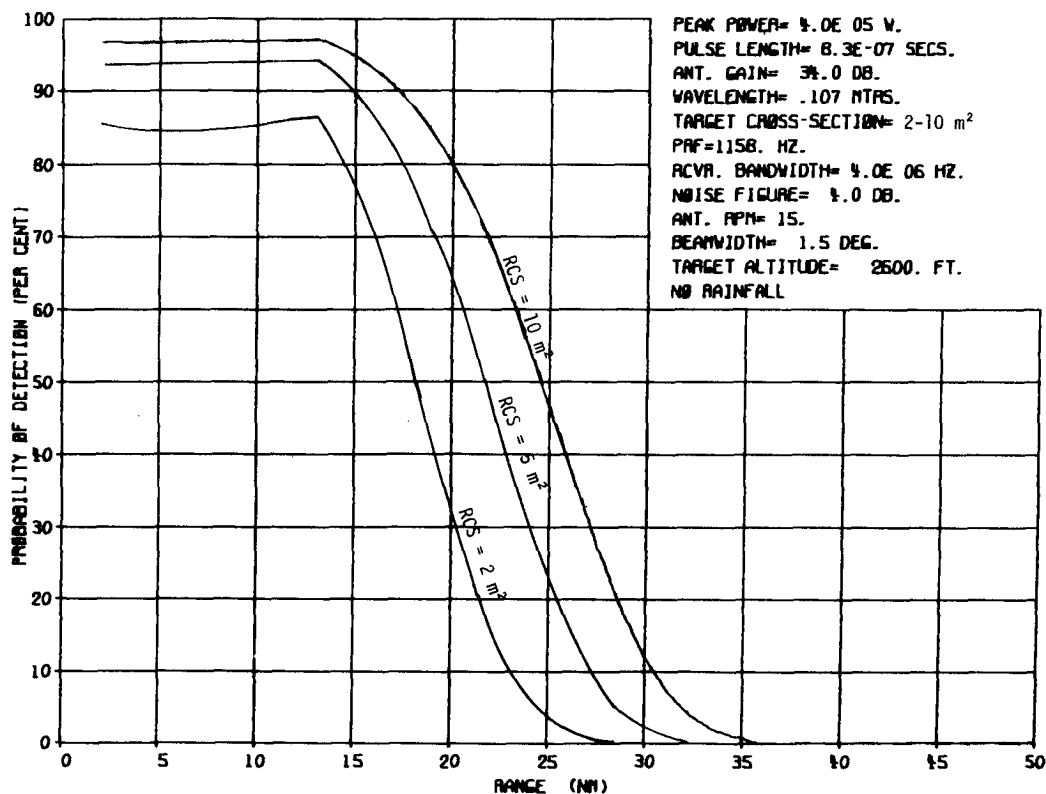


Figure 35. Probability of detecting 2, 5 and 10 m<sup>2</sup> Swerling I fluctuating targets at 3000' ASL using the Ottawa ASR-5 and CRC recorder (100 knot target radial velocity).

A video sweep integrator, as shown in Figure 36, is employed in the ASR-5 to improve detectability, particularly of the MTI output. The effect of the integrator is to introduce correlation between adjacent hits on a target. Used with the preceding limiter, the overall subsystem has the following major effects:

- a) destruction of the conventionally-assumed linear relationship between target cross section and video amplitude (targets above the noise level will all integrate up to about the same video voltage);
- b) the range-gated signal history of a target will show an envelope dominated by the integrator characteristic (a rising and falling exponential), rather than a replica of the antenna horizontal polar diagram; and
- c) pulse-to-pulse fluctuations due to MTI blind-phase effects will be largely eliminated.

Because of the first of the above effects, plans to compute the "apparent radar cross section" of the test aircraft by inversion of the radar range calculation were abandoned in favor of measuring smoothed probabilities of detection by employing a software "plot extractor", a procedure described in the next section.

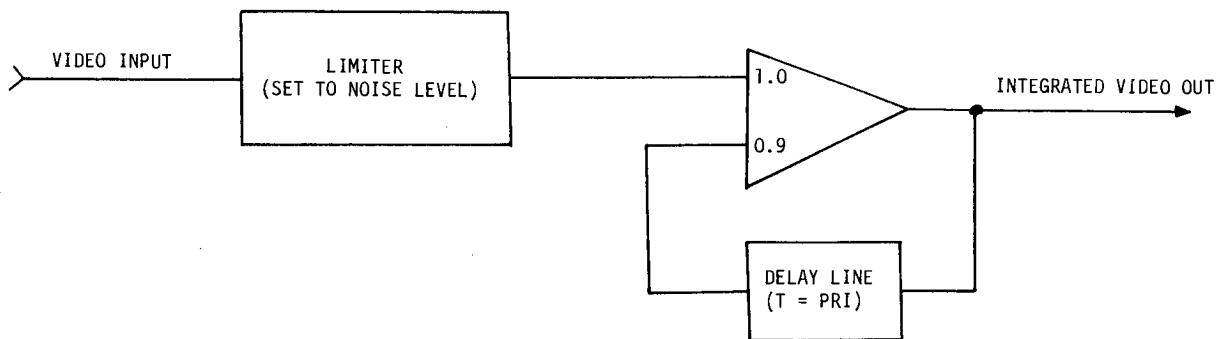


Figure 36. ASR-5 Video Integrator

## 6. OPERATIONAL RADAR EXPERIMENTAL RESULTS

This section describes experiments performed using the Ottawa ASR-5 terminal radar, and analyzes results of these experiments.

The ASR-5 at Ottawa is an operational ATC Radar, and this did not permit adjustment during a given trial. To ensure uniformity of performance, an MOT technician was in attendance during each test, and assurance was given that the channel in use was operating normally. In addition, the following tests were performed at the close of each day's activity:

- a) Measurement of bipolar video rms noise level and pre-MTI limit level (typically, the ratio of these two was 30-35 dB);
- b) Measurement of system MDS, by viewing an injected pulsed signal displayed on an A-scan display, and measurement of the RF input level required to produce limiting ahead of the MTI; and

c) Measurement of the Sensitivity Time Control characteristic in use at the time.

Figure 37 shows the tracks selected to allow observation of ASR-5 performance. The entire pattern was flown twice for each test aircraft (viz. Cherokee 140, Cessna 172, Cessna 177).

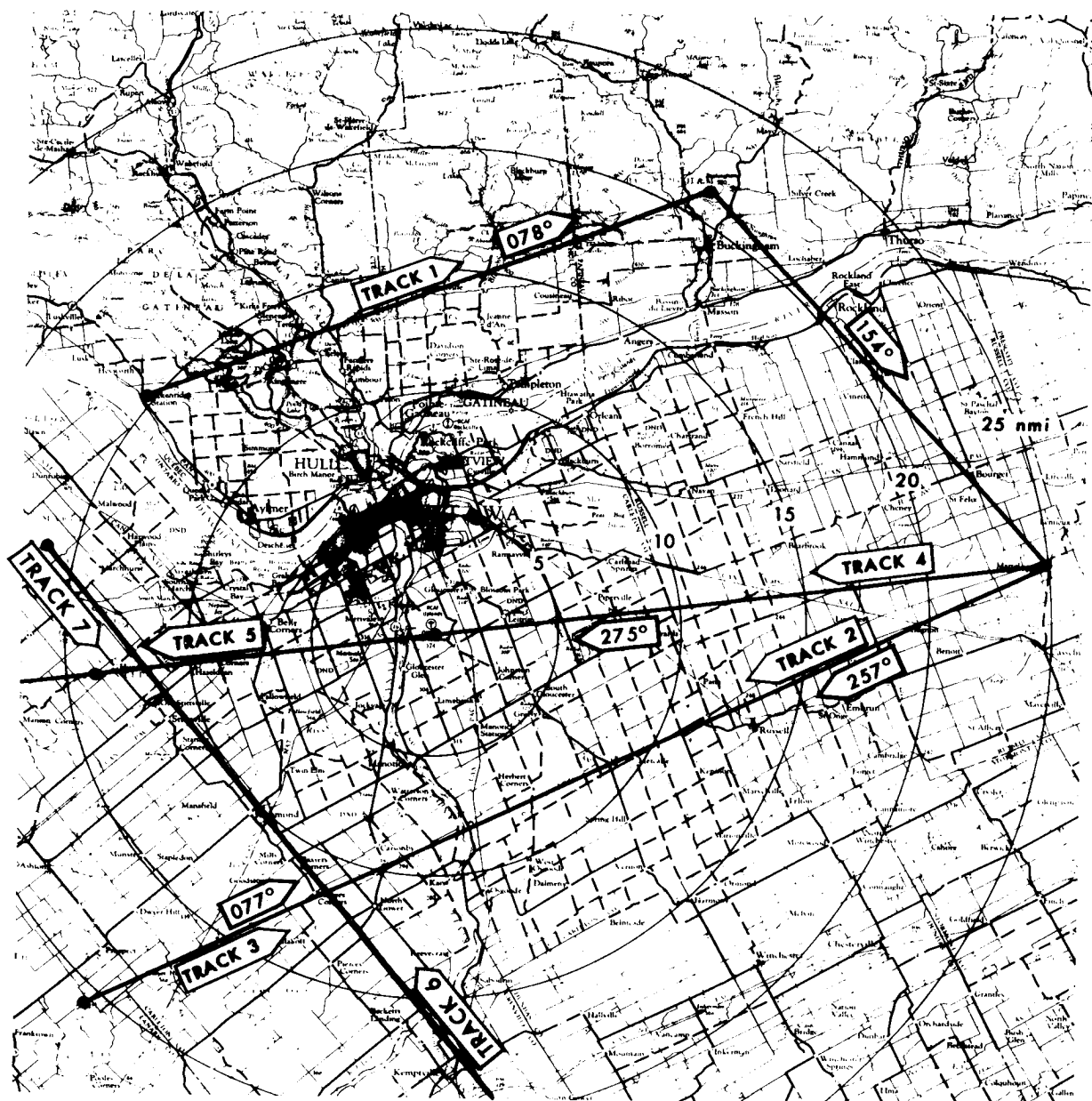


Figure 37. Experimental Tracks Flown Against Ottawa ASR-5 Radar

Track 1, which runs from the Ottawa River west of Aylmer, to just north of Buckingham, was chosen to position aircraft over the strongest ground clutter in the area. Unfortunately, this track proved difficult to follow with precision in the air, and actual ground tracks tended to deviate north of the ideal by several miles, enough to place the aircraft over clutter voids beyond the Gaineau escarpment. For this reason, only general conclusions regarding the effects of ground clutter can be drawn from the Track-1 flights.

Tracks 2 and 3, from the Casselman non-directional beacon, over the Uplands beacon, to just southwest of Richmond, were selected to avoid all ground clutter of any consequence. This routing, which shows detectability of the aircraft for a variety of aspects from  $20^\circ$  off the nose and tail, through the important  $90^\circ$  wing aspect, was flown both eastbound (Track 3) and westbound (Track 2) in every flight sequence.

Tracks 4 and 5, from Casselman non-directional beacon, over the radar, to just south of Carp, were selected to show radar performance against nose and tail aspects respectively. Again, the tracks are largely free of ground clutter.

Tracks 6 and 7, from Kemptville to the Ottawa River northwest of the Airport, were selected to be directly downwind and upwind on the day of their use. These tracks were used in the tangential fading experiments described in Section 6.5.

Results observed with each of the three aircraft types were similar, as would be expected from the measured data presented in Section 4. For this reason, the results of only one flight, that carried out on 2 May 1974 using a Cessna 177 Cardinal, will be presented in full.

## 6.1 GENERAL RESULTS

Figure 38 shows the STC characteristic set on channel B of the ASR-5 during the 2 May flight test. For ranges of 7-10 nmi, the relationship employed is a good deal more severe than  $1/R^4$ ; whereas, for ranges below 6 nmi, the opposite is true. All STC action is essentially complete by 15 nmi. Figure 38 is typical of the STC laws encountered throughout the trials, with the greatest variation from day to day occurring at the short ranges (i.e., less than 6 nmi). After the flight, MTI MDS was measured as -109 dBm, and MTI dynamic range was 35 dB. Both figures may be regarded as typical for this equipment.

Figure 39 shows a record of the position of detections during the flight sequence. The displacement of tracks 4 and 5 from the ideal (they were intended to pass over the radar) results from a minor navigation error. Isolated points, obviously separated in azimuth from the desired aircraft tracks, are due to other flights passing through the recording window.

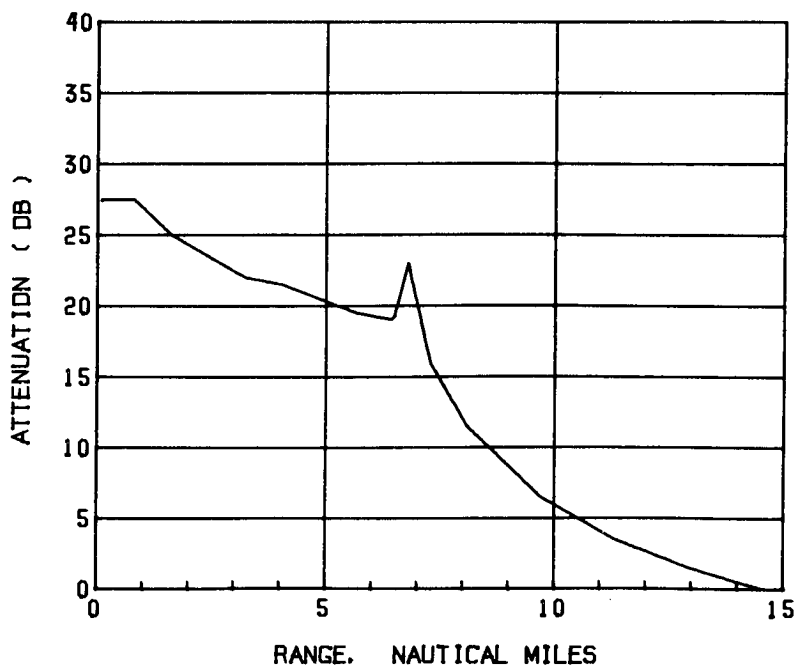


Figure 38. Measured STC Characteristic, ASR-5, 2 May 1974.

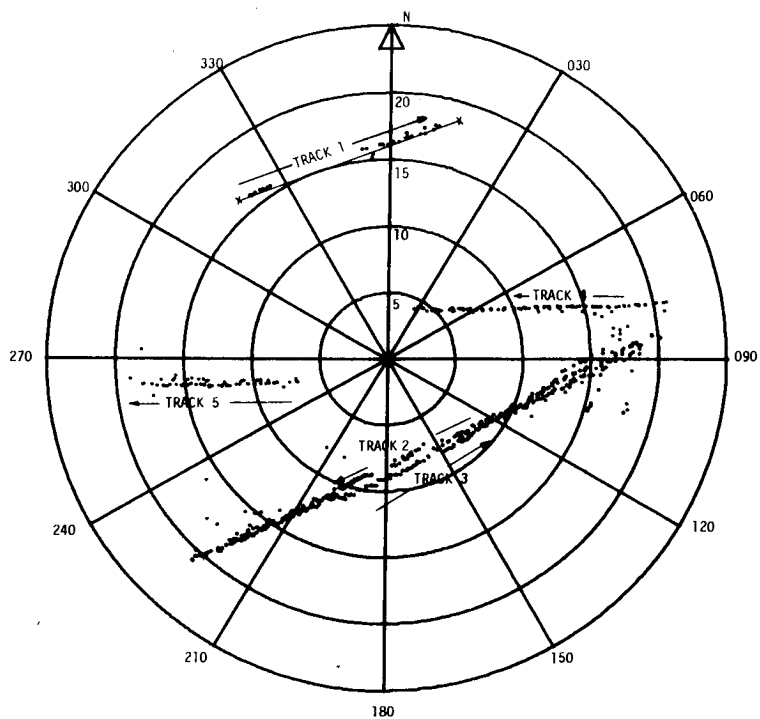


Figure 39. Radar Detections of Cessna 177 – 2 May 1974 (Scale 1:500,000).

## 6.2 TRACKS 4 AND 5 - NOSE AND TAIL-ASPECT FLIGHTS

Figure 40 shows the measured probability of detection ( $P_d$ ) of the Cessna 177 during the inbound flight at 2600 feet. At a radar range of 18 nmi, probability of detection is about 80%, consistent with a target cross section of just over  $5 \text{ m}^2$  (as may be extrapolated from Figure 35).  $P_d$  increases as the aircraft approaches, until the combination of STC and antenna beamshape cause a fall in  $P_d$  between 14 and 18 nmi. A distinct minimum in  $P_d$  is seen at 7 nmi, consistent with the STC law presented in Figure 38.

Figure 41 shows the measured  $P_d$  for the Cessna 177 during an outbound flight at 2600 feet. Again, detection probability is decreased at short ranges. Farther out, at a radar range of 17 nmi,  $P_d$  has fallen to 60%, consistent with a target cross section of about  $2 \text{ m}^2$  (see Figure 35).

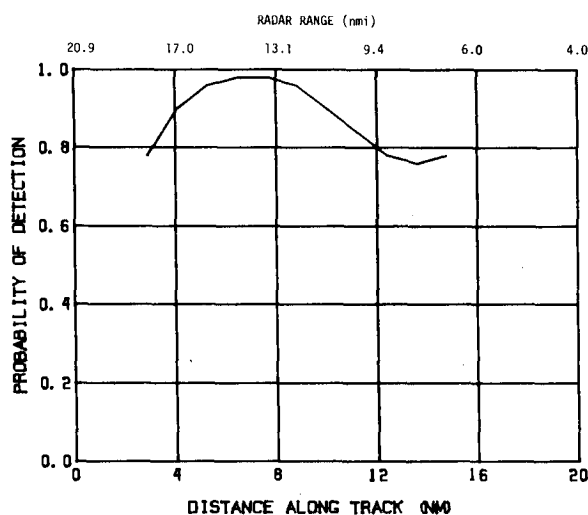


Figure 40. Cessna 177, Track 4, Inbound

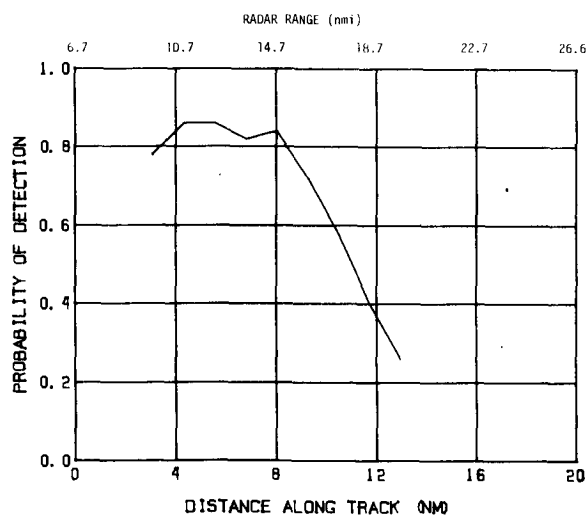


Figure 41. Cessna 177, Track 5, Outbound

The values of RCS estimated in the preceding two paragraphs from the maximum-range data show remarkably close agreement with the overall mean nose and tail radar cross sections,  $5.4 \text{ m}^2$  and  $1.3 \text{ m}^2$  respectively, measured at CRC and tabulated in Table 4-1. Equally good agreement was observed between maximum-range data and measured nose and tail-aspect radar cross sections for the Cessna 172 and Cherokee 140. While absolute values of maximum radar range are critically dependent upon the assumed system loss factor, the consistency of relative maximum ranges for different aspects is noteworthy.

## 6.3 TRACKS 2 AND 3 - TANGENTIAL FLIGHTS

Figures 42 and 43 show the measured probabilities of detection for the Westbound and Eastbound tangential flights respectively. Less difference is apparent between "nose" and "tail" maximum ranges than before, because the lateral displacement of the track does not permit direct nose and tail views of the aircraft. Again, this is in agreement with the data measured at CRC and presented in Section 4.

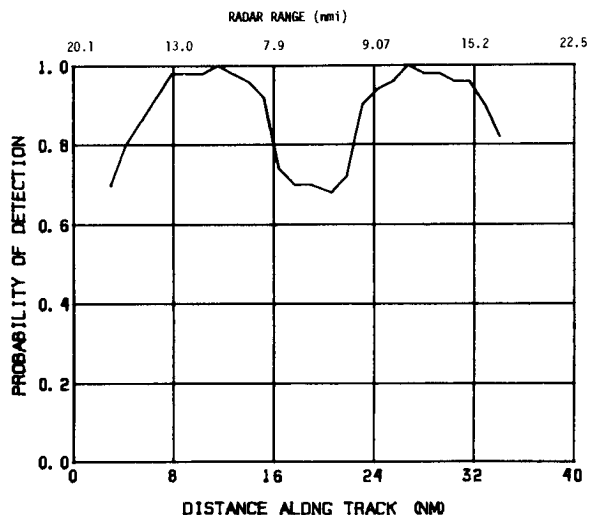


Figure 42. Cessna 177, Track 2, Westbound

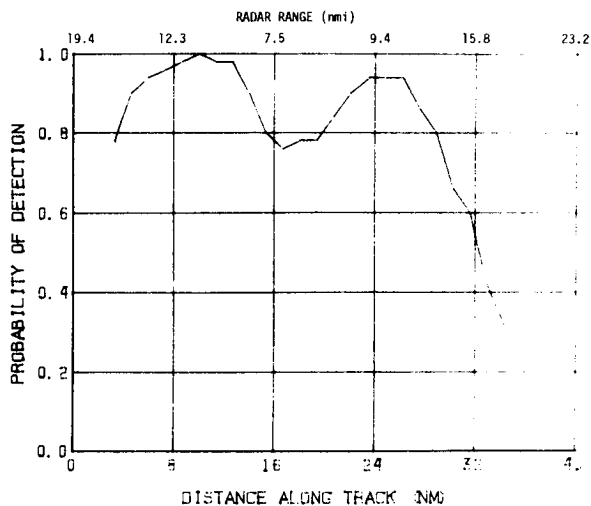


Figure 43. Cessna 177, Track 3, Eastbound

The most striking feature in both Figures 42 and 43 is the readily-apparent tangential fade. The depth of the fade implies the loss of 15 and 12 out of 50 scans respectively. The width of the fade is exaggerated by the smearing effect of calculating detection probability over 50 scans. The number of lost scans suggests a fade width of about one minute, or 1.7 nmi at a ground speed of 100 knots; although, in practice, the fade will not be rigidly defined, and will include some detections. This subject will be considered again in Section 6.5 when the effect of circular polarization is treated.

#### 6.4 TRACK 1 - FLIGHT OVER GROUND CLUTTER

Figure 44 shows the measured probability of detection for the Cessna 177 over the area of ground clutter north of Ottawa. The clutter strength along track 1 is mostly between 20 dB and 30 dB above the MDS, with clutter points in excess of 30 dB widely scattered. This level of clutter should be within the cancellation capability of the MTI, based on simple linear theory; and, therefore, little degradation should result.

Lack of range precision in the present recorder, together with lack of track accuracy on this leg (and time limitations generally), mitigate against detailed consideration of ground-clutter effects at this time. However, it can be stated that even moderate clutter levels did clearly result in a marked decrease in detection performance at a given range (compared to clutter-free tracks) for the three aircraft types studied, and that a visual screening of raw data suggests that small signal suppression, rather than MTI improvement factor degradation as a result of limiting, was the dominant cause, although both effects were observed to take place.

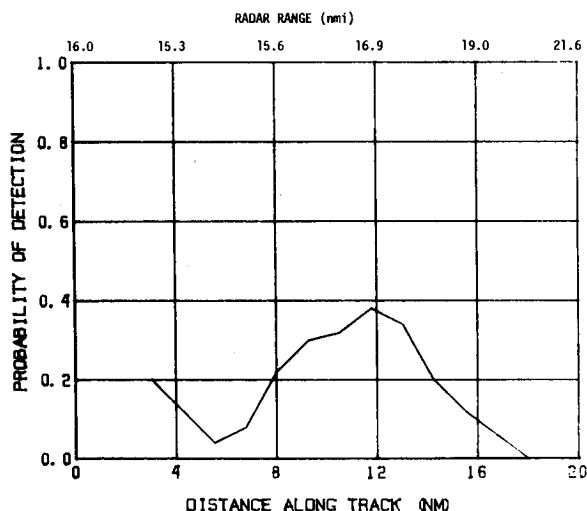


Figure 44. Cessna 177, Track 1 Over Ground Clutter

## 6.5 EFFECT OF CIRCULAR POLARIZATION ON TANGENTIAL FADES

The increase in aircraft RCS at beam aspects was discussed in Sections 2.2.1 and 4.1.1. For tangential flights, this increased cross section, occurring for aspects where radial velocity is near zero, should counteract the effect of the MTI tangential fade, and narrow the region in which radar "misses" are encountered. RAT SCAT experimenters found that the beam-aspect RCS increase was not apparent when using circular polarization (see Section 2.2.1). Hence, tangential fades should be more severe when using circular polarization than when using linear polarization, at least under the following ideal conditions:

- a) accurately flown tangential track, with small heading errors (i.e., not more than 5 or 10 degrees);
- b) near-zero bank angle (i.e., excludes fades encountered during arc flying); and
- c) crab angle due to wind drift less than about 10 degrees.

A mathematical model was evaluated, and four test tracks flown (two using circular polarization; two using linear polarization) to test the practical effect of circular polarization tangential fades. A Cessna 172 was employed in this sequence of flights.

Figure 45 shows a simplified model for the dependence of Cessna 172 RCS on aspect, for linear and circular polarizations. The shapes and magnitudes are consistent with measured median values. Circular polarization is assumed to result simply in the disappearance of the beam-aspect peak in RCS, and a drop of 5-6 dB in "background" RCS.

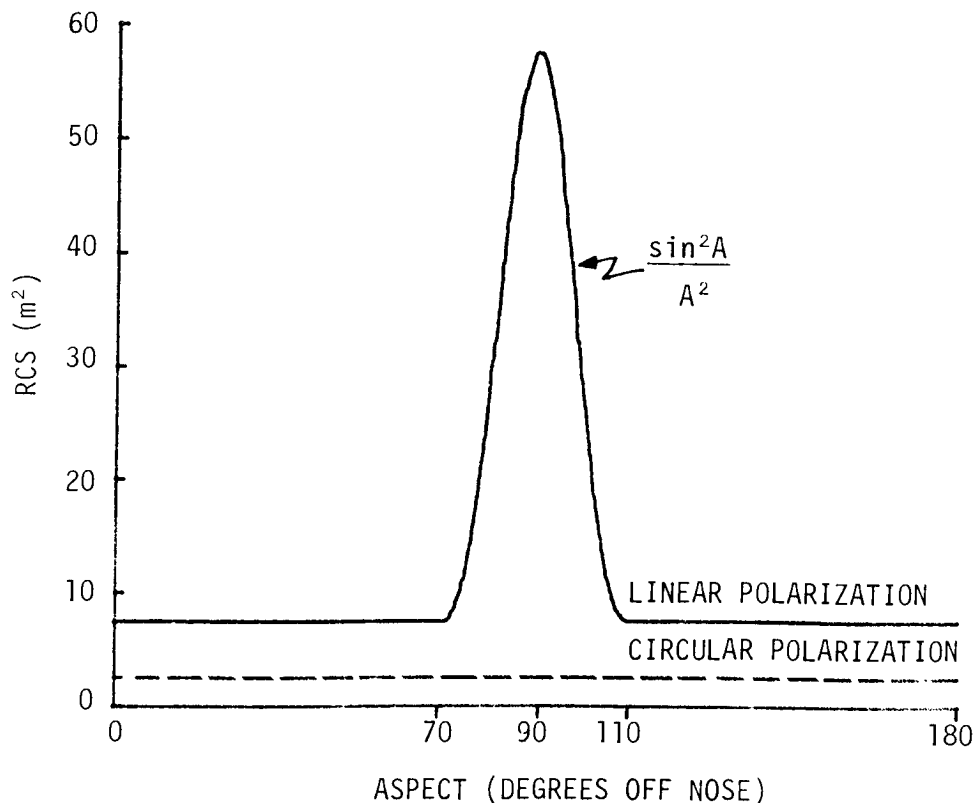


Figure 45. Simplified Model for Light-Aircraft RCS.

Figure 46 shows the computed MTI amplitude, as a function of position, for a tangentially-flying target. This computation assumes the MTI response of the ASR-5 radar (i.e., double-delay canceller with no MTI feedback, S-band, PRF of 1158 Hz). The "No. of Scans" notation along the top of the graph relates to a tangential flight by a 100 knot aircraft with a distance of closest approach of 11 nmi, these being the parameters of the test flights reported in this section. Appendix C shows the signal margin above MDS for a 7 m<sup>2</sup> target at 11 nmi to be 19.6 dB for the Ottawa ASR-5 radar. Moving to -19.6 dB in Figure 46, one would expect the given flight to result in a fade width (using linear polarization) of 14 scans, 1.6 nmi, or 56 seconds. The use of circular polarization, according to the model, will aggravate this situation, doubling the fade to 28 scans, 3.2 nmi, or 112 seconds.

A Cessna 172 was flown along tracks 6 and 7, selected to minimize wind drift and ground clutter: two reciprocal tracks were flown for circular and two for linear polarization. Figures 47 and 48 show the recorded probability of detecting the Cessna 172 along the northbound and southbound tangential tracks respectively, using linear polarization. It is interesting to note that Figures 47 and 48 are almost exact mirror images of each other, showing the repeatability of the averaged probability of detection plots. One slight difference, the lower  $P_d$  at the right-hand extreme of Figure 47 compared to the left-hand extreme of Figure 48, is likely due to the former being a

tail-aspect view, while the latter is nose-aspect (see relative RCS values given in Section 4). Figures 49 and 50 show the identical routes, tracked using circular polarization. The increased depth and width of the tangential fade, compared to that encountered using linear polarization, is clear. Table 6.2 summarizes the number of missed scans in the fade for the four tracks and for the theoretical model. Measured results are consistent with those calculated from the model. Although the precise fade width calculated from the model is dependent upon the selected signal margin above MDS, the relative increase in fade width engendered by the use of circular polarization, given an assumed linear-polarization fade width, is far less so.

TABLE 6.2  
*Width of Tangential Fade (Number of Missed Scans)*

	Linear Polarization	Circular Polarization
Northbound (Figures 47, 49)	16	30
Southbound (Figures 48, 50)	18	28
Model (Figure 46)	14	28

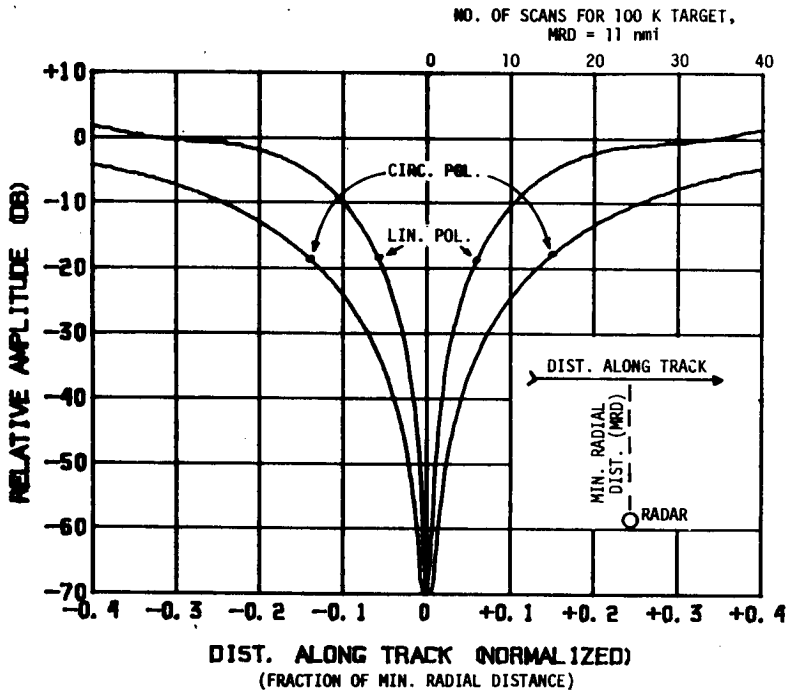


Figure 46. Computed ASR-5 MTI Amplitude For Tangential Tracks

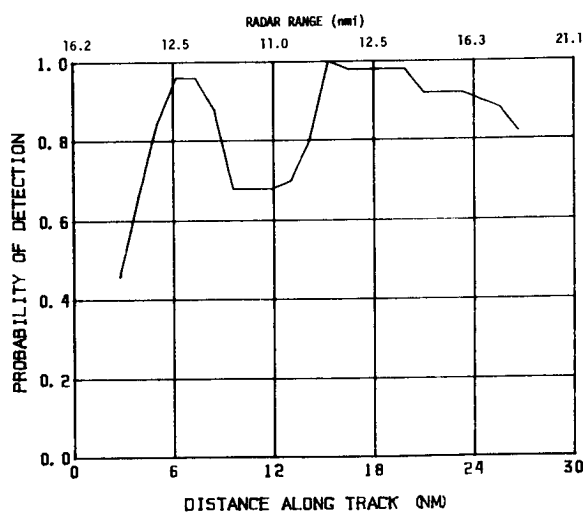


Figure 47. Cessna 172, Tangential Track  
 - Linear Polarization  
 - Northbound

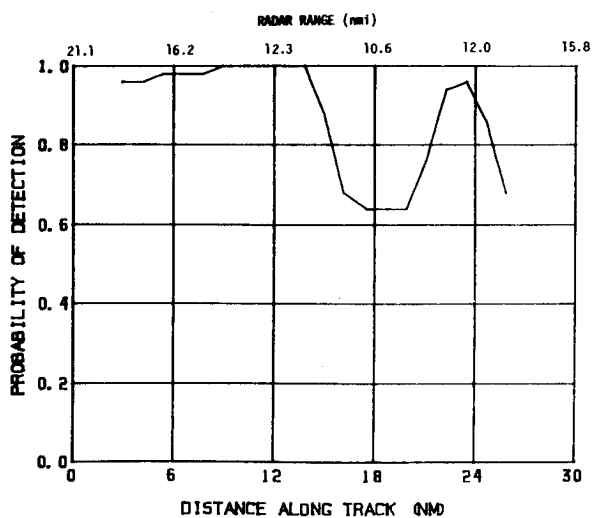


Figure 48. Cessna 172, Tangential Track  
 - Linear Polarization  
 - Southbound

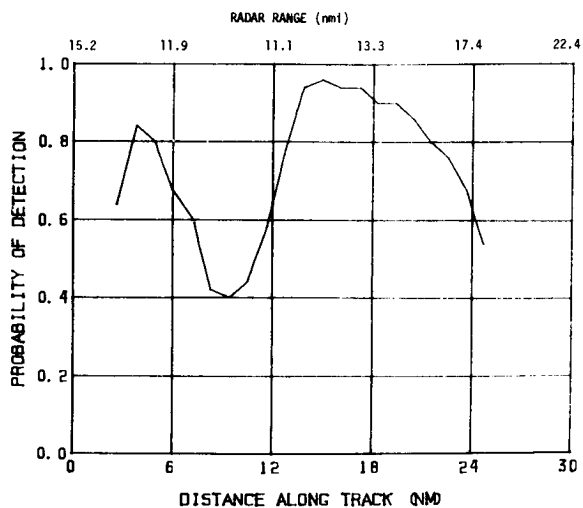


Figure 49. Cessna 172, Tangential Track  
 - Circular Polarization  
 - Northbound

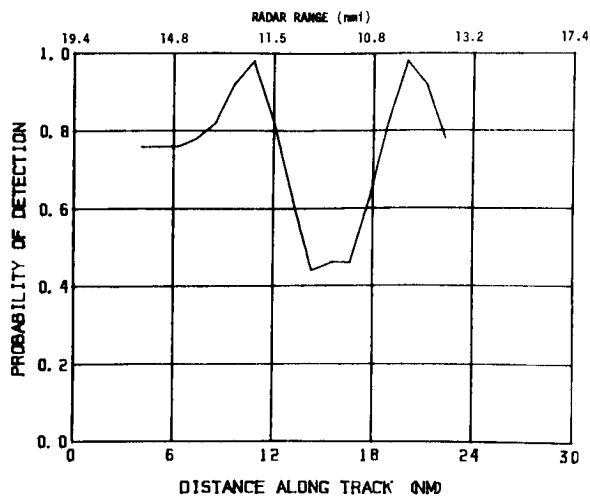


Figure 50. Cessna 172, Tangential Track  
 - Circular Polarization  
 - Southbound

In addition to affecting the tangential fade, circular polarization results in a loss of range performance (e.g., 0.62 versus 0.88 probability of detection at 17.4 nmi range from Figures 47 and 49), approximately equivalent to a 6 dB loss on a Swerling I target, in agreement with RAT SCAT data. A lack of symmetry in the range performance is also apparent for both circular and linear polarizations. This resulted from repeatedly observed poor detection performance to the south of the radar at 12-16 nmi. No attempt was made to determine the cause of this weakness which, incidentally, occurs with the aircraft viewed at both nose and tail aspects in the figures presented.

## 7. CONCLUSION

The time and frequency domain characteristics of the radar echo from light aircraft have been studied, using data derived from a static range, a coherent laboratory radar, and an operational air traffic control radar. The results of this study are summarized below.

### 7.1 SUMMARY OF PRINCIPAL CONCLUSIONS

a) With linear polarization, the median radar cross sections of Cessna 177, 172, 150 and Cherokee 140 aircraft generally lie between 0 and 10 dBsm for all aspects except the beam aspect (Sections 2.2.1, 4.1.1, and 4.1.2.2).

b) With linear polarization, the median RCS of the above aircraft at beam aspects is about 20 dBsm over a 20° wide interval for 0° of bank (Sections 2.2.1 and 4.1.1).

c) Circular polarization results in a 5 or 6 dB loss in median echo amplitude, except at beam aspect where the loss is about 15 dB (Section 2.2).

d) When an aircraft is in a turn, stronger signals are received from the upper surface than the lower surface (i.e., when the radar is abeam of the passing aircraft, turns away from the radar will momentarily produce worse fades than will turns toward the radar) (Section 2.2).

e) Median RCS is substantially independent of frequency from L through C band (Section 2.2.3).

f) Within S band, only the fine detail of RCS versus aspect is frequency dependent (Section 2.2.3).

g) Median RCS is not strongly affected by pitch changes of up to  $\pm 10^\circ$  (Section 2.2.3).

h) Vertical and horizontal polarization yields near-identical RCS for all aspects of the aircraft studied (Section 2.2.3).

i) The RCS of the fabric-covered Super Cub is similar to that of all-metal aircraft of comparable size, except that strong peaks are not observed at the beam aspect (Section 2.2.3).

j) For all aircraft studied, at all aspects except beam aspect, the RCS probability density function may be taken to be either exponential or the weighted sum of two exponential functions with different mean values. The use of an exponential density is justified for generalized performance calculations only (Section 4.1.2.2). The assumption made in the Swerling I model, that the RCS is constant within a scan, does not hold in practice (Section 4.2.4).

k) Mean values of the various RCS density functions for various aspects of the aircraft studied are summarized in Table 4.1. In general, large RCS seems to depend more on rectangular form and a lack of streamlining than on physical size. Nose aspects always yielded higher RCS values than tail aspects (Section 4.1.2.2).

l) The short-term mean RCS of light aircraft in flight fluctuates by as much as 10-20 dB over intervals as short as 1.5 seconds (Section 4.1.1).

m) Nose and tail aspect spectra show strong propeller doppler lines, but narrow frequency extent. At beam aspects, propeller line spectra cover a wide frequency range, but their amplitude is small. Hence, doppler-shifted components due to the propeller provide little improvement in MTI performance, with the possible exception of a tendency for propeller modulation to "fill-in" the blind speeds of non-staggered systems viewing aircraft at quartering aspects (Section 4.2.3).

n) Modeling and measurement suggests that the use of circular polarization will double the width of the region of tangential fading (compared to that encountered using linear polarization), although this effect may not always be apparent where crab angle is high, or where the aircraft heading is wandering (Section 6.5).

o) Ground clutter reduces ASR-5 detection performance, apparently through small-signal suppression, even where the clutter is well within the normally-assumed MTI cancellation capability of the radar (Section 6.4).

p) Non-optimum STC adjustment can seriously reduce detection performance against light aircraft at short ranges (Section 6.2).

## 7.2 RECOMMENDATIONS

The difficulty of detecting light aircraft is not due solely to their small radar cross-section, but to this factor in association with others. The most important of the other factors are the techniques used to enhance detection in clutter (e.g., MTI, limiting receivers, STC, circular polarization), and the operational practices (which are, in part, imposed by the design) of using these techniques in weather conditions, or on ranges and azimuths where they are not only unnecessary but actually disadvantageous. Improved detection performance could be realized by more elaborate signal processing, but the cost is likely to be high. Experience with air defence radar, which tends to lead ATC radar in sophistication (and expense), does not suggest that an ultimate solution to primary radar shortcomings will be obtained simply by improved radar design.

The most obvious and most effective solution to the problem of detecting light aircraft is to require that all aircraft operating within extended DND Positive Control Zones or civil Terminal Radar Service Areas be fitted with SSR Transponders, so that the positive technical features of primary and secondary radar can complement one another. The "political" practicality of this requirement is indicated by the adoption, some years ago, of a similar requirement for two-way communications equipment. Before adopting this course, it would be necessary to verify that it would not lead to over-loading of the Secondary Surveillance Radar system. The authors believe that this would not be an immediate problem in Canada.

The following recommendations relate to the design, siting, and operation of future military ATC radar systems, and are offered on the assumption that improved primary radar performance is required, whether or not the course recommended above is adopted:

a) Requirements for new ATC radars should include the demonstration of reliable detection of a specified "worst-case" target. The target should have a mean RCS of  $1\text{m}^2$ , with an exponential distribution, where detection of no one aircraft type is of dominant concern. However, the correlation properties assumed in the Swerling I target model must be viewed with suspicion, particularly when analysing radar performance at high probabilities of detection, where in-scan fluctuations of real light-aircraft targets will make that model a pessimistic predictor of detection.

b) All ATC terminal radars should be capable of employing linear as well as circular polarization. Operators should be made aware of the degradation in performance (with respect to detection range and tangential fading) caused by the unnecessary use of CP in dry weather.

c) Sweep integration and/or quadrature detection should be incorporated in ATC terminal radars with MTI, to decrease the incidence of blind-phase effects, both pulse-to-pulse and scan-to-scan.

d) Adaptive clutter switching should be employed to restrict the use of MTI processing to areas of high clutter.

e) The position and size of probable tangential fade areas should be estimated and taken into account in determining radar siting, particularly in cases where the radar is not located on the airport.

f) STC adjustment procedures should be chosen with care, to avoid the severe attenuations at short ranges often chosen in the interests of reducing MTI residue near the middle of the PPI.

g) Further research should be undertaken to study the application of automatic scan analysis, as used in the work reported here, to the improvement of system evaluation and routine maintenance procedures.

## 8. ACKNOWLEDGEMENT

The authors wish to acknowledge with gratitude the technical and financial support given by the Directorate of Electronics Engineering and Maintenance, National Defence Headquarters. Appreciation is also extended to the Ministry of Transport for arranging CRC access to their radars, and to the technicians and controllers at Ottawa International Airport for their assistance during the flight tests. Permission given by the Federal Aviation Administration permitting reproduction of static light-aircraft RCS data measured at RAT SCAT has contributed strongly to the conclusiveness of the dynamic measurements reported herein.

Although many CRC staff members were associated with the project from time to time, the contributions of Mr. D.M. Selwyn who designed the digital recording equipment and organized the flight tests, and Dr. A.W.R. Gilchrist who edited and significantly influenced the content of the final report, are worthy of particular mention.

The overall project was carried out under the auspices of the Department of National Defence, Canada.

## 9. REFERENCES

1. Patriarche, M.V., *An Evaluation of Some Features of An Air Traffic Control Radar System in a Mountainous Environment*, CRC Tech. Note No. 635, April 1972.
2. Skolnik, M.I., (ed), *Radar Handbook*, McGraw Hill, New York, 1970. (Chapter 2).
3. Edrington, T.S., *The Amplitude Statistics of Aircraft Radar Echoes*, IEEE Transactions on Military Electronics, January 1965.
4. Gardner, R.E., *Doppler Spectral Characteristics of Aircraft Radar Targets at S Band*, Naval Research Laboratory Report No. 5656, August 1961.
5. Bahret, W.F., *Dynamic Full Scale Measurement of RCS*, NATO AGARD LS-59, October 1973.
6. Federal Aviation Administration Report No. FAA-RD-74-99, *Static Radar Cross Section of Light Aircraft*, Volumes I, II and III, December 1973.
7. Patriarche, M.V., *A Theoretical Study of the Effect of Rain Upon the Performance of Airport Surveillance Radars at Canadian Military Terminals*, CRC Report No. 1222, Ottawa, December 1971.
8. Pollon, G.E., *Statistical Parameters for Scattering from Randomly Oriented Arrays, Cylinders and Plates*, IEEE Transactions on Antennas and Propagation, Vol. AP-18, No. 1, January 1970, pp. 68-75.

9. Wilson, J.D., *Probability of Detection of Radar Targets*, IEEE Transactions on Aerospace and Electronic Systems, Vol. AES-8, No. 6, November 1972.
10. Fehlner, L.F., *Marcum's and Swerling's Data on Target Detection by a Pulsed Radar*, Johns Hopkins Applied Physics Laboratory Report No. TG-451, and "Supplement", Report No. TG-451A.

## A P P E N D I X   A

### Aircraft Accident Report

DEPARTMENT OF TRANSPORT  
 MINISTÈRE DES TRANSPORTS

 AIRCRAFT ACCIDENT REPORT  
 RAPPORT D'ACCIDENT D'AVIATION

 REFER TO REPORT NO  
 REF RAPPORT N°

P0801

AIRCRAFT TYPE - Type aéronef <b>Vickers Viscount 757</b>	REGISTRATION - Immatriculation <b>CF-THY</b>		
AIRCRAFT TYPE - Type aéronef <b>Ercoupe 415C</b>	REGISTRATION - Immatriculation <b>CF-SHN</b>	DATE-TIME - Date-Heure <b>1Mar70 1332 PST</b>	OPERATION - Opération <b>-</b>
PLACE - Endroit <b>8 miles SE of Vancouver International Airport, BC</b>	LATITUDE <b>49/06N</b>	LONGITUDE <b>123/03W</b>	
LOCALITY - Lieu <b>Near Vancouver, BC</b>			
WEATHER - Conditions météorologiques <b>High scattered cloud, visibility 50, temperature 42°F, wind NW at 13 mph</b>			

PILOT PILOTE	LICENCE	TOTAL HOURS - Heures totales	TOTAL HOURS, LAST 90 DAYS - Total d'heures (90 derniers jours)
		ALL TYPES - Tous types ON TYPE - Type en cause	ALL TYPES - Tous types ON TYPE - Type en cause
PILOT PILOTE	Air Transport	7376	135
		2040	135
PILOT PILOTE	LICENCE	TOTAL HOURS - Heures totales	TOTAL HOURS, LAST 90 DAYS - Total d'heures (90 derniers jours)
		ALL TYPES - Tous types ON TYPE - Type en cause	ALL TYPES - Tous types ON TYPE - Type en cause
PILOT PILOTE	Private	300	3
		200	3

## DESCRIPTION OF OCCURRENCE - Description de l'événement

Air Canada flight 106 departed from Victoria, BC at 1318 PST enroute to Vancouver International Airport. At 1326 PST the pilots cancelled their IFR flightplan but remained on the arrival frequency for radar surveillance. While nearing destination in clear weather in a VFR descent of 500 fpm and 180 kts, the pilots were informed by arrival control that there was an aircraft at 12 o'clock at one mile, moving from left to right. They looked intently but were unable to see the aircraft; radar then reported that the target had disappeared and directed a frequency change to tower. The pilots resumed their pre-landing cockpit duties and a few seconds later they felt a slight jar as the Viscount collided with a white Ercope at approximately 1500 feet asl. Witnesses to the collision saw a small white aircraft spiralling to the ground. The Viscount landed safely with minor damage to an engine nacelle.

Vancouver International Airport positive control zone extended five miles from the airport. Aircraft flying within this zone are required to maintain two-way radio contact with the control tower. A NOTAM in effect at the time of the accident requested that pilots flying VFR outside the control zone but within a 10 mile radius of the airport remain at or below 1500 feet asl, unless otherwise cleared by (Cont'd on back)

	TOTAL	FATALITIES - Pertes de vie	SERIOUS INJURIES - Blessures graves	MINOR INJURIES - Blessures légères
CREW - Équipage	4	1		
PASSENGERS	29			
OTHERS - Autres				

## ASSIGNED CAUSE(S) - Cause(s) assignée(s)

The see-and-be-seen concept, although augmented by radar, was ineffective.

The procedures to ensure safe separation of mixed traffic in the Vancouver area are obsolescent.

Vancouver tower (See Figure A-1). Radar monitoring in the area is available from a radar screen in the control tower.

The Ercoupe had taken off from nearby Delta Airpark on a solo recreation flight and was being flown outside the 5-mile positive control zone of Vancouver International Airport, but inside the 10-mile area defined by the NOTAM. The pilot had not contacted any Vancouver agency by radio and, at the moment of collision was at or near the edge of the restricted airspace (Figure A-2).

The Viscount descended VFR toward the Romeo beacon with its prescribed crossing altitude of 1300 feet asl; this would require approaching or penetrating a region where mixed local traffic is confined.

The Ercoupe was painted white and would be difficult to see against the background of predominantly white houses. The Viscount pilots were also attempting to spot a target which had a low relative movement across their line of vision.

The radar equipment currently in use has several limitations. For example it can indicate range and direction but not altitude. Small targets such as light aircraft (not equipped with transponder beacons) do not always provide reliable returns; also, small targets can be obscured by returns from larger aircraft, particularly those equipped with transponder beacons.

1. Although the visibility was excellent, and approach control had alerted the pilots of the Viscount, they did not see the Ercoupe.
2. By cancelling IFR and descending the Viscount crew were approaching airspace allocated to mixed traffic, thus placing dependence on the see-and-be-seen concept.
3. The cautions, regulations, restrictions, etc, aimed at providing safe separation at controlled airports are contained in several publications, NOTAMS, etc. There was no assurance that the pilot of the Ercoupe had received all essential information relating to aircraft operation in the Vancouver area.
4. The radar at Vancouver International Airport as at all major airports has no height finding capability. This not only seriously limits its usefulness as a collision avoidance device but downgrades the credibility of ATC collision avoidance assistance to pilots. Additionally, not all pilots are aware of the limitations of radar and some place undue reliance on it.
5. The Ercoupe, because of its size provides an unreliable radar return. This partially negated the value of the air traffic control radar.

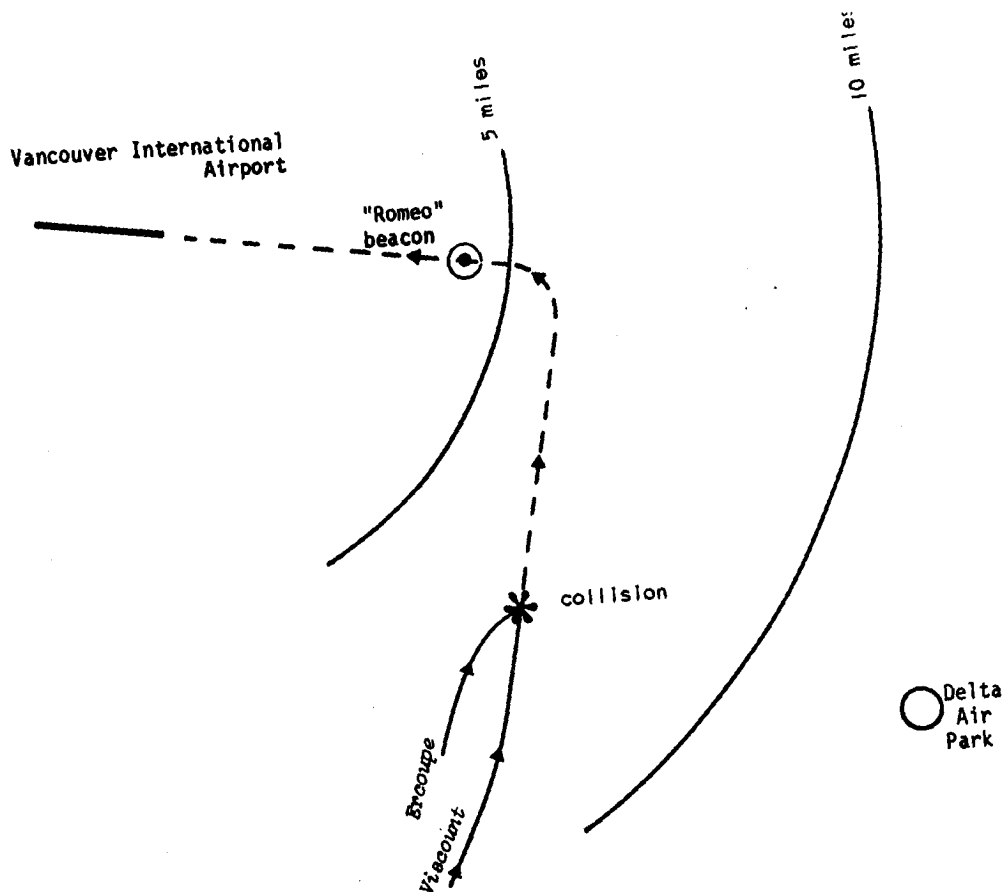


Figure A-1. Flightpaths of The Two Aircraft.

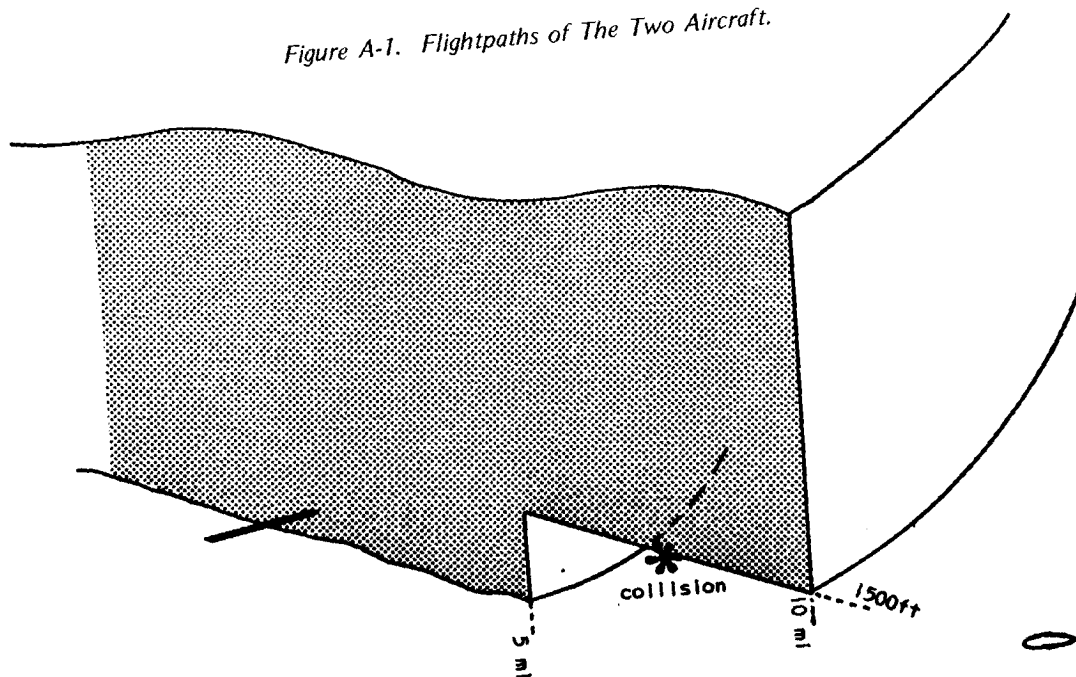


Figure A-2. Sectional View of Region of Positive Control (Shaded).

## A P P E N D I X   B

### Representative RCS Probability Density Functions for Cherokee 140, Cessna 177, and Cessna 172

Figures B-1 to B-15 are additional typical RCS probability density functions, prepared as discussed in Section 4.1.2 of the text.

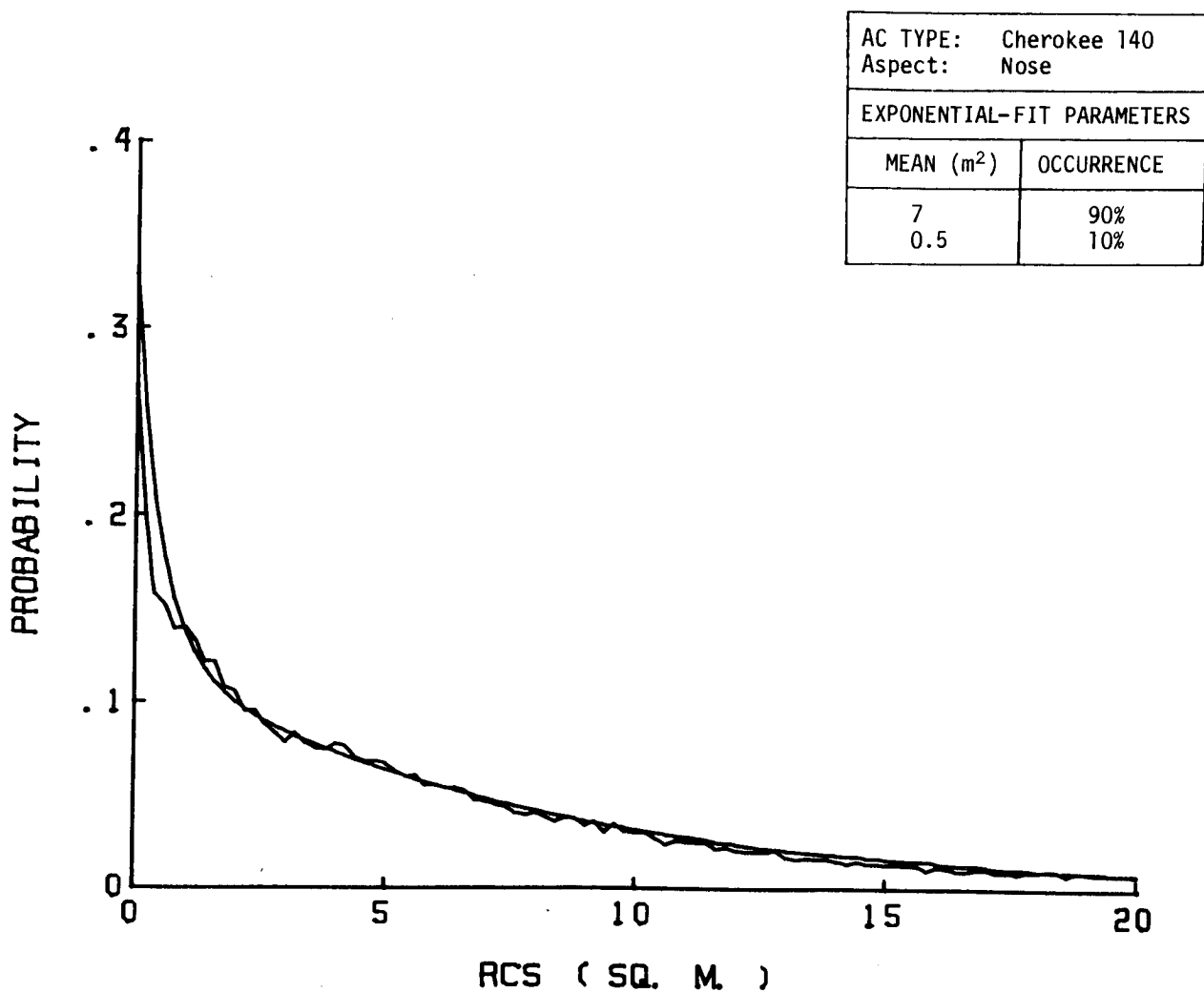


Figure B-1. RCS Probability Density Function.

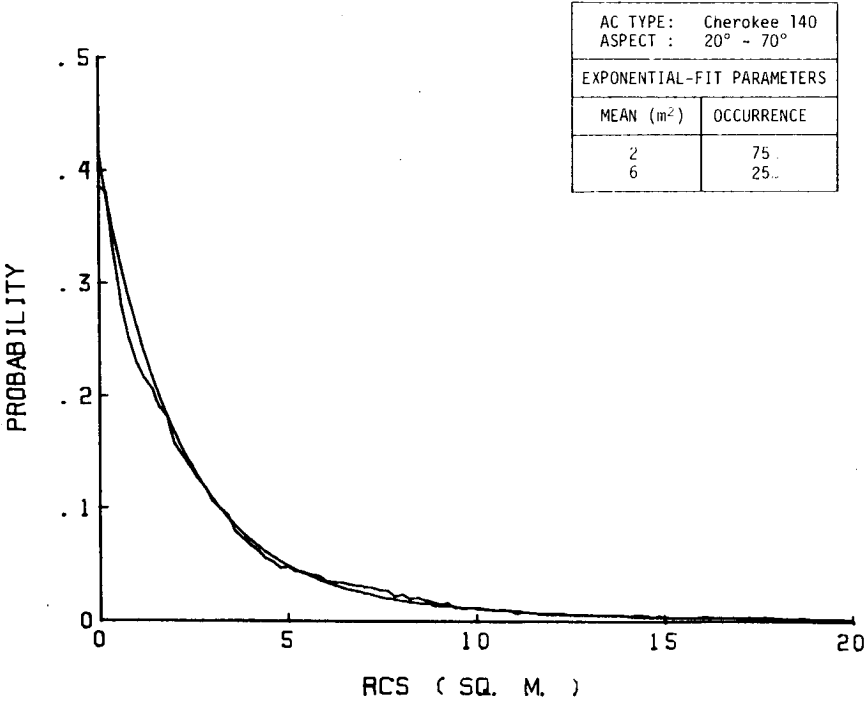


Figure B-2. RCS Probability Density Function.

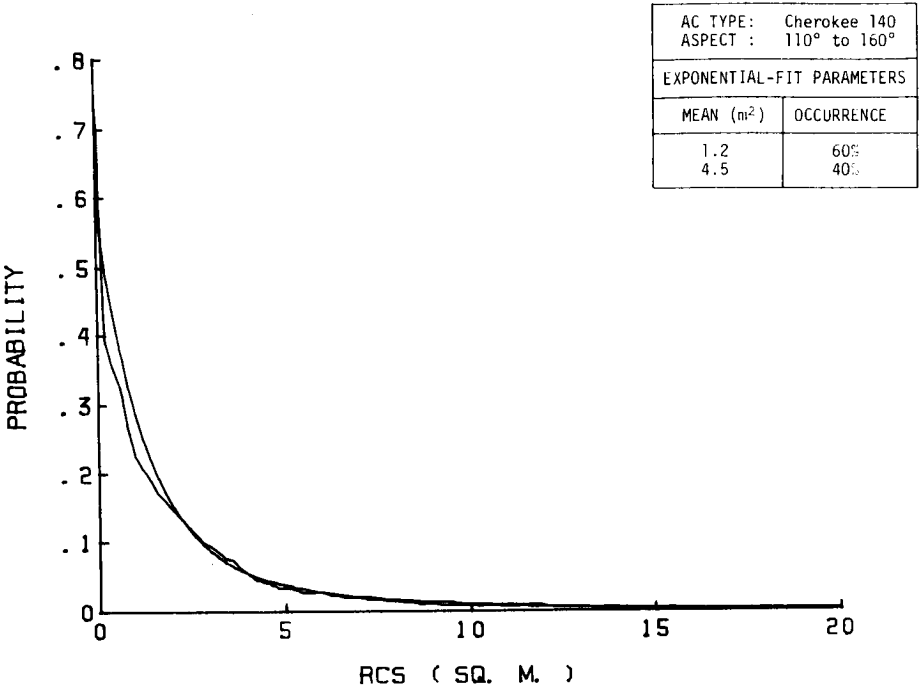


Figure B-3. RCS Probability Density Function.

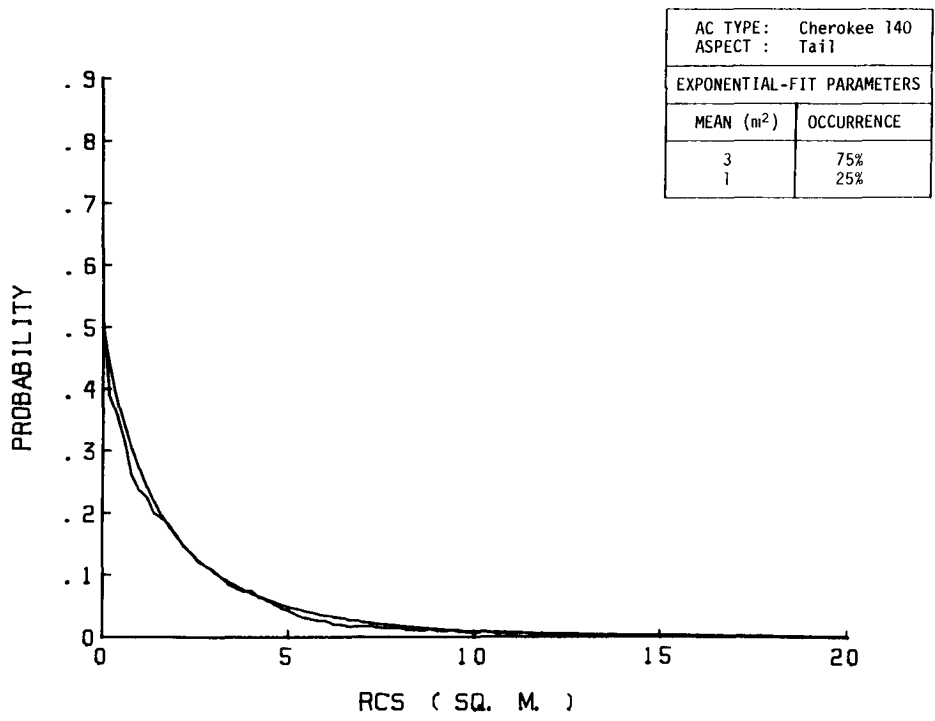


Figure B-4. RCS Probability Density Function

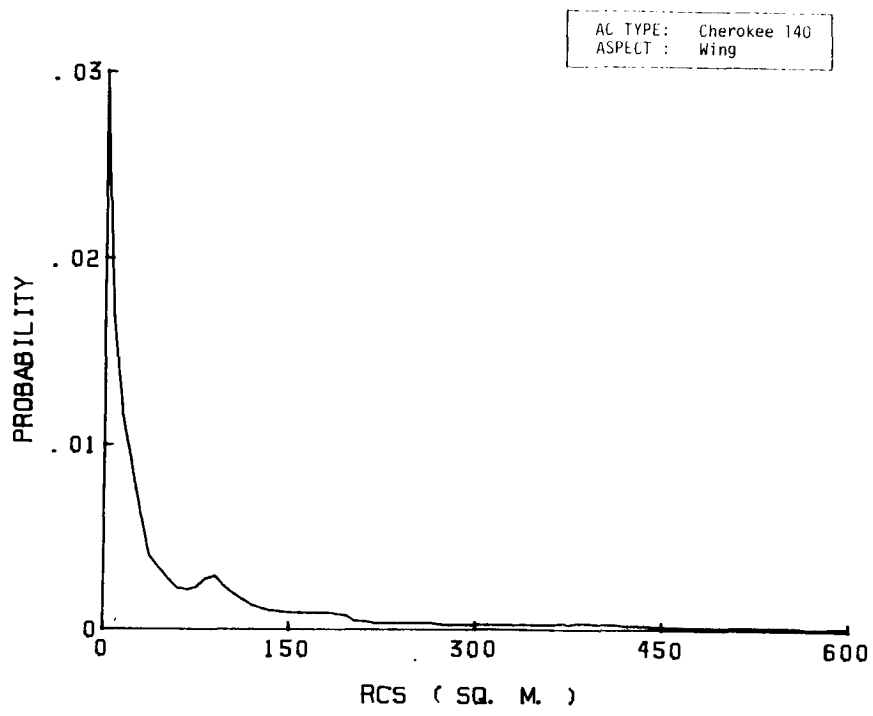


Figure B-5. RCS Probability Density Function.

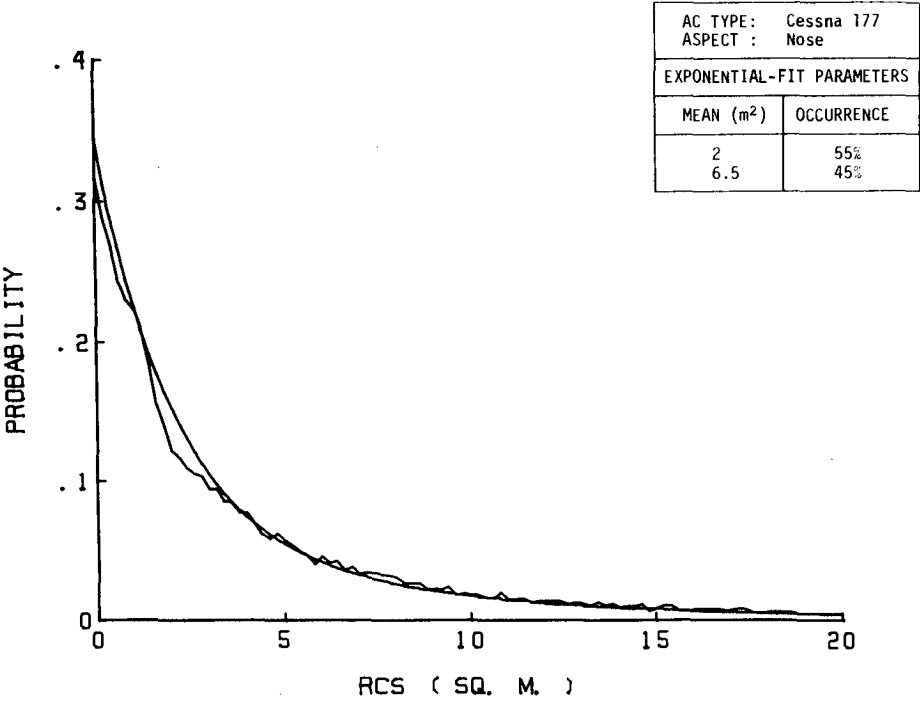


Figure B-6. RCS Probability Density Function.

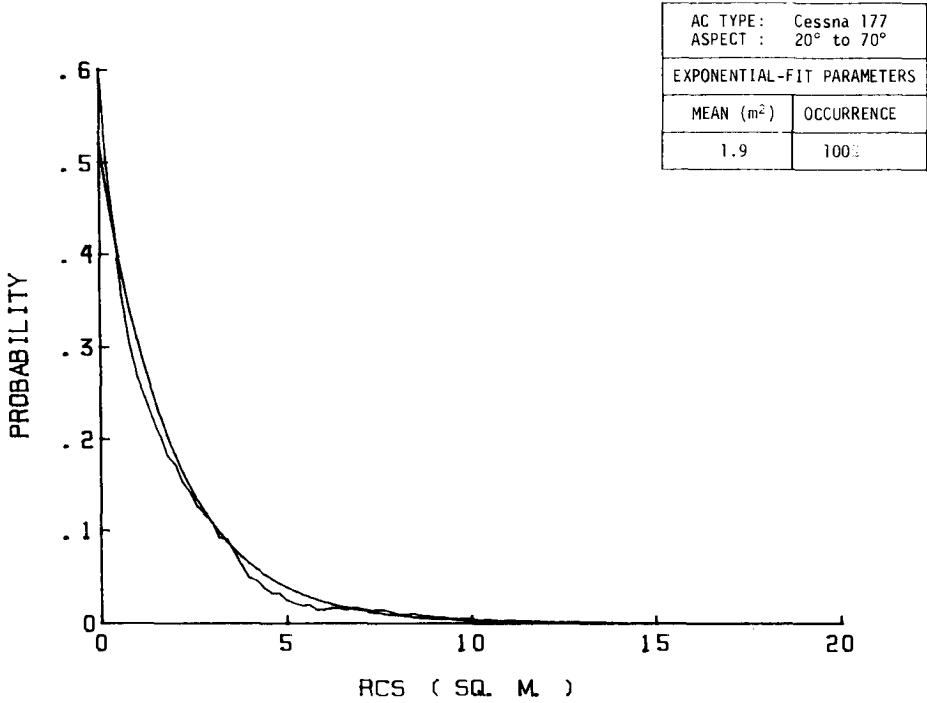


Figure B-7. RCS Probability Density Function.

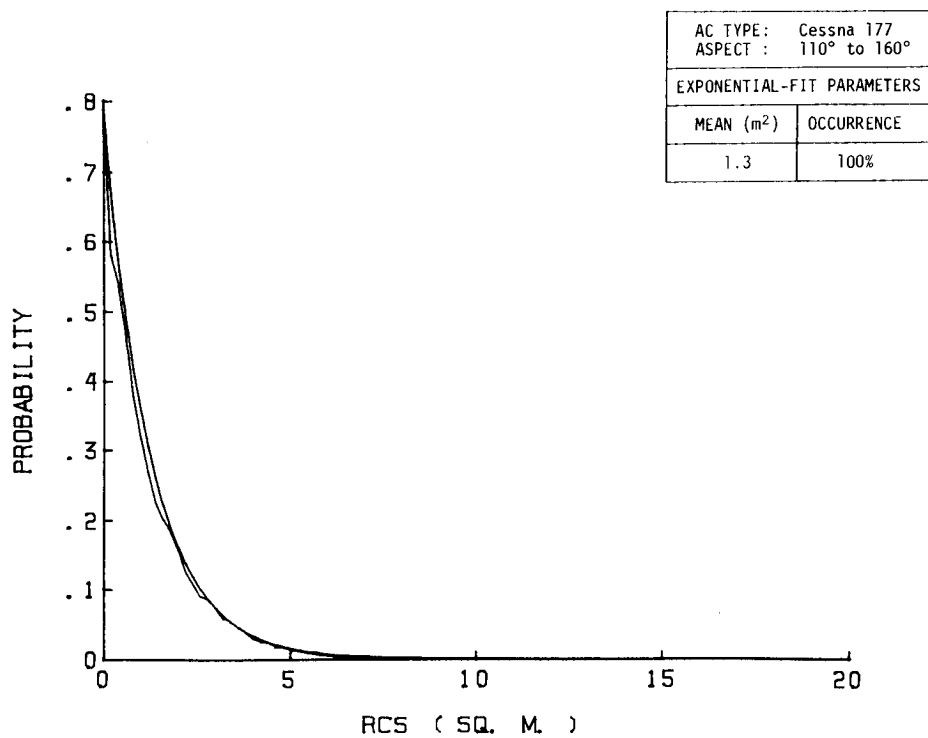


Figure B-8. RCS Probability Density Function.

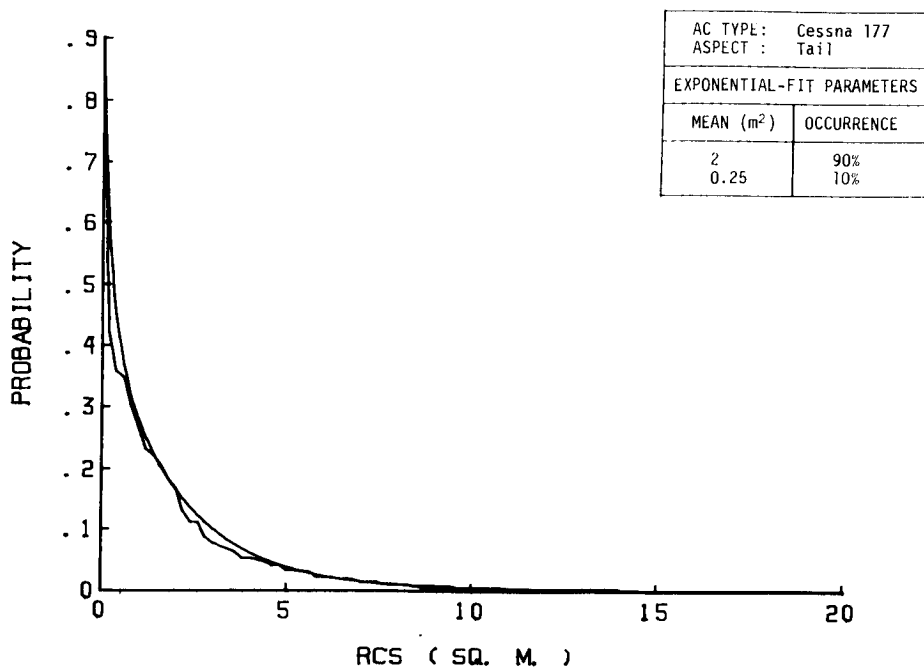


Figure B-9. RCS Probability Density Function.

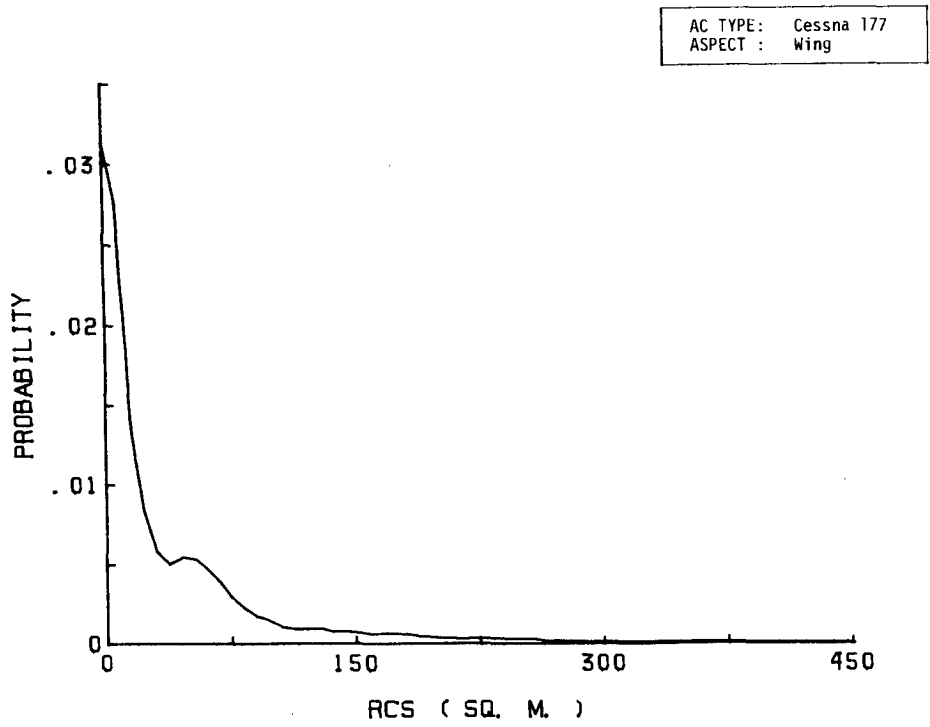


Figure B-10. RCS Probability Density Function.

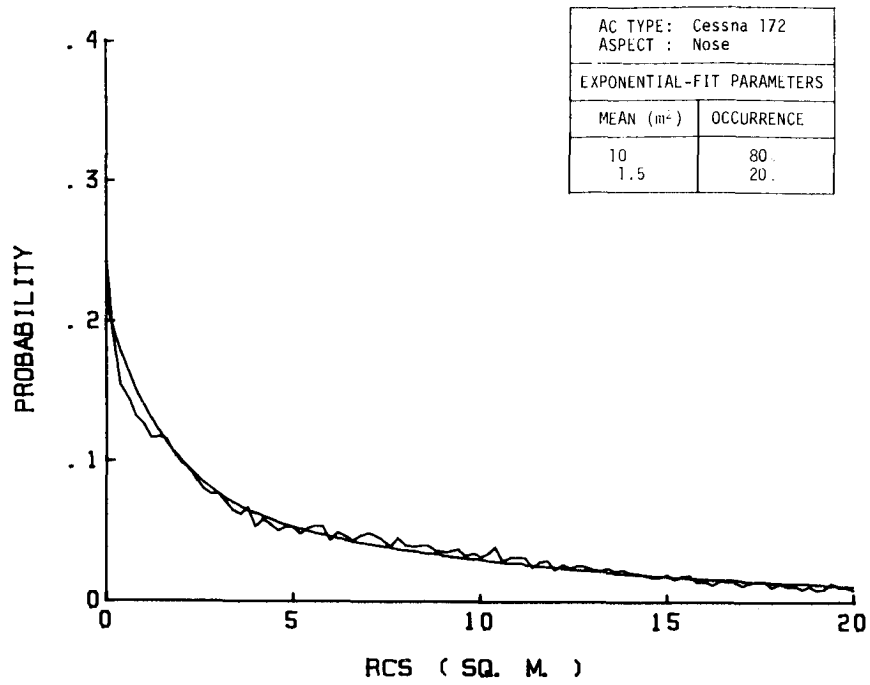


Figure B-11. RCS Probability Density Function.

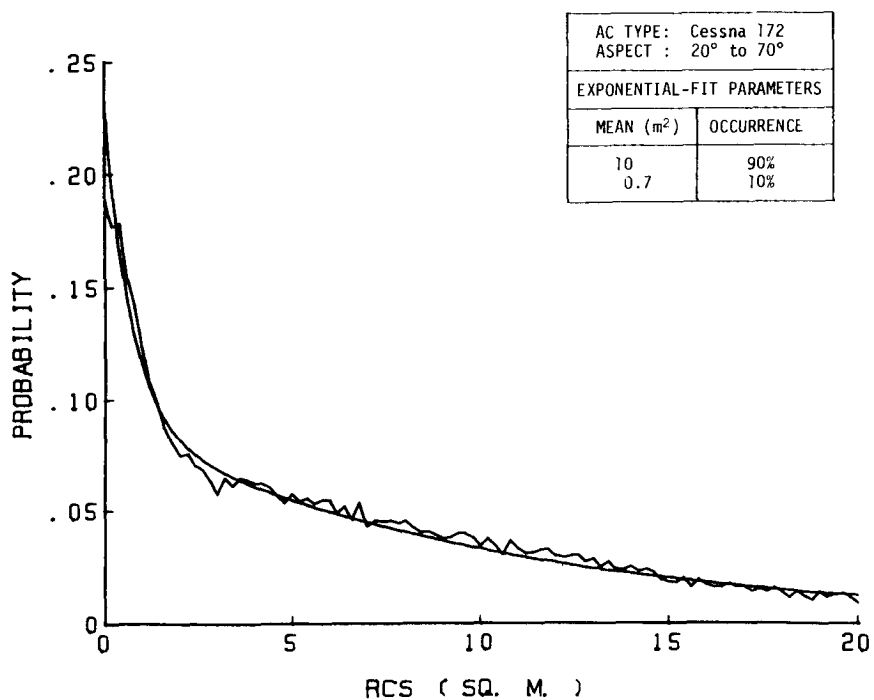


Figure B-12. RCS Probability Density Function.

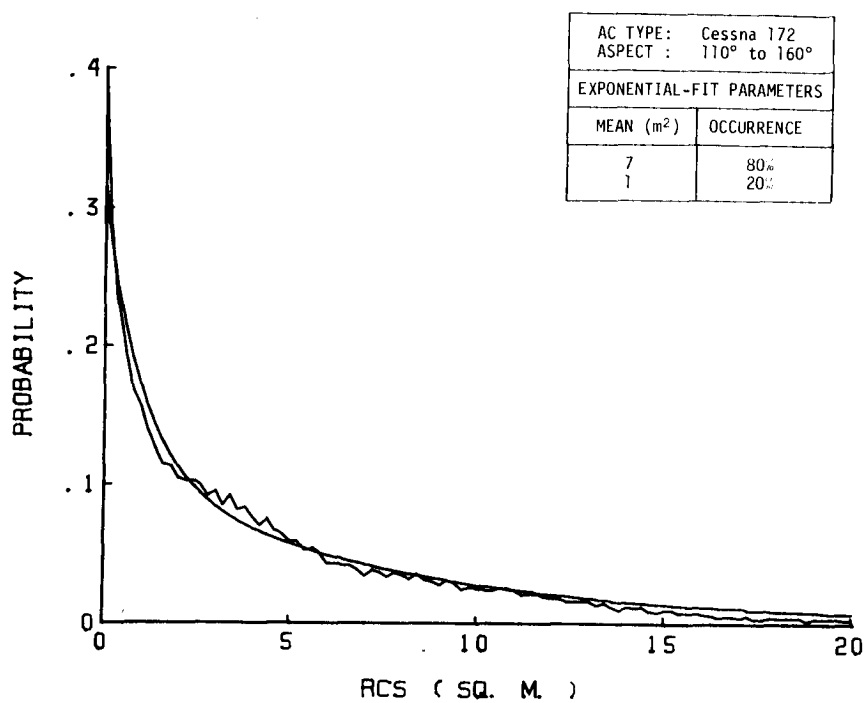


Figure B-13. RCS Probability Density Function.

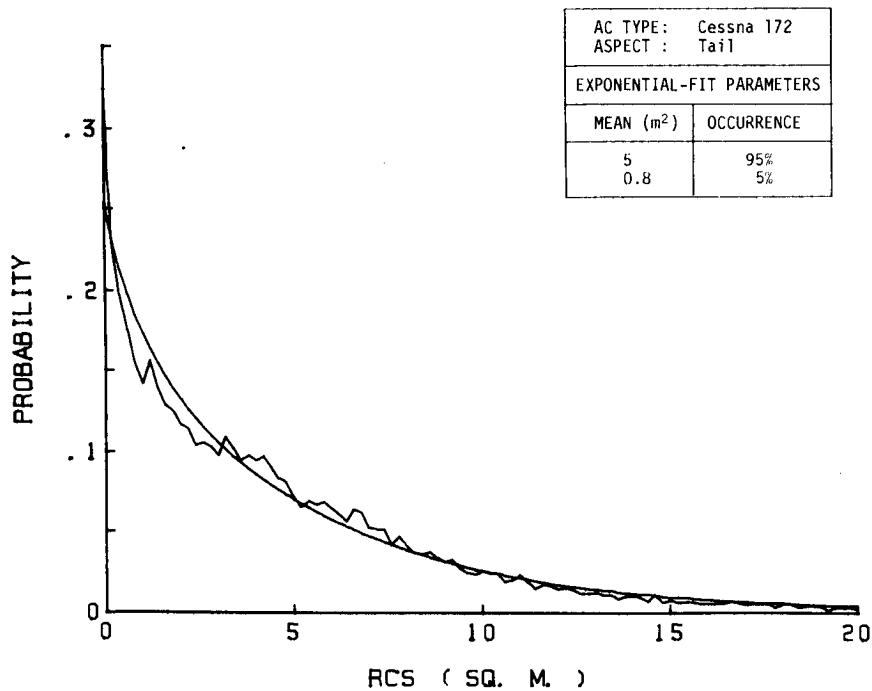


Figure B-14. RCS Probability Density Function.

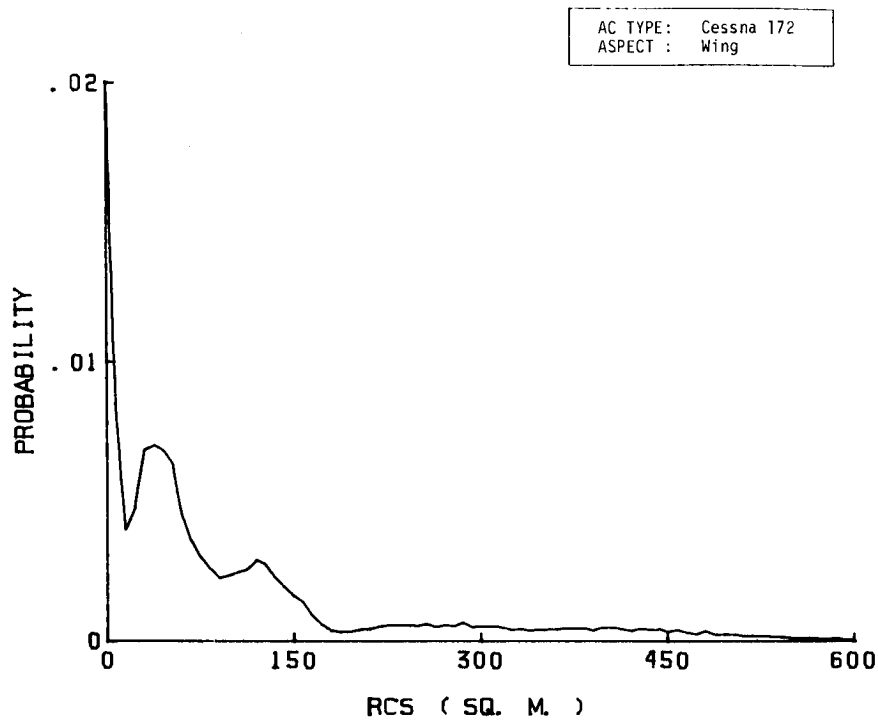


Figure B-15. RCS Probability Density Function.

## A P P E N D I X C

### Calculation of Signal Margin Above MDS

#### 1. ASR-5, WITH 7 m<sup>2</sup> TARGET AT 11 nmi

Equation (1) may be solved to get the mean received power:

$$P_r = \frac{P_t G^2 \lambda^2 \sigma}{(4\pi)^3 R^4} = \frac{4 \times 10^5 \times 10^{6.8} \times (0.107)^2 \times 7}{(4\pi)^3 \times (11 \times 1853)^4} = -62.3 \text{ dBm.} \quad (\text{A.1})$$

System noise power may be calculated from:

$$N = k B [T_o (\overline{NF} - 1) + T_a], \quad (\text{A.2})$$

where  $k$  is Boltzmann's Constant,  $B$  is the receiver bandwidth,  $T_o$  is 290°K,  $T_a$  is the effective antenna temperature, and  $\overline{NF}$  is the receiver noise factor. Solving eqn. (A.2) yields:

$$\begin{aligned} N &= 1.38 \times 10^{-23} \times 1.44 \times 10^6 [290(10^{0.4} - 1) + 120] \\ &= -109.6 \text{ dBm} \end{aligned} \quad (\text{A.3})$$

Hence, the basic signal-to-noise ratio is 47.3 dB.

The following losses must be added:

System loss	-21.1 dB
STC Loss (11 nmi, measured)	- 3.0 dB
Antenna Pattern Loss (2.2° elevation)	<u>- 3.6 dB</u>
TOTAL LOSS	-27.7 dB

Hence, the average net signal-to-noise ratio is 19.6 dB, on a single-pulse basis.

## CRC DOCUMENT CONTROL DATA

1. ORIGINATOR: Department of Communications/Communications Research Centre

2. DOCUMENT NO: CRC Report No. 1291

3. DOCUMENT DATE: March 1976

4. DOCUMENT TITLE: Radar Detectability of Light Aircraft

5. AUTHOR(s): M.V. Patriarche, G.O. Venier and J.R. Lewis

6. KEYWORDS: (1) Radar  
(2) Detection  
(3) Air-Traffic-Control

7. SUBJECT CATEGORY (FIELD & GROUP: COSATI)

17 Navigation, Communications, Detection, and Countermeasures

17 09 Radar detection

8. ABSTRACT:

On behalf of the Department of National Defence, a study has been made of the factors determining the ability of radar to detect light aircraft. Previously published work in this area was reviewed, and two series of experiments, in the time frame 1973 - 1975, were carried out to investigate the characteristics of the radar echo from light aircraft in flight. One series of experiments was carried out using the calibrated CRC coherent radar. The other series, conducted with the cooperation of the Ministry of Transport, made use of an operational Air Traffic Control radar.

The findings of the study are summarized, and recommendations are made concerning the design, siting, and operation of Air Traffic Control primary radars to improve their detection performance. It is pointed out, however, that these measures are unlikely to provide a complete solution to the problem of detecting light aircraft. A complementary approach is necessary: to require all light aircraft operating within airport control zones to be fitted with Secondary Surveillance Radar transponders. The simultaneous use of the two independent sensors (primary and secondary radar) should virtually eliminate the problem.

9. CITATION: \_\_\_\_\_  
\_\_\_\_\_

PATRIARCHE, M. V.

--Radar detectability of light aircraft.

, TK

∴ 5102.5

0673e

#1291

DATE DUE

DATE DE RETOUR \_\_\_\_\_

[illegible]

LOWE-MARTIN No. 1137

CRC LIBRARY/BIBLIOTHEQUE CRC  
TK5102.F5 C672 .A123

TK5102.5 C673e #1291 c. b

Patriarche, M. V.

INDUSTRY CANADA / INDUSTRIE CANADA



209149

